3-2010

A SOLUTION-BASED APPROACH TO THE FABRICATION OF NOVEL CHALCOGENIDE GLASS MATERIALS AND STRUCTURES

Nathan Carlie
Clemson University, ncarlie@clemson.edu

A SOLUTION-BASED APPROACH TO THE FABRICATION OF NOVEL CHALCOGENIDE GLASS MATERIALS AND STRUCTURES

A Dissertation
Presented to
the Graduate School of
Clemson University

In Partial Fulfillment
of the Requirements for the Degree
Doctor of Philosophy
Materials Science and Engineering

---

by
Nathan A. Carlie
March 29, 2010

Accepted by:
Dr. Kathleen Richardson, Committee Chair
Dr. Igor Luzinov
Dr. Jian Luo
Dr. Konstantin Kornev
Mr. Norm C. Anheier

ABSTRACT

Chalcogenide glasses (ChGs) are well known for their large optical nonlinearities and high infrared transparency, and are candidate materials for next-generation thin film-based planar infrared (IR) optical applications. They are also known, however, to possess low thermal and mechanical stability as compared to oxide glasses. Traditional physical vapor deposition (PVD) methods used for the deposition of these materials as thin films often suffer from low deposition rates, deviation from stoichiometry, and cannot coat over complex surfaces. In order to retain the attractive optical properties of ChGs while enabling new fabrication routes and hybrid and composite material systems, we have developed a novel technique for the deposition of ChG-based materials through dissolution of bulk glasses in organic solvents. Utilization of the solution phase allows for new deposition routes such and spin-coating and direct fabrication of ChG optical structures in a single step using micro-stamping techniques. Solution-derived thin films in the As-Ge-Sb-S system are shown to possess similar molecular structure to the parent bulk glass, and vacuum heat treatment allows the preservation of IR transparency through the removal of residual organics. Additionally it is shown that glass-polymer hybrid materials may be created through the incorporation of compatible polymers in the co-solution phase. It was shown that it is possible to tune the optical and mechanical properties of these coatings by tailoring the glass chemistry/polymer content over a broad range, important for applications in IR optical coatings and as interfacial materials where thermal and mechanical property matching is critical. This technique was shown to be a promising route towards the preparation of novel IR optical materials and structures.

DEDICATION

Above all, this work is dedicated to my forgiving wife *Alison* and my beautiful daughter *Charlotte*, who put up with all the late nights, busy weekends and general stress which result from trying to address all the myriad details that always seem to pop-up. Thank you so much for being such a great “single mom” while I’ve been lost in my work. To my parents, grandparents, and my family as whole - thank you for being by my side.

Naturally, none of this would have been possible without the guidance and support of my advisor Kathleen Richardson, who has given me the opportunity to see fascinating places around the world, work with some terrific collaborators, and to choose a research topic that has been both challenging and rewarding. *Dr. Laeticia Petit* has worked with me as a mentor for nearly 6 years now and who, more recently with *Dr. J. David Musgraves*, has kept keep me focused, organized, and motivated. Without you I would have been lost long ago. Thanks to you all for keeping me on the path.

Finally, I would like to thank all those who I’ve worked with over the years, at the University of Central Florida, the University of Bordeaux, the Massachusetts Institute of Technology, Pacific Northwest National Lab, my teammates and committee members and the faculty and staff of the School of Materials Science and Engineering at Clemson University. There is no such thing as a truly individual effort, and all of your contributions are appreciated. Thanks so much!

ACKNOWLEDGMENTS

I would like to acknowledge the United States Department of Energy (DoE) for partial funding of this research, which was conducted under project #DE-FG52-06NA27502 entitled “Novel Material and Manufacturing Technology Development for a High Sensitivity, Target-Specific Planar Optical-Microsensor-Array for Remote Sensing of Chemical Species”. This project was conducted as part of a multi-university effort between Clemson University, MIT, and the University of Central Florida, and much of the work on bulk glass characterization and solution-derived glass coating development was performed as part of this project.

I would also like to thank my collaborators on other aspects of this work, Dr. Georges Boudebs, at the University of Angers II in France, for performing the nonlinear optical property measurements and Norm Anheier at Pacific Northwest National Lab (PNNL) for providing the training and laboratory access to make the infrared prism coupling measurements. The novel instrument used to generate these data in this dissertation was developed during a three month internship at PNNL, and housing and laboratory space was provided during the duration. Prof. Lionel Kimerling at the MIT Microphotonics Laboratory and Dr. Michael Drews at the Clemson Conservation Center provided micro-Raman spectroscopy measurements. Finally, I would like to acknowledge the many contributions of Dr. Dave Musgraves, Dr. Bogdan Zdyrko, and especially Dr. Laeticia Petit who acted as my mentor throughout this research, and without whom it would not have been possible.

TABLE OF CONTENTS

Page

LIST OF TABLES

LIST OF FIGURES

List of Figures (Continued)

Figure Page

List of Figures (Continued)

List of Figures (Continued)

Figure Page

List of Figures (Continued)

Figure Page

List of Figures (Continued)

Figure Page

CHAPTER ONE

Introduction

1.1 Motivation

This work was realized as part of a multi-university effort developing integrated lab-on-chip optical sensor systems. The final goal of this work is the production of a prototype planar infrared (IR) sensor based on chalcogenide glasses (ChGs) which incorporates microfluidic channels for delivery of liquid or gaseous analytes, and leverages optical resonance to enhance effective interaction lengths and sensitivities. Specificity and further increases in sensitivity are provided by tailored polymer coatings which preferentially bind certain analytes to the polymer matrix, increasing analyte concentration near the sensor surface. Ultimately, this device is intended to be integrated with the requisite light sources, detectors, and electronic processing circuitry onto a single Si chip using CMOS-compatible fabrication techniques, which allows for large-scale production and reduced unit cost.

Within this framework, materials were chosen to meet certain criteria for the application. These include: infrared transparency (to allow for low optical loss at wavelengths corresponding to the characteristic optical absorption bands of organic molecules), high refractive index (for tight confinement of optical energy within the resonator structure), processibility into thin film form (for compatibility with CMOS-based lithographic fabrication techniques), chemical compatibility (for adhesion of polymer layers and resistance to the chemical environment to be sensed) and suitability for direct-laser writing of waveguide structures. Chalcogenide glasses (ChGs) meet all of

these criteria and are well suited to this type of application; however, in an effort to further enhance ultimate device performance, this thesis work aimed to evaluate alternative strategies for their merits to ascertain if it is possible to improve on traditional glass film synthesis and fabrication techniques.

As a route to the preparation of novel material systems such as hybrids and composites, and in order to simplify fabrication and open the door to new types of structures and optical components, this dissertation posed the question: *Can a solution-based approach to fabricating diverse ChG thin film structures be used to realize materials and devices which cannot be achieved by traditional means?*

1.2 Theoretical background

Glasses

The term chalcogenide glass generally denotes an amorphous material which is comprised primarily of the elements S, Se, or Te combined with a number of semi-metals (Ge, As, Ga, Sb, etc.). Chalcogenides make up a well known material system that has been studied for more than fifty years [1] and can exist in either a crystalline or amorphous state. Like all glasses, ChGs exhibit a glass transition, a fact which becomes very important for the processing of bulk glasses into thin film and fiber form as required for most applications. Figure 1.1 depicts the kinetics of a standard melt-quench glass formation process is shown below for clarity.

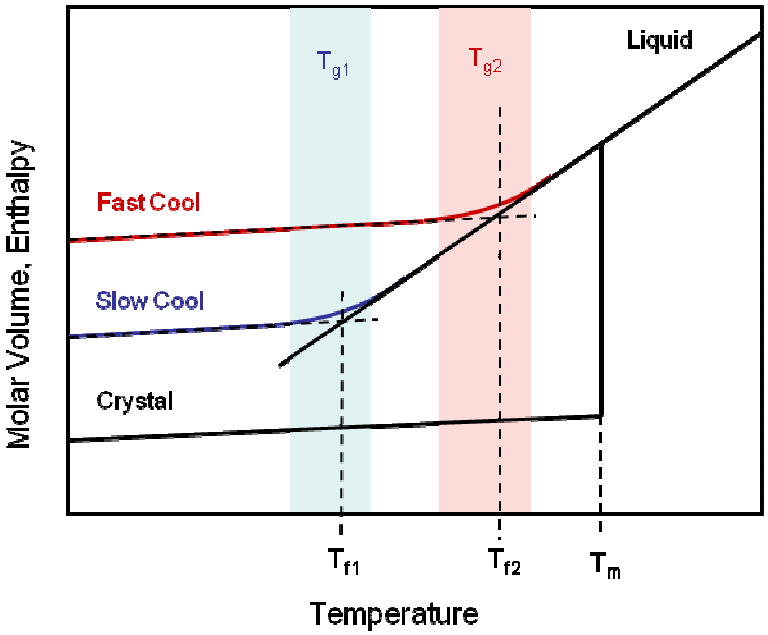

Figure 1.1: Plot of glass enthalpy on cooling from the melt for different heating rates

Generally, when a molten material is cooled through the melting point (T_m), a first order phase transformation occurs, the melt solidifies and a crystal is formed. Because the growth rate of the crystal is kinetically limited, the melt may be cooled quickly enough to delay this phase transformation. This kinetic barrier allows the liquid to be cooled below its melting point, forming what is known as a super-cooled liquid. The viscosity of this liquid is dependent on temperature, and for this reason if sufficient under-cooling is achieved, large-scale atomic motion will cease before significant crystallization can occur. This results in a solid material which still possesses the randomized structure of the liquid.

As shown in Figure 1.1, molecular motion will cease at an earlier time for rapidly cooled glass than a slow cooled glass. This causes the metastable structure of a more rapidly quenched glass to resemble that of the equilibrium liquid at a higher temperature. This variation in structure due to quench rate is often characterized by the fictive

temperature (T_f) of the glass, which may be defined as the temperature at which the particular glass would possess the same structure as the super-cooled liquid. While fictive temperature is a useful way of describing glass structure, it is difficult to directly measure as it requires comparison of the glass structure to that of the high temperature liquid. Moreover, because it is only kinetically frozen, the structure of a glass can relax over time. Physically, relaxation is the process of thermal bond breaking leading to rearrangement of the structural units of the glass which is driven by residual stresses and excess entropy left over from the quenching process. In the glassy state, at any stage of the relaxation process, a relaxation time (τ) is defined by the relaxation equation [2]:

$$\left(\frac{\partial H}{\partial t}\right)_T = \frac{-(H - H_c)}{\tau} \qquad (1.1)$$

where H is the enthalpy at a time t and H_c the equilibrium (crystalline) enthalpy, and thus H - H_c is the excess enthalpy retained by the glass. This relaxation time (τ) is controlled by the viscosity of the glass, as shown by Maxwell [3]:

$$\tau = \frac{\eta}{G} \qquad (1.2)$$

where η is the shear viscosity and G is the shear modulus. Because the relaxation process (viscosity) is thermally activated, it is expected to observe Arrhenius dependence:

$$\tau = \tau_0 \exp\frac{\Delta H^*}{RT} \qquad (1.3)$$

where τ_0 is a structurally dependent prefactor, R is the ideal gas constant and ΔH^* is the activation energy for structural relaxation [4], which is approximately equal to the activation energy of viscous flow [5]. Looking back at equation 1.1, however, we can see

that the driving force for relaxation, which controls viscosity, is itself influenced by relaxation. This makes the process nonlinear and time dependent. We can, therefore, only apply an Arrhenian approximation over short time scales and narrow temperature ranges. Generalized functions describing glass viscosity curves which take this effect into account have been developed, but are beyond the scope of this work. This information is included however, as ChG's posses low T_g's with measurable relaxation times at room temperature which can influence long term material (and hence device) stability. This stability is critical to long-term performance, especially in fiber materials [6] or thin films which are further from equilibrium (as compared to bulk glasses).

Because bonds are broken during heating, additional translational and configurational degrees of freedom become accessible to the molecular units forming the glass network. This can be detected by measuring the temperature dependence of entropy-related material properties, such as heat capacity using differential scanning calorimetry (DSC) or thermal expansion using dilatometry or thermo-mechanical analysis (TMA). To understand this process, we can approximate heating at a constant rate over a temperature range of interest (T_2 - T_1) by N isothermal events, each lasting a time Δt, giving:

$$\Delta t = \frac{(T_2 - T_1)}{qN} \qquad (1.4)$$

where q is the heating rate [4]. The glass transition temperature (T_g) is defined as the temperature below which the glass can be considered an elastic solid ($\tau < \Delta t$) and above which it can be considered a viscous liquid ($\tau > \Delta t$). Thus, we can see that T_g may be

defined as the temperature at which structural relaxation time (τ) is similar to that of the observation time (Δt) i.e.,

$$\tau(T_g) = K\Delta t \tag{1.5}$$

where K is a constant, which is defined by the instrument. Combining equations 1.3, 1.4 and 1.5, we can derive the following [4]:

$$\tau_0 \exp\left(\frac{\Delta H^*}{RT_g}\right) = \frac{K(T_2 - T_1)}{qN} \tag{1.6}$$

We can further derive a relation between the variation of the observed T_g as a function of the experimental heating rate, used for instance in DSC measurements, which was previously reported by Moynihan [7]:

$$\frac{d\ln|q|}{d(1/T_g)} = \frac{-\Delta H^*}{R} \tag{1.7}$$

Thus, we can see that T_g is logarithmically dependent on heating rate. In fact, this transition from solid to liquid is not abrupt but gradual, because viscosity varies continuously as a function of temperature, which implies that T_g is not a well defined temperature, but is a broad temperature range.

It is important to note several of the facts discussed here in order to understand some of the unique properties of glasses. Firstly, that T_g is not a thermodynamic transition, but is simply removal of the kinetic barrier to structural rearrangement. It does however have thermodynamic signatures, which is the reason that T_g is usually measured rather than T_f. Secondly, T_g is not an absolute value, but occurs over a range of temperatures where relaxation occurs over similar time scales to that of the observation,

which makes the value dependant on the measurement conditions. Finally, due to the relaxation process, the properties of the glass (density and refractive index most importantly), are determined in part by its thermal history. This has important implications for fields which employ fibers and especially thin films, because different cooling rates during formation and subsequent thermal processing steps induce variation in the physical and optical properties as compared to those of the parent bulk glass. Annealing, or heating of the glass to a temperature near T_g, is often employed both to remove excess stress and allows many film properties to approach bulk values through structural relaxation. For this reason, the properties of the thin films prepared during this study were extensively compared to those of the bulk glass, and the effects of post-deposition annealing were examined.

Chalcogenides

As compared to their oxide glass counterparts, chalcogenide glasses (ChGs) are comprised of larger, heavier atoms which have very similar electronegativities (1.8-2.5). These facts give ChGs some of their defining characteristics. High atomic mass and electronic polarizability lead to low phonon energies and high refractive indices, giving these glasses excellent transparency in the infrared, and interesting uses as hosts for rare-earth ions. Low strength and highly covalent bonding lead to comparatively low T_g and hardness values, allowing for easy polishing and processing into thin films or fiber form. This makes them attractive for infrared optical applications such as IR photonics [8-10], laser power delivery [11-13], Raman gain amplification [14], supercontinuum generation

[15, 16], and IR optical sensing [17-22]. Additionally they also tend to exhibit wide glass forming regions, even including non-stoichiometric chalcogen concentrations, which allows tailoring of glass chemistry and properties to meet device engineering constraints.

In order to form a glass, the liquid must be able to be cooled below its melting point and reach the glass transition, $\eta \approx 10^{12}$ Pa.s, before significant crystallization occurs. This generally requires low crystal growth rates and/or high melt viscosities. The most commonly used glass formers contained within the chalcogenide systems are $GeS_2/GeSe_2$ and As_2S_3/As_2Se_3 with other elements acting as intermediates (Ga, Sb, Te) or modifiers (S, Se, I). In this sense, we define an intermediate as a substance which will not form a glass on its own but will act as a glass former when combined with other materials, while a modifier is used to alter the network structure and/or to help prevent devitrification. It should be noted that, the structural role of the various elements in ChGs is more flexible than in oxides, and these characterizations should only be applied on a case-by-case basis. For example, Te may act as a three-fold or four-fold coordinated cation in the Te-I and TeO_2 glasses [23] or twofold coordinated anion in the As-Te system [24]. Its structural role in As-Te-Se [25] and Ge-Sb-S-Te [26] glasses is still unclear, but is expected to be in one of these multi-valent configurations.

Covalently bonded oxide glasses tend to from heteropolar charged dangling bonds or non-bridging oxygen ions (NBOs) rather than O-O homopolar (peroxide) bonds, for instance when alkaline elements are added or as defects. However, homopolar bonds such as S-S are far more common in ChGs than charged species such as the equivalent non-bridging sulfur ion (NBS). In fact, the only commonly used compound which forms

charged species in these glasses is Ga_2S_3, which is known to form GaS_4^- tetrathedra within the glass network, and is commonly used to increase the solubility of rare earth cations through charge balancing. As a general structural model, we therefore consider the coordination spheres of both the metals and chalcogens to be always complete (2 bonds for S/Se, 3 bonds for As/Sb and 4 bonds for Ge) and any excess or deficiency of the chalcogen is accounted for by chalcogen-chalcogen or metal-metal homopolar bonds respectively. In the case of As-based glasses, this leads to a predominantly two-dimensional (2D) layer-like network while in Ge-based glasses the network is predominantly three-dimensional (3D) [27]. This has important consequences for the thermal and physical properties of the glass i.e., hardness and T_g, which are generally higher for Ge-based compositions.

Another important attribute of these glasses which is caused by the structural versatility of their elemental constituents, is the sensitivity of these glasses to high intensity or short wavelength (above the absorption band gap) irradiation. Here, such irradiation can lead to bond rearrangement and changes in the physical and optical properties of the glass. These changes can be either permanent, metastable (reversed by annealing), or reversible (relaxing to their original state over time) [28], and can proceed via multiple mechanisms over various timescales [29, 30]. This leads to additional applications as optical (ovonic) memory [31, 32], inorganic photoresists [33, 34] and direct-written optical structures (waveguides), gratings or microlenses [15, 19, 21, 35-39].

Most of these device applications require the glass to be processed into either fiber or thin film form. Traditionally, chalcogenide films are deposited using physical vapor deposition (PVD) techniques such as thermal evaporation, pulsed laser deposition or sputtering. While these methods are generally simple, they suffer from several shortcomings which occasionally restrict their use. They are generally limited to largely two-dimensional surfaces, and require high-vacuum processing and sometimes difficult target preparation in the case of laser deposition and sputtering. Another complication, particularly for thermal evaporation, is the observation that the resulting film often has a different composition (stoichiometry) from that of the parent glass target, or is inhomogeneous across its thickness, due to differential volatility in multi-component materials. A common solution to this problem is multi-source depositions where as many as four materials may be simultaneously evaporated at different temperatures in order to reach a desired film composition [6]. This solution to the problem of inhomogeneity turns what was a straightforward deposition method into one which is complex and generally imprecise to control or tailor.

Solution-based coating methods offer a potential pathway to overcoming these limitations. By controlling the chemical composition of the solution phase, the chemistry of the film may be controlled with high precision. Techniques such and spray-coating, spin-coating or dip-coating may be used over highly varied (shaped) surfaces by taking advantage of the surface tension of the solution, and are suitable for large surface areas/high production volumes. The elimination of high vacuum during the deposition also allows for higher production rates and simpler processing. An added advantage of

the solution phase is the opportunity to incorporate other materials into the film, as long at this material may be dissolved or dispersed into the same solution. Examples of these materials might be carbon, noble metal or semiconductor nanoparticles, or polymers, allowing for the creation of hybrid or composite coatings with novel functionalities or enhanced properties. Such solution-based processes are fertile ground for research, and to date, composite and hybrid chalcogenide materials are largely unstudied. Thus, this thesis examines key material and process variables associated with fabricating ChG thin films and structures using a novel solution-based approach.

1.3 Applications of chalcogenide thin films and glasses

The IR transparency of chalcogenide glasses (ChGs) leads to a wide variety of optical applications; however, the band gap and conductivities of these materials can be varied over a wide range, which can lead to electronic applications as well. Among these, the most prominent is as Li^+ ion conducting electrolytes for secondary (rechargeable) battery applications [40]. Oxysulfide glasses based on P_2S_5 [41, 42], B_2S_3 [43], GeS_2 and SiS_2 [44, 45] have been shown to have relatively open structures compared to the small Li^+ ion leading to high ionic conductivities combined with good mechanical durability compared to liquid and polymer electrolytes which can prevent dendrite formation and improve operating temperature ranges [46].

Most sulfide and selenide glass are considered to be amorphous semiconductors, and crystalline As_2S_3 is an inherent p-type semiconductor. The addition of Tl has been shown to increase the hole mobility in As_2S_3 glasses [47], providing a p-type

semiconductor, while the addition of Bi to GeS_2-based glasses can be used to create n-type semiconducting glasses [48], making these materials also attractive for electronics applications. However, a better understanding of the nature and influence of inherent defects in these materials is still needed [49]. Another electronic application of doped ChGs is in ion-selective electrodes [50-52] and electronic tongues [53]. The high solubility of the glasses for "soft" ions (Cu^{2+}, Pb^{2+}, Cd^{2+}, Hg^{2+}, Ag^{+}, etc.) allows doped films with high ionic conductivities for these species. Similar doping of noble metal elements also allows the tailoring of the electric conductivity and band gap for application as photoconductive sensors [54] and thermoelectrics [55]. Recently, there have also been increasing interests in applications of transition metal (e.g. Cu, Ag, Sn, Cr) doped chalcogenide glasses as optical memory and laser materials [56]. Previous investigations [57] have shown that the introduction of Cu into the As_2Se_3 glass causes a substantial increase in the efficiency (contrast, photosensivity, reversibility and diffractive efficiency) of optical recording on thin films of $Cu_x(As_2Se_3)_{100-x}$ with $x < 20$ at.%.

Optical recording in ChGs is well known and forms the basis of current rewritable optical disk technologies like CDs and DVDs [32]. The most commonly used alloys are Ge-Sb-Se-Te and Ag-In-Sb-Te systems, that operate through laser heating and thermally-induced phase changes. Lower pulse energies are capable of heating the glass above its glass transition temperature inducing rapid crystallization, while high pulse energies heat the film above its melting point and lead to revitrification [31]. The different reflectivity of the crystalline and amorphous phases is used to differentiate between the "1" and "0"

values needed for memory. Non-volatile memory systems which can be both read and written electronically though changes in resistivity induced by crystallization are also under development [58], and Intel has reported that their next-generation memory will be based on this technology.

The primary optical applications of these materials are concerned with their high optical nonlinearity and infrared transparency. Initial development of these materials centered around optical fiber-based devices [6, 11, 59] have found applications in optical switching [60-62], telecommunications [63] infrared laser power delivery and supercontinuum generation [11, 64, 65], and remote IR chemical sensing [66, 67]. In more recent years, thin film versions of these devices based on waveguides, have been the focus of much research [15, 19, 61, 68-71]. Fabrication of waveguide structures in thin films have been manufactured using lift-off lithography [33, 70], reactive ion etching [39, 72, 73], ion implantation [39, 74], and photo-diffusion of silver into in the glass [75, 76]. All of these fabrication techniques have been shown to further alter the chemical stability of the glasses, which dissolve in standard alkali developer solutions used in photolithography. This property makes ChGs attractive as inorganic photoresists [34, 75, 77-80] using wet etching. Glass dissolution has become a focus of some interest recently as a method for fabrication of thin films [35, 79-82], and has seen more success than the adaption of traditional sol-gel techniques used for oxides to this system [81-83]. This technique holds promise for the development of new deposition routes for complex structures in these materials, and the development of novel hybrid and composite

materials, which have drawn considerable attention in recent years [84-97] due to the promise of optical functionality with greatly improved mechanical durability.

Expanding further to these preliminary findings, the focus of this work is the development of solution-based fabrication techniques for ChG-based materials which maintain high IR transparency and homogeneity.

CHAPTER TWO

Research Design and Methods

2.1 Sample Preparation

All of the materials examined in this work were prepared through the melting of elemental starting materials to form a bulk glass. In order to achieve high transparency at infrared wavelengths, chalcogenide glasses should ideally be free of lighter elements, including oxygen and hydrogen, which lead to absorption bands in the mid-IR region. It is therefore necessary to prepare all materials in a low humidity anaerobic environment. It should also be noted that unless otherwise stated, no special purification methods were employed to reduce the extrinsic impurities.

Bulk Glass Melting

High-purity elemental starting materials (As: Alfa-Aesar 99.999% Ge: Sigma-Aldrich 99.999%, Sb: Alfa-Aesar 99.999%, S: Sigma 99.999%,). were weighed inside a glove box under a nitrogen atmosphere containing less than 10 parts per million (ppm) of both oxygen and water. The appropriate weight of each element was then added to a cylindrical fused quartz ampoule, with a length of approximately 20 cm and a diameter between 1 and 2.5 cm, depending on the total mass of the batch to be melted. The ampoule was then placed under vacuum using a turbo-molecular pump, without exposure of the batch to room air, and maintained at 90 °C for at least 4 hours. This temperature was chosen in order to drive off any residual water on the surface of the starting materials and ampoule, without melting the sulfur contained in the batch. After 4-8 hours under

these conditions (depending on the total mass of the batch), the ampoule was then sealed with a gas-oxygen torch. The batch within the sealed ampoule was then melted by heating to between 700 and 925 °C, depending on the composition of the glass, using a heating rate of 2.5 °C/min and holding at the melt temperature, for 12-24 hours, depending on the mass of the batch to melt. The glass melt was homogenized through the use of a specially designed rocking furnace which rotates the ampoule and batch through 90°, perpendicular to the long axis, at a rate of 5 cycles/minute. Lastly, the rocking was stopped while the temperature of the furnace was decreased by 25 to 50 °C in order to prevent entrainment of bubbles within the melt, and the ampoule and batch were quenched to room temperature by removal from the furnace and cooling in room air. Samples were annealed at 40 °C below T_g over night in order to remove the thermal stress from the quench and to increase the glass mechanical stability.

Film deposition by spin-coating

Solution-derived films were deposited onto 3" silicon wafer substrates and 3" BK7 glass (Schott Glass) substrates using a three step process which consists of i) solution preparation by dissolution of bulk glass powder, ii) spin-coating, and iii) heat treatment. In order to prevent the incorporation of atmospheric water into the hygroscopic solvents used, as well as to prevent oxidation of the solutions, all steps were performed inside a glove box and/or under nitrogen atmosphere.

The first step of this process was dissolution of the glass to form the solution. Finely ground glass was dissolved in a solvent by stirring at room temperature until

complete dissolution was achieved. As discussed in detail in Chapter 4, the duration of this step varied as a function of both the solvent and glass composition. Because precipitation of some of the glass constituents can occur at high loadings, the glass solubility limits were defined for each solvent/glass pair.

For the second step, the spin-coated films were prepared using a programmable computer-controlled spin-coater (Model G3 from Specialty Coating Systems). This spin coating system allows the tailoring of four main variables, including spin-up time (acceleration), spin speed, dwell time, and spin-down time (deceleration). In addition, it is also possible to add hold times between the application of the solution to the substrate (initial hold), and between the end of spinning, and annealing of the film (final hold). In each case, the key metrics for optimization of the spin-coating procedure were the surface roughness, thickness, and thickness uniformity for the final film.

The last step for the processing of solution-derived films was heat treatment to remove any residual solvent from the film, stabilizing the final physical structure of the film and allowing the separate dissolved glass components to densify into a continuous network. After completion of the hold time following coating, the coated substrate was "soft-baked" by placing it into an oven or onto a hotplate, which was pre-heated to appropriate temperature for a period of several minutes in order to solidify the film and reduce moisture sensitivity so that it could be removed from inert atmosphere. After cooling from this "soft-bake", the film was then transferred into a vacuum furnace, which was purged with nitrogen and evacuated to ~1 Torr before heating to a higher temperature. This second annealing stage is intended to remove the residual solvent

which may be present interstially or may be chemically bonded to the dissolved glass components, and also to allow reaction between these components in order to fully densify the film and restore the glassy network.

2.2 Characterization of materials

The physical, thermal, optical, and structural properties of the fabricated bulk glass, and thin films were characterized using a series of techniques including Archimedes' density measurements, thermo mechanical analysis (TMA), differential scanning calorimetry (DSC), prism coupling, UV-Visible, Fourier-transform infrared (FTIR), and Raman spectroscopy.

2.2.1 Physical properties

For large-scale roughness measurement and estimation of film thickness uniformity, white light interferometric microscopy was employed (Zygo Corp. model NewView 6300). This technique utilizes and interferometric response to image a surface: a beam splitter is inserted into the beam path of a microscope, half of the light is focused by a microscope objective and is reflected from the sample surface, and the other half is reflected from a reference mirror inside the instrument. The two optical paths are combined by the beam splitter and imaged by a camera. Finally, the focal point of the

system is then raised and lowered by a piezo actuator system, and the computer records the image intensity for each pixel as a function of the distance to the sample. Because the image recorded by the camera contains an interferogram of the light reflected from the reference and sample surfaces, differences in the sample height from one pixel to the next can be seen as differences in the interference fringe pattern. The computer then mathematically transforms this data into sample height for each pixel, creating a three-dimension map of the sample surface. The primary limitation of this technique is the lateral resolution, which cannot exceed the diffraction limit. This translates to approximately 0.61 times the center wavelength of the light source (~530 nm) or approximately 320 nm, but is typically much larger as determined by the total magnification of the system and the pixel size of the camera. For instance, using a typical magnification (5x) and a 640x480 pixel camera provides a lateral resolution of ~2 μm.

For high resolution mapping of surface features, atomic force microscopy was employed using a Dimension 3100 (Digital Instruments, Inc.) microscope. This technique measures surface relief by scanning a silicon cantilever probe with a sharpened tip across the surface of the sample. A laser is reflected from the back surface of this probe and the angle of reflection is measured using a quadrant photodetector. As the height of the sample surface under the probe changes during the scan, the probe bends

and the reflection angle changes, leading to a change in the signal from the photodetector. A piezo actuator then moves the support of the probe vertically in order to restore the bending angle, and thereby the photodetector signal, to its normal value. The vertical position of the probe support is then related to the vertical position of the point of the sample surface under the probe.

In addition to the surface height, this instrument also allows the examination of the attractive forces between the probe and sample which lead to sticking though the use of “tapping mode” imaging, appearing as a phase-lag between the oscillating driving force provided by the actuator and the movement of the probe away from the sample surface. This tapping force mode allows improved resolution, and the possibility of discerning regions of the sample with different elastic properties, which may be caused, for example, by phase separation. Generally the resolution of this technique is limited only by the size of the probe tip which may be less than 1 nm. Silicon tips with spring constants of 50 N/m were used, and imaging was done at scan rates in the range 1 - 2 Hz.

Morphology

The micro-scale structure of bulk and thin films samples was examined using both optical microscopy and a scanning electron microscope (SEM). *Optical microscopic*

images of polished bulk glass sections and thin films were acquired using a Nikon model 115 microscope at up to 500x total magnification, and were examined for the presence of any bubbles, cracks, or suspended particulates within the glass as well as for any signs of crystallization or phase separation.

Electron microscopy was performed using a Hitachi model S3400 SEM, under variable pressure mode, which allowed the imaging of non-conductive samples without the application of carbon or platinum coatings. This instrument was equipped with an electron backscatter detector, which allowed the observation of chemical differences at the sample surface through contrast differences. Film samples were cleaved and examined on-edge in order to examine any possible laminar or columnar structures. SEM observations also allowed the determination of the chemical composition of the bulk and thin film samples, through the use of an attached Oxford model Energy-dispersive X-Ray (EDX) spectrometer. During electron microscopy, the high energies of electron beam, generally used at 20 kV in this case, causes ejection of secondary electrons from the sample surface, as shown in Figure 2.1 below.

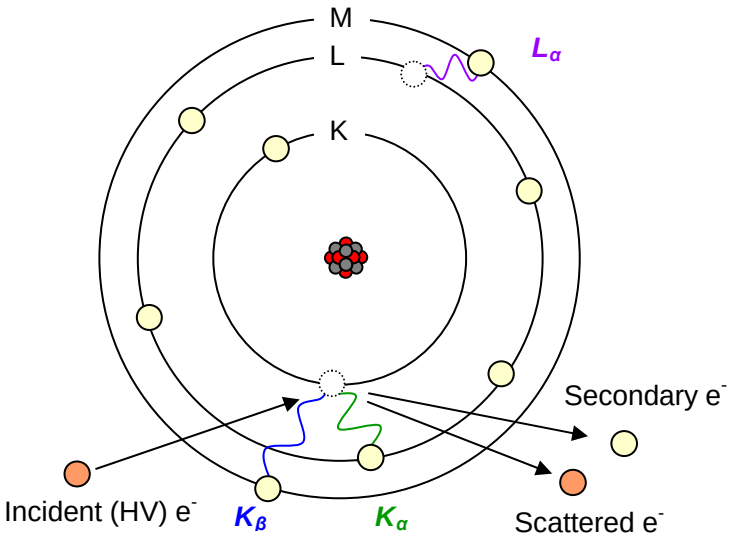

Figure 2.1: Schematic depicting secondary electron scattering and subsequent X-Ray emission under high-voltage (HV) electron beam bombardment.

As vacancies in core levels are filled by electrons from higher energy outer levels, X-Rays are emitted which have energy equal to the difference in energy between the levels and are characteristic of the element from which they originate. When one of these X-Ray photons is incident at the detector of the spectrometer, a charge pulse is created which is proportional to the energy of the incident photon. Each charge pulse is finally converted to a voltage pulse, and the spectrometer counts and sorts these pulses. The counts versus photon energy is displayed. Corrections for the X-Ray emission cross-sections of the different elements was applied in order to allow semi-quantitative compositional analysis (±1 at. %).

`

Density

In the case of bulk glasses, density was directly measured using Archimedes' principle. The sample was first weighed in air and then suspended in a liquid of known density (diethyl phthalate in this case). The weight of the sample when suspended may be expected to be reduced by the mass of the volume of liquid which was displaced, which was equal to sample volume multiplied by the density of the liquid. The sample density may then be calculated to within ±0.02 g/cm^3 as follows [98]:

$$\rho_s = \frac{m\rho_l}{\Delta w} \qquad (2.1)$$

Where ρ_s is the density of the sample, ρ_l is density of the liquid, m is the mass of the sample in air, and Δw is the change in weight of the sample upon submersion. The density of film samples was estimated from the refractive index using the Lorentz-Lorenz (Clausius-Mossotti) relation. Assuming that the average molar polarizability (α) of the species comprising a substance is constant, the refractive index (n) is dependent on the number density per unit volume (N) of those species as follows [99]:

$$\frac{n^2 - 1}{n^2 + 2} = \frac{4\pi}{3} N\alpha \qquad (2.2)$$

`

In the case of anisotropic crystals and polar liquids, where permanent polarization and two and three-body interactions contribute to the total polarization, the more complex Onsager model must be used [100]. However, glasses are expected to be isotropic due to their amorphous structures, the Lorentz-Lorenz is expected to be sufficient. Since the number density of polarizable species is proportional to the mass density, the density of the film can be expressed as a fraction of the bulk glass density:

$$\rho_f = \rho_g \cdot \frac{\left(n_f{}^2 - 1\right)\cdot\left(n_g{}^2 + 2\right)}{\left(n_f{}^2 + 2\right)\cdot\left(n_g{}^2 - 1\right)} \qquad (2.3)$$

where ρ_f and n_f are the film density and refractive index, and ρ_g and n_g are bulk glass index and density respectively.

Micro-hardness

The micro-hardness of the bulk glasses was determined using a Shimadzu model DUH-210 dynamic ultra-micro hardness tester from Shimadzu. The instrument was equipped with a Vicker's microindenter, which consists of a diamond point having a square profile, and cut at a 136° angle. The probe was pressed into the sample surface using a constant load which was held until a constant penetration depth into the sample surface was reached, and then held for an additional 2 seconds. After this time, the load was released, the indenter was withdrawn from the surface, and resulting indentation was

`

examined microscopically. The Vicker's hardness (H_V) of the sample was calculated from the average length of the diagonals (d) of the indentation (measured using an optical microscope) and the applied load (L) using the following relation [101]:

$$H_V = 2\sin\left(\frac{136^0}{2}\right)\frac{L}{d^2} = \frac{1.8544L}{d^2} \quad (\text{in kg/mm}^2) \qquad (2.4)$$

Commercial polycrystalline zinc selenide and fused silica samples were used for calibration, and the hardness was taken as the average of ten measurements.

2.2.2 Thermal properties

In this study, the glass transition temperature (T_g) of bulk glasses was determined using a (TA Instruments model 2920) differential scanning calorimeter (DSC). The instrument is designed to measure the amount of heat needed to raise the temperature of a sample by a set amount, as compared to a reference. The sample was contained in a hermetically sealed aluminum pan, with a second (empty) pan used as a reference, and the temperature of both pans are maintained at nearly the same temperature which was increased at constant rate. The heat flow was then recorded as a function of temperature, allowing changes in heat capacity or thermodynamic transitions, such as melting, to be observed. The DSC thermogram of the bulk glass with the composition $As_{42}S_{58}$, taken as an example, is shown in Figure 2.2.

`

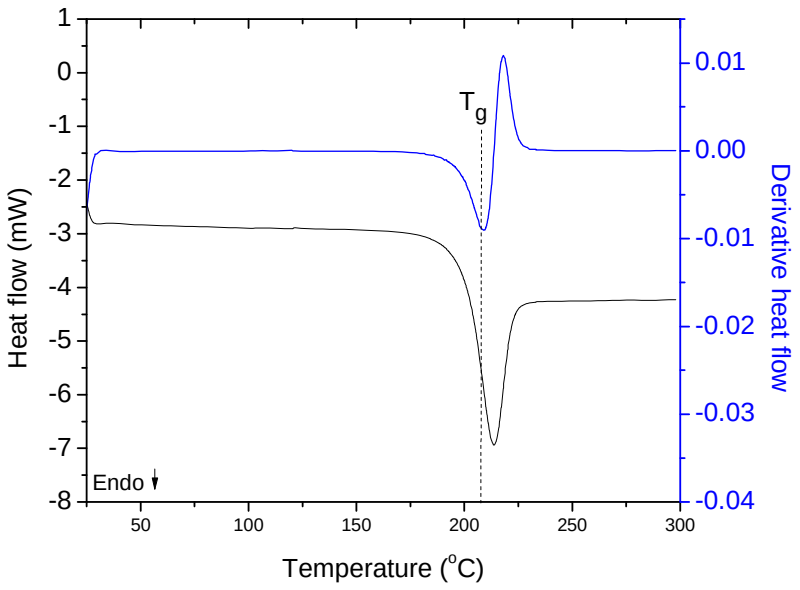

Figure 2.2: DSC thermogram of $As_{42}S_{58}$ acquired at 10 °C/min

As the temperature increases, an endothermic signal is seen which is associated with the glass transition. T_g was assigned as the inflection point of this first endotherm, taken as the minimum of the first derivative curve of heat flow versus temperature.

Due to the small mass provided by thin film samples, it is difficult to obtain a sufficient signal to noise ratio for T_g measurements using DSC. For this reason, a relatively new technique, micro-thermal analysis (model 2990 from TA Instruments) was employed. Depicted in the figure below, the instrument uses a platinum wire probe attached to a standard AFM head which is placed in contact with the film surface and heated at a constant rate. The vertical defection of the probe is observed during heating, similar to the operation of a thermal mechanical analyzer.

`

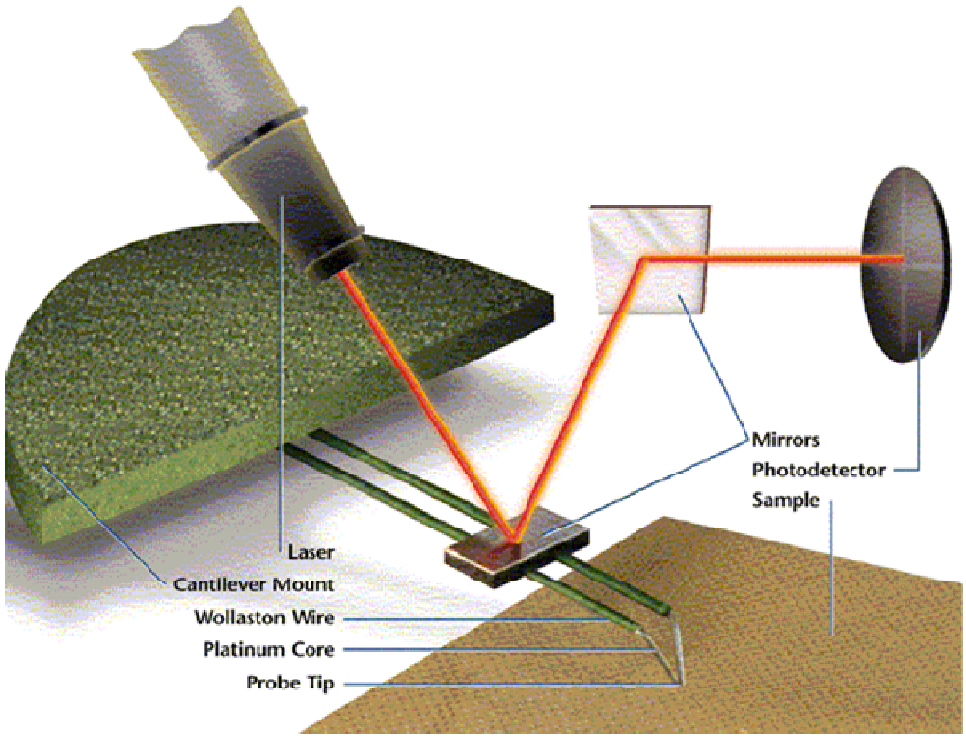

Figure 2.3 Schematic of probe heated-wire arrangement used in micro-thermal analysis

As the sample is initially heated by the probe, an upward movement of the probe is observed which is caused by thermal expansion of the local area of the sample and by the probe itself. This latter contribution is constant for all measurements, but would need to be considered as part of the total signal. At higher temperatures, where the glassy film begins to soften, the probe begins to move downward, indicating that the probe starts to penetrate into the sample surface. A sample thermogram for $As_{42}S_{58}$ bulk glass is shown in Figure 2.4 below.

`

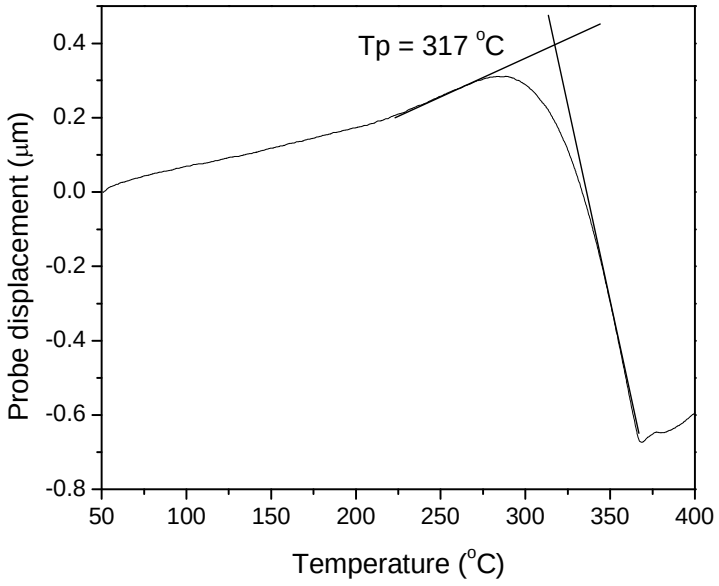

Figure 2.4: Micro-thermal analysis thermogram showing vertical probe deflection versus temperature for an 800 nm thick $As_{42}S_{58}$ film, with a heating rate of 10 °C/s.

This movement of the probe leads to a transition through a point of maximum deflection in the sensor signal, and an indentation at the surface of the film where the probe was in contact with the sample can be observed with an optical microscope after the measurement. The temperature at the onset of the probe's downward motion, as determined by the intercept of the two tangents shown in Figure 2.5 is labeled as the "probe-penetration temperature" (T_p). In order to estimate the experimental error of the T_p value in our measurements, each measurement was repeated at least four times, and the error bars (±10 °C) were derived from the variability of this data for a heating rate of 600 °C/min. A thorough description of the technique as applied to bulk and thin film chalcogenide glasses is presented in [102].

`

2.2.3 Optical properties

UV-Vis-NIR spectroscopy

A Perkin-Elmer model Lambda 900 UV-Vis-NIR spectrophotometer was used to examine the optical transparency of bulk glasses and thin films over the wavelength range of 200 to 2500 nm. This instrument measures the ratio of optical intensity transmitted over a reference path and through the sample to give the transmittance of the sample. In general, three primary sources exist for the loss of optical power transmitted through the sample: reflection, scattering, and absorption.

The first source of optical loss is reflection, which is caused by a difference of refractive index (n) as the light passes from one medium (air) into a second (glass), and is typically characterized by the Fresnel equation [99]

$$r = \frac{(n_1 - n_2)^2}{(n_1 + n_2)^2} \qquad (2.5)$$

where r is the reflection coefficient at normal incidence for the interface between two media with refractive indices n_1 and n_2. Since there are reflections at both glass surfaces (commonly referred to as the material's Fresnel reflections) and multiple reflections between them, the combined reflection coefficient (R) may be expressed by [99]:

$$R = \frac{2r}{(1 + r)} \qquad (2.6)$$

The second source of optical loss due to Rayleigh scattering, primarily caused by surface roughness or inhomogeneities within the sample which possesses a refractive index differing from that of the surrounding medium, such as bubbles or striae, and is

dependant both on the refractive index difference and on the size of the scattering center. For a well polished glass sample with good homogeneity and over short path lengths, this effect is often considered negligible.

The third source of optical loss is absorption which may be either intrinsic or extrinsic, depending on whether the electronic transitions are due to the material itself, such as valence band to conduction band transition, or due to impurities or dopants within the sample, respectively. After correcting for the Fresnel reflective losses and neglects scattering loss, the absorbance (A) of the sample may then be calculated from Beers's law where: [99]

$$A = -\log\left(\frac{1}{T}\right) \tag{2.7}$$

Finally the absorption coefficient (α), or equivalently the absorptivity, is calculated from the absorbance of the sample (A) and the path length of the light, or sample thickness (d) by:

$$\alpha = \frac{A\ln(10)}{d} \tag{2.8}$$

From the absorption spectrum it is possible to determine the optical band gap. In glasses, the primary source of absorption in the UV or visible spectrum is the excitation of electrons in the valence band of the glass into unoccupied states in the conduction band. Chalcogenide glass are known to display an indirect-type band gap transition, indicative of a change of momentum of the electron as it is promoted from the valence to the conduction band [103]. As a result, the region of high absorptivity($\alpha \geq 10^4$ cm^{-1}) may be described by the Tauc power law [104]:

`

$$\alpha h\nu = B\left(h\nu - E_g\right)^2 \qquad (2.9)$$

where B is the slope of the Tauc edge, which depends on the density of states (DOS), and E_g is the optical band gap energy. Because of the amorphous nature of glass, some localized states exist with higher energies than that of the equivalent crystalline structure. As a result, there exists an absorption "tail" which extends to longer wavelengths. The absorption coefficient in this weakly absorbing ($10\ cm^{-1} \leq \alpha \leq 10^4\ cm^{-1}$) portion of the spectrum may be described by the Urbach Exponential relation [105],

$$\alpha = \alpha_0 \exp\left(h\nu\right)/E_u \qquad (2.10)$$

where E_u is the Urbach energy. The relative value of E_u is often used as a tool for estimating the amount of disorder present within the glass network.

Fourier-transform infrared spectroscopy (FTIR)

FTIR spectra were used in this study for identification of various IR absorbing species such as impurities within the glass, or the presence of organic molecules, and the semi-quantitative comparison of their relative concentrations. This spectroscopic technique utilizes an interferometer to obtain the transmittance of a sample over wavelengths in the mid-IR from 2.5 to 20 μm, using a Nicolet model 530 FITR spectrometer. This instrument is comprised of a broad band infrared source and a Michelson interferometer with a movable mirror in one arm. The mirror is moved at a constant rate while in intensity of the light passing through the interferometer is recorded. The data generated by this process contains information on the temporal coherence of the light. By placing the sample in the beam path, this pattern is modulated, and the

transmittance of the sample may be extracted by applying the well-known Fourier transform.

Refractive index

The refractive index of a material is the ratio of the speed of light (c) in vacuum to the phase velocity (v_p) of light within the material. This is caused by differences between the magnetic permeability (μ) and dielectric permittivity (ε) of the material and those of free space (μ_0 and ε_0), resulting in a retardation of the propagating wave [106] where:

$$n = \frac{c}{v_p} = \sqrt{\frac{\varepsilon\mu}{\varepsilon_0\mu_0}} \qquad (2.11)$$

This property is one of the most important variables in the design of optical devices, and was examined in this study using a variety of techniques, for both bulk and thin film materials.

The refractive index of the investigated bulk and thin films was directly measured using the prism coupling technique in collaboration with Mr. Norm Anheier at Pacific Northwest National Lab. The normal configuration of the instrument is built around a fused silica or rutile prism, a HeNe laser and detector, and a rotary stage. The laser is aligned such that the beam strikes the face against which the sample is pressed internally to the prism, and is then reflected out to the detector. The prism, sample and detector are then rotated together such that the laser is incident on the same spot at the prism-sample

interface throughout, and the reflected intensity is recorded as a function of incident angle. The experimental setup is depicted in the figure 2.5:

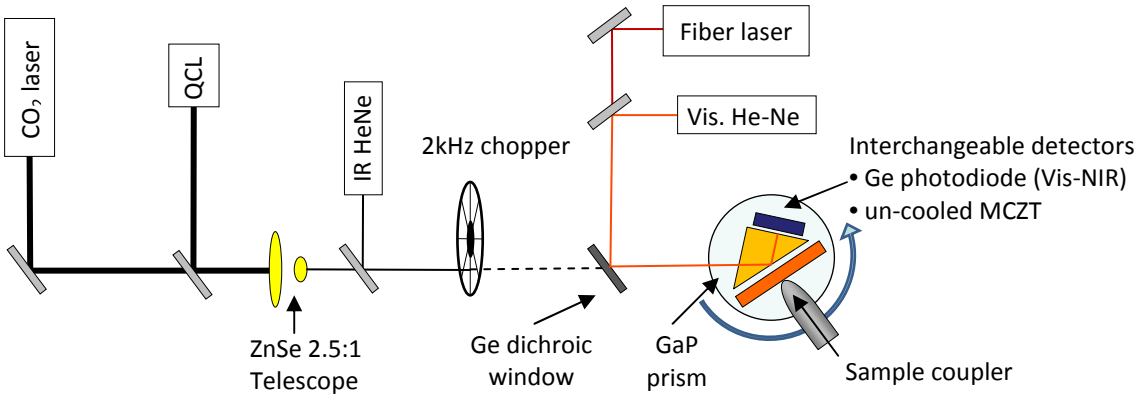

Figure 2.5: Layout of Metricon model 2010 prism coupler with modifications for IR refractive index measurements

In order to provide the ability to measure refractive wavelength at longer wavelengths, additional discreet laser sources at 1.55. 3.39. 5.35 µm and a tunable CO_2 laser covering 9.3 to 10.6 µm were added and aligned to be collinear with the 632.8 nm HeNe. Additionally, the prism was changed from rutile to GaP in order to provide the correct transmission range, and to keep the refractive index of the prism higher than those of the test samples. Finally, a mercury-cadmium-zinc telluride detector was added in order to expand the detection range through the mid-IR (3-10 µm). Sufficient signal to-noise ratio was achieved by optically chopping the IR lasers at 2 kHz and recovering the signal from the detector using a lock-in amplifier. Shown in Figure 2.6 below is a simulated plot of intensity versus incident angle for bulk and thin film samples.

`

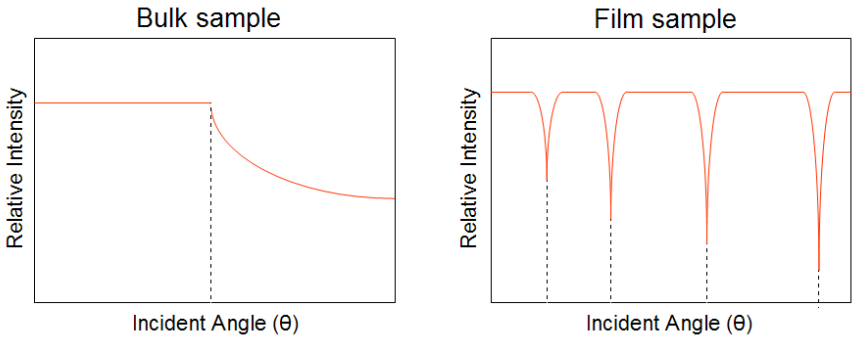

Figure 2.6: Illustration of photodetector intensity output plots as a function of incident angle (θ) for bulk and thin film samples during prism coupling measurements.

In the case of a bulk glass sample with a lower refractive index than that of the prism, the laser beam is reflected from the face of the prism, into the detector, until the incident angle drops below the critical angle for total internal reflection, at which point it is coupled evanescently across the gap and into the sample. In the case of a thin film sample, a series of modes are formed, again below the critical angle where the light is guided within the film, which allows the calculation of both refractive index and thickness from the pattern of mode angles. Since the absolute intensity of the light is not needed for the calculation of refractive index, but only the angle of the prism at which coupling occurs, the absolute accuracy of this measurement technique can reach as high as ±0.0001 refractive index units (RIU) or 100 ppm.

A limitation of the prism coupling technique for the determination of thin film refractive indices is that multiple modes must be coupled in order to allow a unique solution to both refractive index and thickness. As a result, the film thickness must be close that the wavelength of light.

`

In order to calculate the refractive index of thin films at IR wavelengths, a separate program was developed which performs an analysis of the coupled mode angles. This is accomplished be recording the intensity values as a function of incident angle, and determining the location of the minima observed in the signal. The effective index of the corresponding guided mode (N_m) for each minimum is determined from the incident angle of the mode (θ_m), the prism base angle (ε), and the prism refractive index (n_p), using the following relation [107]:

$$N_m = \sin\theta_m \cos\varepsilon + \left(n_p^{\,2} - \sin^2\theta_m\right)^{1/2} \sin\varepsilon \qquad (2.12)$$

It is known that coupled modes occur at discreet incident angles given by [107],

$$k_{xf} W + \phi_{fs} + \phi_{ft} = m\pi \qquad (2.13)$$

where m is the integer mode order, W is the film thickness, λ is the wavelength of the measurement, and k_{xf} is the effective optical density of the mode, given by [107]

$$k_{xf} = \left(\frac{2\pi}{\lambda}\right)\sqrt{n_f^{\,2} - N_m^{\,2}} \qquad (2.14)$$

Finally, the Fresnel phase shifts which occur on reflection from the interface between the film and substrate, or film (ϕ_{fs} and ϕ_{fa} respectively) follow the relation [107]:

$$\phi_{fi} = -\tan^{-1}\left(\frac{N_m^{\,2} - n_i^{\,2}}{n_f^{\,2} - N_m^{\,2}}\right) \qquad (2.15)$$

In order to find a single value for n_f and W which solves the set of transcendental equations corresponding to each observed mode, the method first described by Kirsch [107] is used. An initial guess value for the refractive index is calculated from the position of the first two minima in the following equation:

`

$$n_f = \sqrt{\frac{4\left(N_0^{\,2} - N_1^{\,2}\right)}{3}} \tag{2.16}$$

Once the estimated film index is known, approximate values of the two phase shifts ϕ_{fs} and ϕ_{fa} may be calculated. The following relationship between effective mode index (N_m) mode order number (m) may then be fit using linear regression through the following relation.

$$y_m = C_1 x_m + C_2 \tag{2.17}$$

where:

$$y_m = N_m^{\,2}, \tag{2.18}$$

$$C_1 = -(\lambda/2W)^2, \tag{2.19}$$

$$C_2 = n_f^2, \tag{2.20}$$

$$x_m = \left[m - \frac{\left(\phi_{fs} + \phi_{ft}\right)}{\pi} \right]^2 \tag{2.21}$$

The refractive index may then be calculated from the x_m intercept, and the thickness from the slope of the line. The film index derived from regression is then used to improve the initial estimates of the values of the ϕ_{fs} and ϕ_{ft} phase shifts and the regression is performed again. This iterative refinement is continued until the change in n_f between each iteration is significantly less than the expected precision of the index measurement, 1×10^{-5} RIU for example, which is primarily limited by the accuracy of the stage used to rotate the prism, and the collimation of the laser.

`

The other technique used in this study to quantify the refractive index of thin film is based on the method developed by Swanepoel [108]. This method uses interference effects which occur due to multiple reflections between the interface of a thin film and the air and to the substrate, when the thickness of the film is close to the coherence length of the light. This effect produces an interference pattern in the transmission spectrum of the film, which is demonstrated Figure 2.7 below.

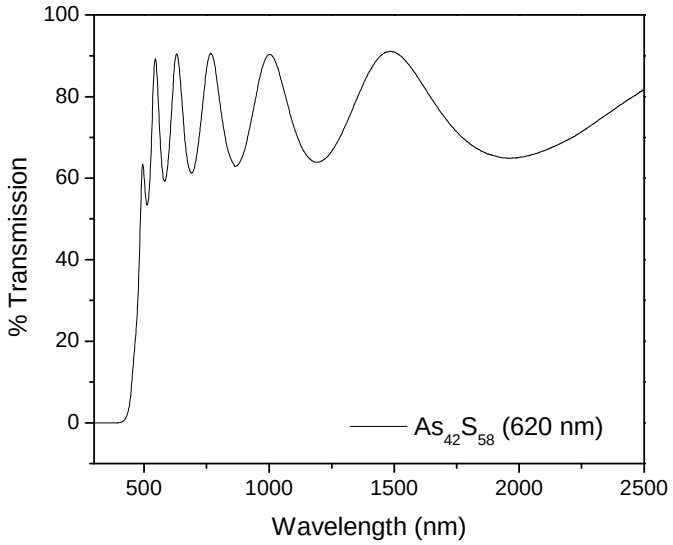

Figure 2.7: Transmission spectrum of a 620 nm thick $As_{42}S_{58}$ glass thin film deposited on a microscope slide using thermal evaporation

At wavelengths longer than the band gap, if it is assumed that absorption and scattering are negligible, the maximum transmission values are expected to correspond to the transmittance of the substrate alone, while the minimum transmission occurs where when the reflections from the two surfaces of the film interfere constructively. The refractive index of the film (n) may then be calculated from the transmittance values [108].

`

$$n = \left[N + \left(N^2 - s^2\right)^{1/2}\right]^{1/2} \quad (2.22)$$

given: $N = 2s\frac{T_M - T_m}{T_M T_m} + \frac{s^2 + 1}{2}$ (2.23)

where T_M and T_m are the transmission values at the maxima and minima, and s is the refractive index of the substrate. The thickness of the film may also be determined, by examining the spacing between adjacent maxima and minima, using the following equation:

$$2nd = m\lambda \quad (2.24)$$

where d is the film thickness, λ is the wavelength, and m is the order number. In this case, the maxima may be expected to occur at integer values of the order number, minima occur at half integers.

2.2.4 Structural properties

X-ray diffraction

Samples which are at least partially crystalline lend themselves to X-Ray diffraction (XRD) analysis, which allows the identification of the crystalline phase. In this technique, an X-ray beam with a wavelength of 0.15418 nm is generated from an X-ray tube with a copper anode. This beam passes through a slit for collimation and is incident on the sample, which may be a polished bulk glass, thin film or powder, and a scintillation counter detects the reflected intensity. The incident angle of the beam and the angle of the detector are then increased together. If a periodic array of atoms exists in

the sample, the X-Ray beam may be diffracted when the diffraction from each plane of the array interferes constructively, as illustrated below.

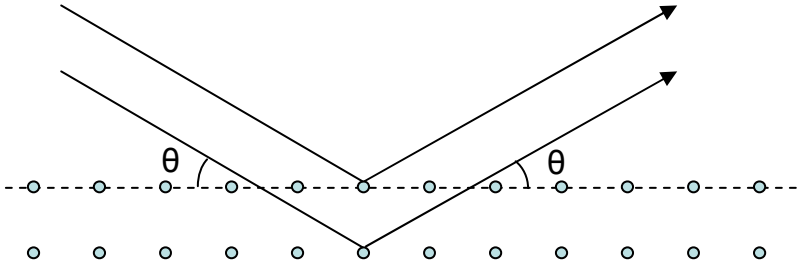

Figure 2.8: Representation of X-Ray diffraction from atomic lattice planed during XRD measurement.

The condition of constructive interference exists when the path length difference of the beam diffracted at any one plane and the one below it is equal to an integer multiple of the wavelength (λ). Since the path difference is dependent on the incident angle (θ), and on inter-plane spacing (d) given by the well known Bragg equation, shown below.

$$n\lambda = 2d\sin\theta \qquad (2.24)$$

Powdered diffraction patterns were acquired over the range of 5° to 80° with a step size of 0.02° and an integration time of 2 seconds per step. The lack of a well defined diffraction pattern may indicate that a sample is either fully amorphous or that crystallite size is too small to be observed using this technique, generally bellow a few nm, due to line broadening for small particle sizes [109]

Micro-Raman spectroscopy

`

Raman scattering is the inelastic scattering of photons by optical-mode phonons. Energy equivalent to that of the vibrational modes of the lattice may be gained or lost by the photon when it is scattered. As a result, the scattered photon is of a different wavelength than the incident photon, and the wavelength shift is indicative of the vibrational energies of chemical bonds within the glass. The scattered photon may have either a higher energy or lower energy and therefore frequency as compared to the incident photon, referred to as Stokes or anti-Stokes shifts respectively. The Raman scattering process involves the coupling between low frequency vibrations of the electron cloud surrounding an atom as the position of its nucleus changes within the lattice due to thermal energy, with high frequency vibrations induced by the AC electric field of the light. Since this phenomenon is dependent on the electric field intensity of the light, the Raman scattering process is non-linear, and generally requires a high-intensity light source to be observed. Also, since the energy shift is equal to the lattice vibrational energy, small when compared to optical photon energies, scattered photons have a similar wavelength to that of the incident photons. These factors make lasers an ideal excitation source for Raman spectroscopy due to their high intensities and short wavelength bandwidths.

Raman spectrometers include a laser excitation source, a wavelength dispersive detector (typically a grating coupled CCD array), a specially designed optical filter which prevents the excitation wavelength from reaching the detector, but allowing wavelengths very close to that of the laser to pass through. Micro-Raman spectrometers also utilize a microscope objective, typically in a confocal arrangement, in order to focus the incident

laser light. This serves to increase the laser intensity, and therefore the scattered signal, but may also be used to allow high spatial resolution, and to allow normalization of the absolute scattered intensity.

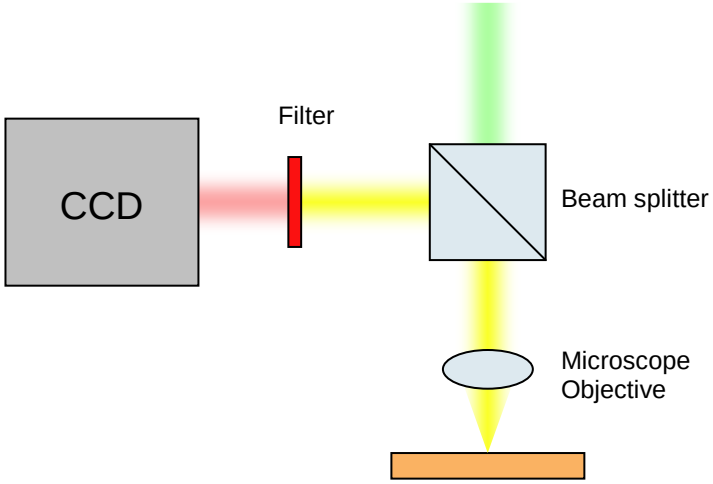

Figure 2.9: micro-Raman spectrometer in backscattering geometry

A common source of interference is fluorescence from the sample under the excitation wavelength. The fluorescence process is generally much more efficient than Raman scattering, and may cause saturation of the detector system without measurement of the Raman signal. A second concern in the case of chalcogenide glass is their photo-sensitivity. If the excitation wavelength is close to the absorption band gap of the glass, or if the intensity is very high, the bonding within the material may be changes by interaction with the laser light [110]. Since the glasses measured in this study have band gaps in the visible part of the spectrum, near infrared laser excitation at 785 nm with relatively low (< 5 mW) power were used throughout this study. Raman spectra for this study were recorded using two systems: a Kaiser Hololab 5000R (KOSI) Raman spectrometer with Raman microprobe attachment in collaboration with the MIT

`

microphotonics lab, and SENTERRA dispersive micro-Raman spectrometer (Bruker Optics *http://www.brukeroptics.com*) in collaboration with the Clemson Conservation Center. Both systems operate in backscatter geometry, and employ a holographic notch filter and grating-coupled CCD.

CHAPTER THREE

Compositional Dependence of Bulk Glass Properties

In this first part of the results section, the characterization of the bulk glasses is reported. It will be divided into sections discussing the i) physical, thermal and optical properties, ii) structural characterization, and iii) dissolution behavior.

As discussed in the introduction section, the two primary glass forming elements in the chalcogenide system are Ge and As. Because Ge tends to form 4-coordinated units while As forms 3-coordinated units, the choice of glass former impacts many of the characteristics of the glass, such as hardness, T_g and crystallization temperatures, thermal expansion, etc. Arsenic is by far the best glass former in the chalcogenide system in terms of stability against crystallization, and in fact, most crystalline samples of the stoichiometric compound orpiment (As_2S_3) are of geologic origin because slow crystallization kinetics prevent convenient laboratory preparation. In comparison, GeS_2 is quite difficult to prepare in the glassy state, requiring rapid cooling methods such as roller quenching, resulting in most authors either choosing a non-stoichiometric composition (commonly $Ge_{30}S_{70}$) or adding an intermediate such as Sb in order to retard crystallization kinetics enough to allow air quenching [111, 112].

The use of intermediates, which modify the structure of the glass, also allows tuning of the glass properties to suit the application. This can include increasing or decreasing the refractive index or thermal expansion, nonlinear optical properties [14, 113], or even photosensitivity to laser exposure [1, 114]. Thus we can see that

understanding the effect of intermediates on the properties and structure of the glass, and as well as the impact on solution processing are important. In this first part of the study we will examine a series of As-S based glasses containing either Ge or Sb as an intermediate, and a Ge-S based glass containing Sb as an intermediate.

3.1 Physical and thermal properties

Table 3.1 shows the physical and thermal properties of the glasses $Ge_{23}Sb_7S_{70}$, $As_{42}S_{58}$ $As_{36}Ge_6S_{58}$ and $As_{36}Sb_6S_{58}$.

Table 3.1: Physical and thermal properties of the investigated glasses

Nominal composition	**EDS analysis** at.% (±2)	**Density** g/cm^3 (±0.02)	**H_V** kg/mm^2 (±2)	**T_g** °C (±2)	**CTE** ppm/°C (±1)
$As_{42}S_{58}$	$As_{42}S_{58}$	3.20	112	210	22.6
$As_{36}Ge_6S_{58}$	$As_{34}Ge_8S_{59}$	3.15	125	220	21.4
$As_{36}Sb_6S_{58}$	$As_{37}Sb_6S_{57}$	3.41	117	208	23.0
$Ge_{23}Sb_7S_{70}$	$Ge_{23}Sb_7S_{70}$	2.93	153	305	17.1

One can see that in the As-based system, replacement of As by Ge causes an increase of T_g and hardness and a decrease in the density and coefficient of thermal expansion (CTE). Sb induces an increase in the density but no significant change in T_g and only a slight decrease in hardness. In comparison with the As-based glasses, the germanium-based glass ($Ge_{23}Sb_7S_{70}$) possesses a significantly higher T_g and hardness, with a decreased density and CTE.

3.2 Optical properties

Shown in Figure 3.2a below is the UV-Vis absorption spectrum of the glasses presented in Table 3.1; note that the effect of Fresnel reflectance has been removed.

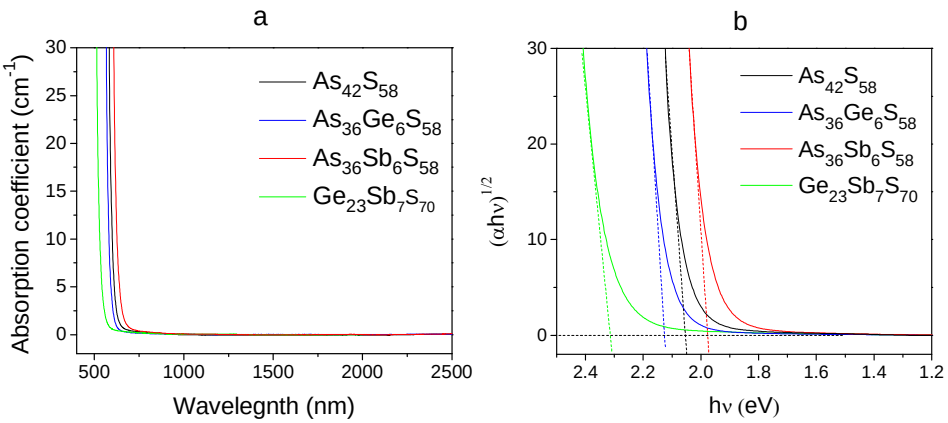

Figure 3.1: UV-Vis absorption spectra, and Tauc band gap plots for the investigated bulk glass compositions.

This figure shows that the glasses are highly transparent throughout the near-IR, and that small shifts of the band gap occur with changes in composition. The low absorption region (0-10 cm^{-1}) is expected to be dominated by the exponential Urbach tail which is caused by defect states near the band gap [105], while the high absorption region (>10 cm^{-1}) is dominated by promotion of electrons from the conduction to valence band (HOMO to LUMO molecular orbital transition). As the band gap in amorphous semiconductors is known to be indirect, α is expected to follow the form [115]:

$$\alpha h\nu = B\left(h\nu - E_g\right)^2 \qquad (3.1)$$

Through linear regression of $(\alpha h\nu)^{1/2}$ in the high-absorption region the intercept gives the band gap energy (E_g). Figure 3.1b shows the linear regression from the 4 compositions shown. The replacement of As by Sb induces a decrease (red shift) of the band gap from

2.07 to 1.97 eV, while introduction of Ge induces a slight increase to 2.13 eV. As compared to the As-based compositions, the Ge based glass shows a significant blue shift of band gap to 2.32 eV.

The refractive index of the bulk glasses was measured using prism coupling. Figure 3.3 presents the refractive index dispersion over the spectral range of 0.6 to 10.6 µm. Note that the error bars are within the size of the data points (±0.0004).

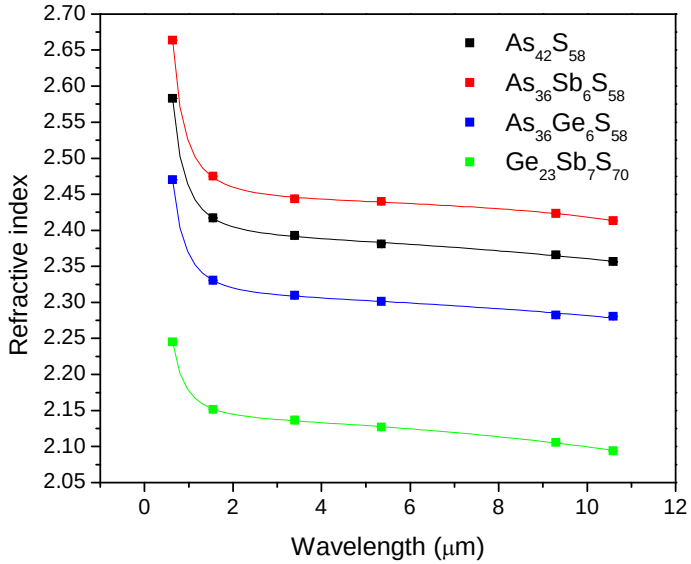

Figure 3.2: Visible and infrared refractive index data and calculated Sellmeier dispersion curves measured by prism coupling.

It is clear from the figure that the refractive index of As-based glasses increases across the entire visible through mid-IR region upon replacement of As by Sb and decreases with replacement by Ge, while the Ge-based glass has significantly lower index compared to all of the As-based compositions. In accordance with previous publications, [116] the data was fit using a Sellmeier dispersion curve having the form:

`

$$n^2 = 1 + \frac{A\lambda^2}{\left(\lambda^2 - B^2\right)} + \frac{C\lambda^2}{\left(\lambda^2 - D^2\right)} + \frac{E\lambda^2}{\left(\lambda^2 - F^2\right)} \qquad (3.2)$$

Where n is the refractive index λ is the wavelength in μm and A through F are fitting constants, which are summarized for reference in Table 3.2 below.

Table 3.2: Sellmeier dispersion constants for the studied glass compositions.

Composition	**Sellmeier fitting constant**					
	A	**B**	**C**	**D**	**E**	**F**
$As_{36}Sb_6S_{58}$	4.47337	0.27337	0.48540	0.27338	0.98390	82.50170
$As_{42}S_{58}$	4.34696	0.26107	0.35981	0.26093	6.79827	70.90834
$As_{36}Ge_6S_{58}$	4.14747	0.24772	0.17273	0.24754	4.66020	63.88099
$Ge_{27}Sb_7S_{70}$	3.25221	0.22628	0.31192	0.01989	3.02455	44.92886

The non-linear refractive index (n_2) and nonlinear absorptivity (β) were measured using the Z-scan technique at 1064 nm, the results of which are summarized along with the non-linear figure of merit (F) [61] in Table 3.3 below. In this case, increasing F predicts higher performance of the glass in nonlinear optical applications, which generally require high nonlinearity but with low optical loss [61].

Table 3.3 Nonlinear optical constants at 1064nm for the studied compositions.

Nominal composition	**n_2** ($x10^{-18}$) m^2/W	**$n_2/n_{2silica}$**	**β** ($x10^{-11}$) m/W	**F** $(n_2/2\beta\lambda_g)$	**$E_g/h\nu$**
$As_{42}S_{58}$	3.8 ±0.6	127	0.2 ±0.1	0.9	1.78
$As_{36}Ge_6S_{58}$	3.2 ±0.8	107	0.1 ±0.1	1.4	1.83
$As_{36}Sb_6S_{58}$	4.7 ±0.8	157	0.45 ±0.15	0.5	1.69
$Ge_{23}Sb_7S_{70}$	1.7 ±0.2	57	< 0.1	> 0.8	1.99

One can see that both β and n_2 increase with Sb substitution in the As-based glass and slightly decrease with Ge substitution, while the Ge-based composition has a significantly reduced nonlinear index, but β was too small to be measured. As we have shown in previous publications, the nonlinear optical constants are generally related to the

`

proximity of the absorption band gap to the measurement wavelength [113]. For this reason, the ratio of band gap energy (E_g) determined from UV-Vis spectroscopy to the photon energy at the Z-scan measurement wavelength (1064 nm) is also shown. It can be seen that n_2 and β both decrease with an increase of $E_g/h\nu$, while the nonlinear figure of merit increases for the As-based glasses.

3.3 Structural characterization

Chalcogenide glasses are well known for infrared transparency, making infrared spectroscopy of little use for their structural characterization. However, since the most common impurities in these materials are carbon, oxygen, and hydrogen, IR spectroscopy can be used to evaluate the presence of these species. Shown in the figure below, are the FTIR spectra of the investigated glasses in this study.

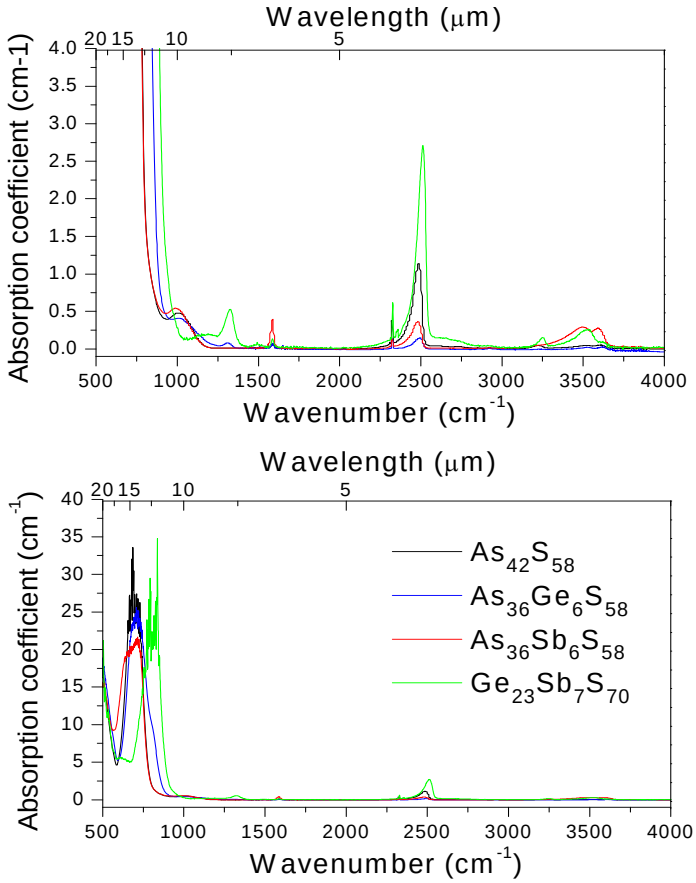

Figure 3.3: FTIR spectra of the investigated bulk glasses.

One can observe several small bands in the spectra, in the range of 4000 to 800 cm^{-1}. The high frequency (>2000 cm^{-1}) bands above are related to hydrogen impurities, due to the low atomic mass. The largest feature is a relative sharp asymmetric band near 2500 cm^{-1}, related to S-H bond stretching [117], while the broad feature near 3500 cm^{-1} is related to O-H either connected to the network as in Ge-OH or As-OH or free as in interstitial H_2O [118]. An additional peak at 1600 cm^{-1} is also attributed to H_2O [117, 118]. At low frequencies, one band appears at 1260 cm^{-1} only in the spectra of $Ge_{23}Sb_7S_{70}$ and $As_{36}Ge_6S_{58}$, caused by Ge-O bond stretching, and one near 1000 cm^{-1} attributed to networked As-O bond stretching in the three As-based compositions [117]. A very strong

absorption band at 700-800 cm^{-1} is expected to be caused both by extrinsic oxide impurity absorptions and intrinsic multi-phonon absorption [117]. This leaves a useful IR transparency range of approximately 10 µm, with appropriate purification.

As we have shown, useful information about the bonding within these materials is difficult to obtain from IR spectra of these glasses, and their amorphous structures preclude the use of X-Ray diffraction analysis. Therefore, the primary tool used to elucidate the bonding structure of the glasses is Raman spectroscopy. In particular, micro-Raman was employed in order to allow comparison of bulk materials to thin films. Low intensity near-IR excitation (λ_{exc} = 785 nm) is preferred due to absorption at visible wavelengths and the photo-sensitivity that results. The micro-Raman spectra of the bulk glasses are presented in Figure 3.4.

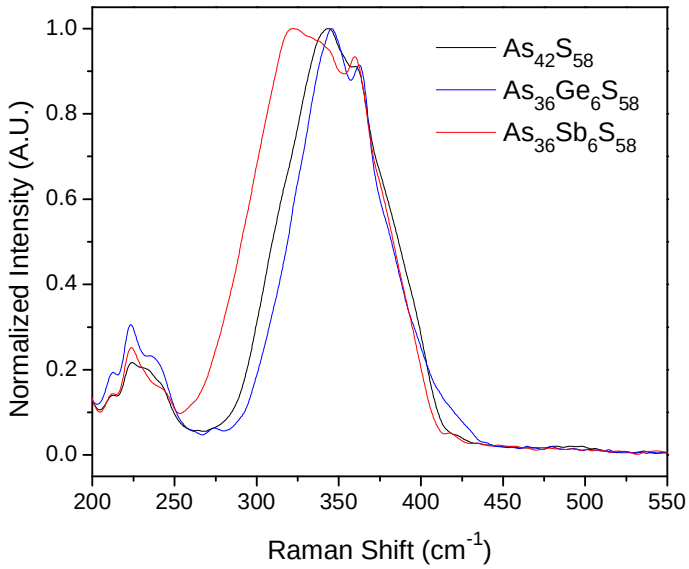

Figure 3.4: micro-Raman spectra (λ_{exc} = 785nm) for the As-based bulk glasses.

The main band of $As_{42}S_{58}$, a slightly chalcogen deficient glass close to the stoichiometric composition (As_2S_3), is attributed to vibrations of $AsS_{3/2}$ pyramidal units, including the symmetric and asymmetric stretches of the AsS_3 units at 310 and 345 cm^{-1} respectively [119], and stretching motion of S in $S_{2/2}As\text{-}S\text{-}As\text{-}S_{2/2}$ bridges at 380 cm^{-1} [119]. Several additional small bands appear in the low frequency region (200-250 cm^{-1}) which are related to As-As bonds either in $S_{2/2}As\text{-}As\text{-}S_{2/2}$ network units (220 cm^{-1}) [120] or isolated As_4S_4 molecules (235 cm^{-1}) [121, 122]. Finally a small band near 490 cm^{-1} can be seen in the spectrum of $As_{42}S_{58}$ (Fig. 3.4) which is related to S-S homopolar bonds in $S_{2/2}As\text{-}S\text{-}S\text{-}AsS_{2/2}$ disulfide bridges [123]. Upon replacement of As by Sb, the main band broadens significantly and shifts to lower wavenumber, due to the appearance of a band at 290 cm^{-1} related to $SbS_{3/2}$ pyramids [119]. Concurrently, replacement of As by Ge sharpens the main band and shifts it slightly to higher wavenumbers, due to the overlap of the symmetric stretch of $GeS_{4/2}$ tetrathedra at 340 cm^{-1} [124]; a small shoulder at 420 cm^{-1} also appears, attributed to $S_{3/2}Ge\text{-}S\text{-}GeS_{3/2}$ bridges [125]. The appearance of a shoulder of the main bands of both substituted glasses at 365 cm^{-1} corresponds to an increase of the band at 220 cm^{-1}, both attributed to As_4S_4 [121], and a small band near 270 cm^{-1}, found only in the spectrum of $As_{36}Ge_6S_{58}$, is attributed to As_4S_3 molecules, also containing As-As bonds [122]. The above Raman band assignments are summarized in Table 3.4.

`

Table 3.4: Summary of Raman band assignments

Raman shift (cm^{-1})	**Assignment**	**Ref.**
210	B_1 stretching mode of As_4S_4 molecule	[121, 122]
225	As-S-As bending (E) mode of As_4S_4	[121, 122]
365	A_1 breathing motion of As_4S_4 molecule	[121]
235	Stretching of $S_{2/2}As\text{-}AsS_{2/2}$ homopolar network bonds	[120]
270	A_1 mode of As_4S_3 molecule	[122]
310	Asymmetric stretch of $AsS_{3/2}$ network units	[119]
345	Symmetric stretching of $AsS_{3/2}$	[119]
380	T_2 Stretching motion of $S_{2/2}As\text{-}S\text{-}AsS_{2/2}$ network bridges	[119]
330	A_1 Symmetric stretching mode $GeS_{4/2}$ (corner-shared)	[125]
340	A_1 Symmetric stretching mode GeS_4 (disulfide-bridged)	[124]
370	A_1^c mode of $Ge_2S_2S_{4/2}$ units (2 edge-shared tetrahedra)	[125]
400	F_2 Anti-symmetric stretch of GeS_4	[125]
425	T_2 stretching motion of $S_{3/2}Ge\text{-}S\text{-}GeS_{3/2}$ bridges	[124]
290	Asymmetric stretch of $SbS_{3/2}$ units	[119]
475	A_1 symmetric breathing mode of S_8 rings	[123, 126]
490	S-S stretch in S_n bridging chains (disulfide bridges)	[123, 126]

As noted above, the network of the base glass ($As_{42}S_{58}$) is composed primarily of interconnected $AsS_{3/2}$ units which are expected to form a 2-dimensional sheet type structure [127]; however, a small number of homopolar "wrong" As-As bonds are observed due to the slight stoichiometric excess of As in relation to S. While there are many ways to consider the different bonding forms occurring within the glass, we believe that in the context of the current study the most instructive may be to consider the molecular units. In the case of the base glass, the two fundamental molecular units are $AsS_{3/2}$ units, of which most of the network is comprised, and $AsS_{2/2}$ units, which are the basis for the "wrong" bonds in the glass. It can be seen that $S_{2/2}As\text{-}AsS_{2/2}$ network homopolar bonds are formed of two $AsS_{2/2}$ units, and As_4S_4 molecules are formed from four of these units bonded together. Because the S atoms are shared with neighboring

units, each $AsS_{3/2}$ unit contains 1.5 effective S atoms while $AsS_{2/2}$ contains 1 S atom. The relative numbers of these units may then be unambiguously calculated from the composition by solving a set of linear equations. If X is defined as the number of $AsS_{3/2}$ units, and Y is defined as the number of $As_{2/2}$ units, then:

$$X + Y = 42 \text{ (As atoms per 100)} \quad (3.3)$$

$$1.5X + Y = 58 \text{ (S atoms per 100)} \quad (3.4)$$

Solving these equations gives 32 $AsS_{3/2}$ units and 10 $AsS_{2/2}$ per 100 atoms, or 76% and 24% respectively.

As-As homopolar bonds have previously been shown to form preferentially over Ge-Ge or Sb-Sb homopolar bonds in ternary glasses [119, 128, 129], primarily due to differences in bond energies [130] (summarized in Table 3.5) and in this case also due to the relatively low concentration of Ge and Sb.

Table 3.5: Bond dissociation energies for homopolar and heteropolar bonds

Bond Type	Dissociation Energy (kJ/mol)
As-S	380
Ge-S	534
Sb-S	369
S-S (S_8)	265
As-As	386
Ge-Ge	264
Sb-Sb	301

We can therefore extend the molecular unit calculations to the substituted glasses by assuming that only $SbS_{3/2}$ or $GeS_{4/2}$ units are added upon substitution, and letting the number of these units be given as the variable Z in:

$$Z = 6 \quad (3.5)$$

`

$$X + Y = 36 \quad (3.6)$$

$$1.5X + Y + 1.5Z\ (SbS_{3/2}) = 58 \quad (3.7)$$

or

$$1.5X + Y + 2Z\ (GeS_{4/2}) = 58 \quad (3.8)$$

Solving for $As_{36}Sb_66_{58}$ (Equations 3.5, 3.6 and 3.7) gives 62% $AsS_{3/2}$, 24% $AsS_{2/2}$ and 14% $SbS_{3/2}$, while for $As_{36}Ge_6S_{58}$ (Equations 3.5, 3.6 and 3.8) it gives 48% $AsS_{3/2}$, 38% $AsS_{2/2}$ and 14% $GeS_{4/2}$. From this, we can see that substitution decreases the number of fully coordinated As units which can be formed, thereby increasing the relative number of As-As homopolar bonds. As each $AsS_{3/2}$ unit contributes 3 As-S bonds to the network while each $AsS_{2/2}$ contributes 2 As-S and 0.5 As-As bonds, the expected bond statistics may also be determined using this method, giving 4% As-As bonds in $As_{42}S_{58}$, 5% in $As_{36}Sb_6S_{58}$ and 8% in $As_{36}Ge_6S_{58}$. Finally, a third type of As-containing unit, S-$AsS_{2/2}$, should also be considered. Two of these units would be expected to form an S-S homopolar bond (in $S_{2/2}$As-S-S-$As_{2/2}$), which may be expected in small concentrations due to randomization of bonding in the amorphous network. Each S-$AsS_{2/2}$ unit formed results in the formation of an additional $AsS_{2/2}$ unit. These statistics, summarized in table 3.6, are in good agreement with the evolution of the Raman spectrum of the As-based glasses with composition. It is also important to note that these additional As-As bonds found in the substituted glasses occur primarily as As_4S_4 molecules, as evidenced by the large intensity at 220 and 365cm^{-1} [121, 122], (and some As_4S_3 in the case of $As_{36}Ge_6S_{58}$) which are not present in significant quantity in the base glass.

`

The Raman spectrum of $Ge_{23}Sb_7S_{70}$, shown in Figure 3.5 possesses a broad main band centered at 330 cm^{-1} with an extended shoulder from 370 to 425 cm^{-1}. There are two additional low-intensity features near 250 and 480 cm^{-1}.

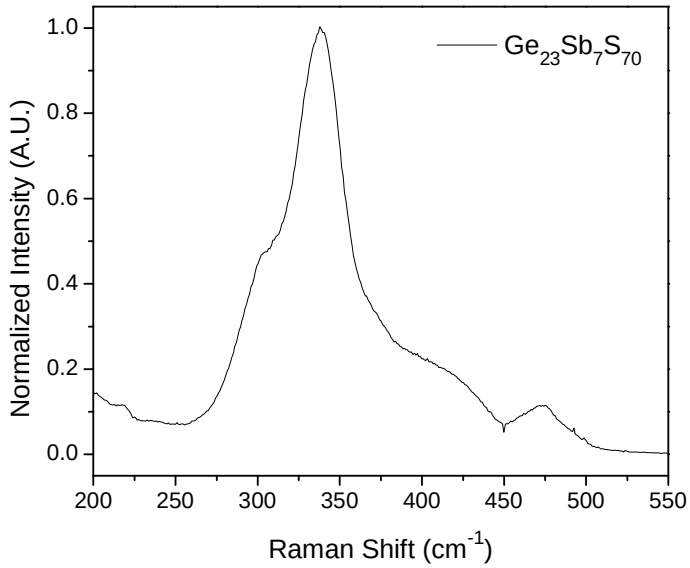

Figure 3.5: micro-Raman spectrum (λexc = 785nm) of Ge23Sb7S70 bulk glass.

Also explained in detail elsewhere [111], the main band, centered near 330 cm^{-1}, is formed primarily by two superimposed bands at 340 and 330 cm^{-1} which correspond to the A_1 mode of disulfide-bridged or "isolated" GeS_4 [124] and corner-sharing $GeS_{4/2}$ [125] tetrahedral units respectively. A band near 300 cm^{-1}, also present, is attributed to the E mode of $SbS_{3/2}$ pyramids [126]. The shoulder of the main band at higher wavenumbers is formed by three bands near 370, 400, and 425 cm^{-1}, respectively attributed to the A_1^c "companion" mode of edge-sharing $Ge_2S_2S_{4/2}$ bi-tetrahedra [125], the anti-symmetric motion (F_2) of $GeS_{4/2}$ units [125], and the T_2 motion of bridging S

`

atoms between corner-shared tetrahedral in $S_{3/2}Ge\text{-}S\text{-}GeS_{3/2}$ [124]. These units are illustrated in Figure 3.6 for reference.

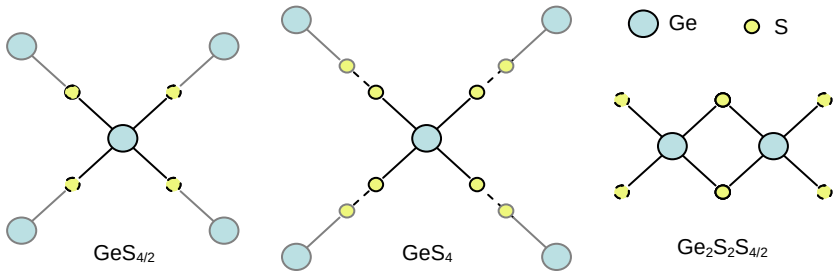

Figure 3.6: Diagram of GeS_4-based network units, dashed lines show elements which are shared with a neighboring unit.

As for the As-based glasses, it is possible to describe this glass in term of molecular units, and to calculate their relative concentrations from the composition of the glass. However, as we will show, the situation in this glass is much more complex. In this case, there would appear to be $SbS_{3/2}$ units and $GeS_{4/2}$ units forming the majority of the network; however, a large excess of S is found in this glass leads to the formation of S-S homopolar bonds. The thermodynamically preferred for of elemental S at room temperature is the S_8 ring. It may however, be expected that smaller S-S groupings such as Ge-S-S-Ge bridges or S_4 clusters would be more likely in the glass due to the low probability of eight free S atoms (not bonded to either Sb or Ge) coming together in the necessary geometry with no Ge Sb nearby. S_8 rings would therefore only be likely for glasses with very large excesses of S. Since the large majority of network units are centered on Ge, which also has a higher coordination number, we may further expect most of these disulfide bridges to form on Ge tetrahedra due to the relatively low Sb concentration. We may therefore expect units such as $S\text{-}GeS_{3/2}$ units which can pair to

form a single S-S bond. If these same method used for the As-based glasses is extended to this glass, we may then calculate the relative numbers of these units using the system:

$$1.5X + 2Y + 2.5Z = 70 \quad (3.9)$$

$$Y + Z = 23 \quad (3.10)$$

$$X = 7 \quad (3.11)$$

Where Z is the number of $SbS_{3/2}$ units, X is the number of $GeS_{4/2}$ and Z is the number of S-$GeS_{4/2}$. In fact, it is not possible to solve this system (for positive values of X. Y and Z). Even if we consider that all Ge units have an S-S bridge connected to them (only S-$Ge_{3/2}$ units) there are still not enough Ge atoms to account for all of the S atoms. This serves to illustrate how large the excess of S is in this glass. There is no particular reason to assume that only one S-S bond may be connected to each $GeS_{4/2}$ tetrahedron, and in fact, some of these units may be connected into the network entirely through S-S bonds. This is what was referred to above as an "isolated" GeS_4 tetrahedron. We can more accurately expect a mix of units having from 0 to 4 S-S bridges at their corners (though each is only ½ of a full S-S bond). Because the A_1 mode of $GeS_{4/2}$ is found at 330 cm^{-1} and that of GeS_4 is found at 340 cm^{-1}, the main band should in fact be formed of the overlap of the A_1 modes of all 5 types of unit with varying intensities, which would be impossible to reliably deconvolve. For the purpose of simplicity, therefore, we will use only the two extremes of fully isolated GeS_4 and fully S-shared $GeS_{4/2}$ units, understanding that the relative numbers of these also represent the relative numbers of Ge-S-Ge and Ge-S-S-Ge bridges. Since the vibration of Ge-S-Ge bridges is found at

425cm^{-1} while that of Ge-S-S-Ge bridges is at 475cm^{-1}, this formalism should be much easier deconvolve. Rewriting the equations for unit counting appropriately, we have:

$$1.5X + 2Y + 4Z = 70 \quad (3.12)$$

$$Y + Z = 23 \quad (3.13)$$

$$X = 7 \quad (3.14)$$

This gives: 7 (23%) $SbS_{3/2}$ units, 16.25 (54%) $GeS_{4/2}$ units and 6.75 (23%) GeS_4 units per 100 atoms; this suggests that approximately half of the bridges between Ge tetrahedra are of the disulfide (S-S) type. Finally, as discussed above, because there is such a large excess of S in the glass it is not truly valid to assume that absolutely no S_8 molecular rings are present. Because there is a significant intensity near 490 cm^{-1} corresponding to the breathing motion of S_8 rings, it is in fact easy to confirm. Although exact concentrations are difficult to determine without having accurate information on the Raman scattering cross-sections of the various S-S containing units, it must true be that for each S_8 ring, eight S-S network bridges must be lost (or four GeS_4 units converted to $GeS_{4/2}$). This type of conversion of disulfide bridges to S_8 rings has been observed during laser irradiation of this composition and is reported in detail elsewhere [131, 132]. Once again, it is possible to count the number of Sb-S Ge-S and S-S bonds using 3 Sb-S bonds for each $SbS_{3/2}$ 4 Ge-S for each $GeS_{4/2}$ and 4 Ge-S bonds plus 4 S-S bonds for each GeS_4 unit.

`

3.4 Bulk glass structure-property relationships

It is important to note that only As-As and S-S homopolar bonds are predicted for the four compositions examined in this study ($As_{42}S_{58}$, $As_{36}Sb_6S_{58}$, $As_{36}Ge_6S_{58}$ and $Ge_{23}Sb_7S_{70}$) while Sb-Sb and Ge-Ge are discounted. This is explained by examining the associated bond energies [133], which are summarized in Table 3.5 above. As we will show, the evolution of both the structure and many of the properties of the bulk glasses may be understood by examining the changes in bonding outlined above, which is controlled by composition. It is important to first consider the coordination numbers (CN) of each of the elements (As/Sb = 3, Ge = 4, S = 2) and that each element contributes 4-CN lone electron pairs to the glass. Taking 1 mole of glass to contain $100N_A$ atoms, many key parameters may be calculated including bonds statistics, average bond energies $<E_b>$, molar volume (V_{mol}), and number density of electron pairs (N_{e^-}). These are summarized in the following table.

Table 3.6: Summary of structural information including stoichiometric bonds statistics, average bond energy ($<E_b>$), molar volume (V_{mol}) and number density of lone electron pairs (N_{e^-}).

Composition	Number of bonds / 100 atoms					$<E_b>$ (kJ/mol)	V_{mol} (cm^3)	N_{e^-} (cm^{-3})
	As-S	Ge-S	Sb-S	S-S	As-As			
$As_{42}S_{58}$	116				10	380.5	16.4	5.81×10^{22}
$As_{36}Ge_6S_{58}$	92	24			16	408.7	16.6	5.52×10^{22}
$As_{36}Sb_6S_{58}$	98		18		10	380.3	15.7	6.05×10^{22}
$Ge_{27}Sb_7S_{70}$		92	21	27		458.9	17.1	5.17×10^{22}

It may be expected that some physical and thermal properties related to bond breaking, such as hardness or glass transition temperatures, may be correlated with the average

bond energy in the glass. A plot of glass transition temperature (T_g) and Vickers micro-hardness (H_V) is depicted in Figure 3.5 below for each of the glasses listed in table 3.7.

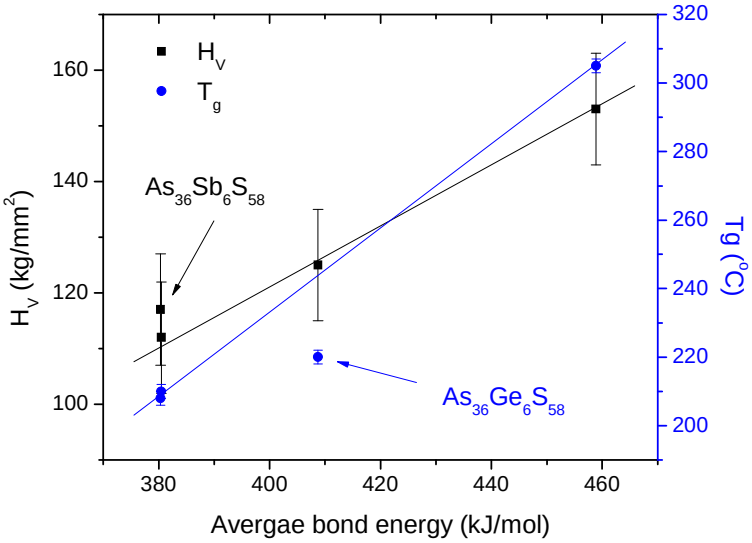

Figure 3.7: H_V and T_g as a function of average molar bond energy.

The micro-hardness appears to correspond well with the average bond energy, with the possible exception of $As_{36}Sb_6S_{58}$. It can also be seen that a linear fit of the T_g data is not appropriate for the glass $As_{36}Ge_6S_{58}$.

By examining molar volumes, it can be found that the composition $As_{36}Sb_6S_{58}$ has significantly higher packing efficiency (lower molar volume) compared to $As_{42}S_{58}$ and $As_{42}Ge_6S_{58}$, despite the relatively larger size of Sb. By correcting average bond energy with the molar volume, giving an estimation of the energy needed to break all the bonds within a given macroscopic volume, a much better fit of the hardness data is realized as shown in figure 3.7a.

`

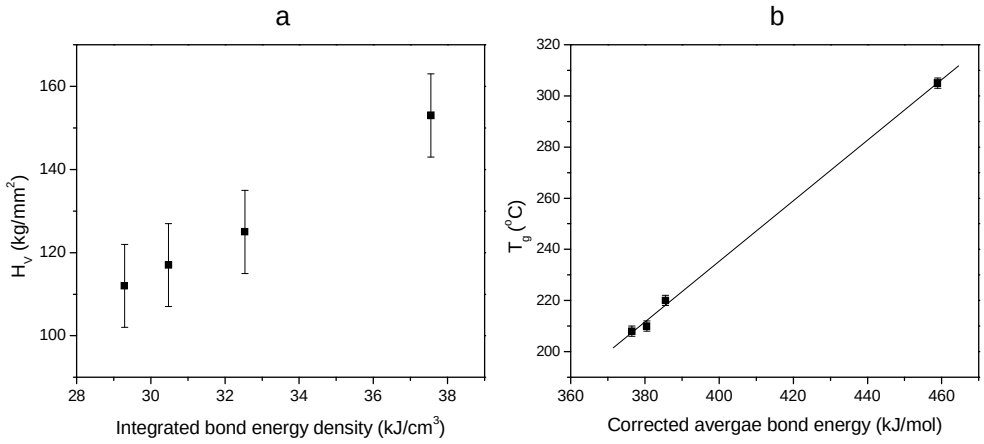

Figure 3.8: H_V as a function of bond energy density (a) T_g as a function of average bond energy, corrected to discount isolated As_4S_4 molecular units (b).

A correction of the bond energies with respect to T_g is also possible by noting from the Raman data that most of the As-As bonds in the glass are present in the form of As_4S_4 molecules, which do not participate in the network, and so are not directly involved in the glass transition. The network bond energy may then be corrected by subtracting the contribution of the excess As-As bonds which are expected to be in the form of As_4S_4, based on the compositional calculations in section 3.2. These corrected values are shown in figure 3.8b and can be seen to agree well with the predicted linear fit. This suggests that the physical and thermal properties can in fact be predicted from the structural characteristics, if these corrections are taken into account.

The linear and nonlinear optical properties may also be predicted using knowledge of the evolution of structure with composition in these glasses. For clarity, both β (nonlinear absorptivity, commonly defined as two-photon absorption[TPA]) and n_2 are shown in relation to $E_g/h\nu$ in figure 3.8(a), while the evolution of band gap energy

`

in relation to the number density of electron lone pairs (Table 3.7) is illustrated in figure 3.9(b).

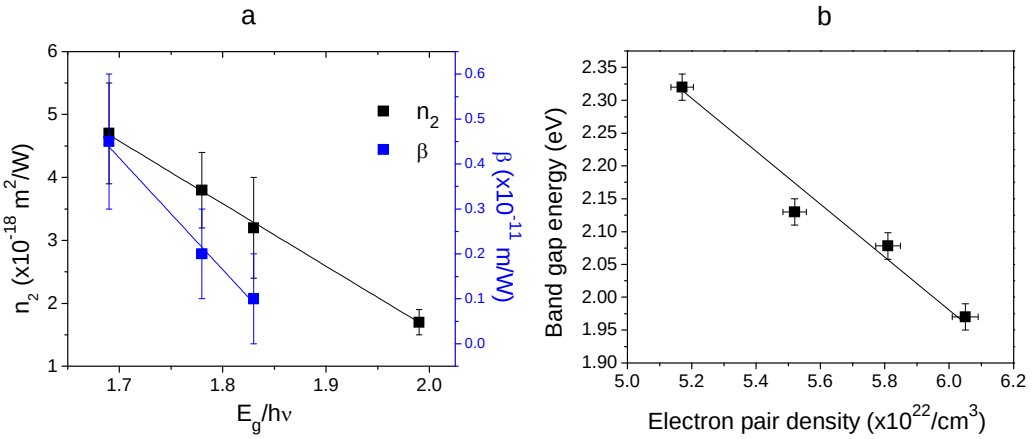

Figure 3.9: Nonlinear refractive index and nonlinear absorptivity (TPA) as a function of $E_g/h\nu$ ratio (a) and E_g as a function of electron lone pair density (b).

From the figure it is clear that a linear dependence of n_2 and β on the ratio of the band gap energy to photon energy (at 1064nm) can be found, though the uncertainty is large. This indicates that the nonlinear response is likely controlled by the proximity of the measurement wavelength to the absorption band gap. This has been postulated by numerous authors [113]. In turn, the band gap position corresponds well to the number density of lone electron pairs, thus nonlinear constants may also be attributed to this property of the glasses. Importantly, the value of β increases ~4X more slowly than that of n_2 ($\beta \propto -2.5E_g/h\nu$ but $n_2 \propto -10E_g/h\nu$), which is why the nonlinear figure of merit (F) becomes larger with increasing band gap energy, as noted in Table 3.3. While it cannot be assumed that the linear correlation between β and $E_g/h\nu$ extends to $Ge_{23}Sb_7S_{70}$ (because $\beta < 0$ would be predicted), this still suggests that this glass is probably most well

`

suited for near-IR nonlinear optical applications, where a $F < 1$ (high non-linearity with low nonlinear absorption) are desired.

While these correlations may be oversimplifications of the true mechanisms controlling structure-property relationships in these glasses, they nonetheless provide a first order means for estimating material behavior and thus can be seen as a powerful predictive tool. Moreover, it is instructive to see that it is possible to tailor the properties of these materials to a large degree, given simple a-posteriori knowledge of the structural role of the various constituents forming the glass network.

3.5 Summary of findings

In this chapter, an examination of the evolution of the physical, thermal and optical properties of the bulk glasses, and the relationship between properties and structure has shown:

1) As-based glasses possess greater density with lower glass transition temperatures (T_g) and hardness. Reduced absorption band gaps lead to high linear and nonlinear refractive index but make them less desirable for nonlinear optical applications compared to the Ge-based composition.

2) Partial replacement of As by Ge causes increased T_g and hardness, decreased refractive index and increased (blue-shifted) bandgap, leading to lower nonlinearity but with an improved figure of merit (F).

3) Partial replacement of As by Sb causes increased density and decreased T_g and hardness. The band is smaller (red-shifted), giving a high linear and nonlinear index but with a low figure of merit.

4) It was shown that both the linear and nonlinear optical properties varied primarily as a function of the lone electron pair density, while the thermal and physical properties varied as a function of the molar bond energy of the glasses.

CHAPTER FOUR

Solution Processing of Chalcogenide Films

It is well known that chalcogenide thin films obtained using thermal evaporation show a variety of inhomogeneities, most typically compositional drift or lamination, which are caused by differential volatility of the glass constituents, leading to possible preferential condensation. Various techniques may used to overcome this issue, including simultaneous multi-source evaporations [134], and alternate deposition routes such as sputtering [68, 135] or pulsed laser deposition [136]. While it is true that these techniques have to potential to increase compositional accuracy and homogeneity over standard thermal evaporation, it comes with added complexity and cost or reduced deposition rates and greater sensitivity to impurities. The prospect of using solution-based methods offers the opportunity to tightly control film chemistry through control of the solution chemistry. Additionally, high speed continuous processing methods and a variety of novel fabrication techniques become available through the use of solution processing, making this method highly advantageous compared to traditional processing routes.

The first step in developing solution-based processing methods is to understand the chemical stability of the glasses, and what solvents may be suitable for forming solutions, and eventually coatings. Attempts at depositing films through sol-gel based routes similar to those used for oxide coatings have previously been attempted [81-83]; however, have met with limited success in the preparation of chalcogenide materials due to the need to avoid oxygen incorporation into the film; oxygen is is a necessary part of

the hydrolytic reactions commonly used in sol-gel preparations. For this reason we chose to examine an alternate bulk glass dissolution route. Development of the process was broken into three parts: 1) optimization of the dissolution process for compositional fidelity, 2) optimization of the coating condition (spin-coating) for films with the lowest possible roughness, the largest thickness, and uniformity of thickness and 3) optimization of the post-deposition heat treatment procedure for films to produce properties as close as possible to those of the parent bulk glass.

4.1 Bulk glass dissolution

The first step of this development was the analysis of the chemical stability of the glass, with the goal of finding a solution where the glass may be dissolved, or colloidal sulfide particles suspended, without significant oxide formation. For this purpose we first examined $As_{42}S_{58}$ and $Ge_{23}Sb_7S_{70}$ bulk glasses which serve at examples of predominantly two-dimensional (2D) (AsS_3) and 3D (GeS_4) network, respectively. Additionally these glasses were selected as they might be expected to show different dissolution behavior. In order to determine the dissolution rate, a series of samples (1 x 5 x 5 mm) were prepared in order to present similar masses and surface areas. These samples were then suspended in 40 mL solutions of solvent and stirred vigorously (using magnetic stirrer at 800 rpm). The weights and dimensions of the samples were then measured at intervals 3 minutes. The dissolution rate was normalized to the molecular mass of the samples (based on structural units) as discussed in the previous chapter and to the surface area of the sample,

since it is presumed that this is a controlling factor in the dissolution. From the mass change of the sample, the average dissolution rate for each 3 minute period was calculated using the following formula:

$$W = \frac{\Delta m}{SM\Delta t} \qquad (4.1)$$

where W is the dissolution rate, given in (mol/cm^{2}s), Δm is the change in mass, M is the molar mass, and S is the surface area of sample and Δt is the elapsed time. The dissolution rate of the two base glasses in solutions of various pH is presented in Table 4.1 below. As an initial test, the glass was exposed to various aqueous solutions

Table 4.1: Dissolution rates of bulk glasses in various aqueous solutions, concentrations are given in W/V%, and approximate pH values were calculated

Solution	**Dissolution rate ±10 (x10^{-9} mol/cm^{2}s)**	
	$As_{42}S_{58}$	$Ge_{23}Sb_7S_{70}$
98% H_2SO_4 + 0.1M Cr_2O_3	164	112
98% H_2SO_4	19	7
86% HNO_3	27	18
37% HCl (pH ~ -1.1)	0	0
0.5M H_2SO_4 (pH ~ 0.3)	0	0
pH = 4 buffer	3	0
D.I. water (pH =7)	0	2
pH = 10 buffer	5	160
29% NH_4OH (pH ~ 12.1)	177	760
50% KOH (pH ~ 13.7)	1573	5331

It is interesting to point out that the glasses are both stable in neutral and acidic (non-oxidizing) solutions, but begin to dissolve quite rapidly in basic solutions. Although highly resistant to HCl solutions, persisting for several days without significant surface attack, the surface of the glass is slowly dissolved when placed in concentrated nitric or

sulfuric acid. In fact, was found to become smoother and more highly polished. This effect was attributed to surface oxidation of the glass and subsequent dissolution of the oxide layer by the acidic medium, due to the oxidizing nature of concentrated HNO_3 and H_2SO_4. It can be also noted that it is enhanced dramatically when chromic oxide, an oxidizing agent, is added to the sulfuric acid. $Ge_{23}Sb_7S_{70}$, having a large excess of electronegative S atoms, was found to be slightly more resistant to this oxidation process, but still dissolved readily. It was also found that improvement of surface roughness of several hundred nanometers (RMS) was possible given long exposures (several days) and while not of interest in this study, this process has the potential for use in chemical polishing of ChG surfaces. In contrast, the surface of the glasses exposed to basic solutions became pitted and degraded rapidly. AFM scans of the glass surfaces following etching in 0.02M KOH are shown in the figure below.

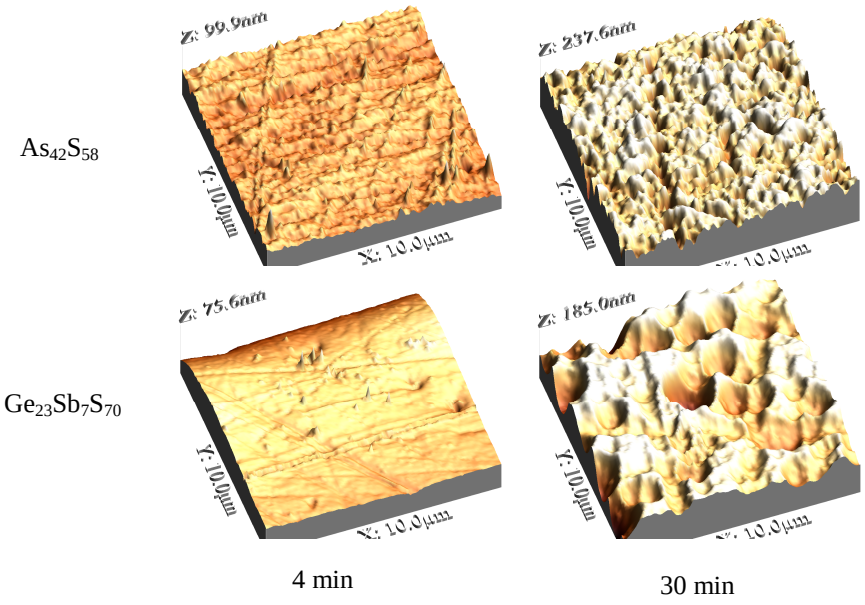

Figure 4.1: AFM Surface profiles (10 µm x 10 µm) of glasses etched in aqueous solutions [137].

After 4 minutes of etching it can be seen that small surface defects left after polishing become visible for both compositions. After 30 minutes of etching, the surface of $As_{42}S_{58}$ is significantly roughened while that of $Ge_{23}Sb_7S_{70}$ shows pitting. EDS analysis of the surface of the etched samples is summarized in the following table.

`

KOH Concentration	Surface composition (± 2 at.%)						
	$As_{42}S_{68}$			$Ge_{23}Sb_7S_{70}$			
(moles/L)	**As**	**S**	**O**	**Ge**	**Sb**	**S**	**O**
0.01	40	60		21	6	73	
1	36	51	13	21	7	42	30
2	33	44	22	20	7	44	29
4.5	31	44	24	20	7	22	51

Table 4.2: Surface composition of $As_{42}S_{58}$ and $Ge_{23}Sb_7S_{70}$ after etching in KOH solutions of various concentrations for 4 minutes [137].

The dissolution rate is calculated from the change in sample mass versus the time exposed to the solution (slope), and corrected for the surface area of the sample and molar weight of the composition.

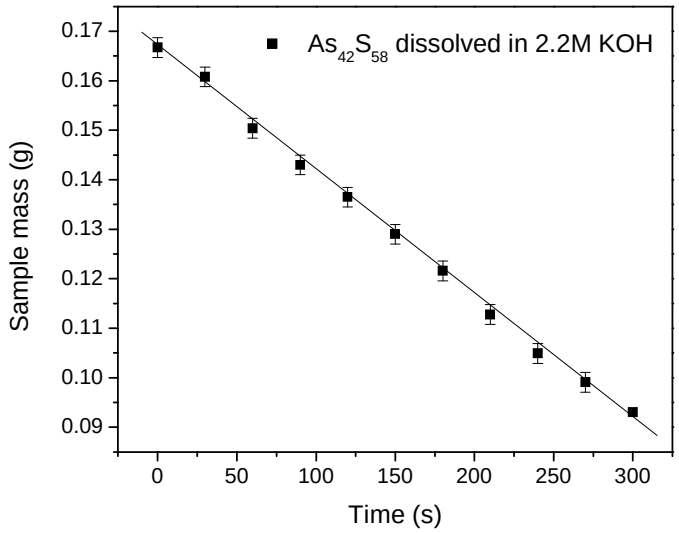

Figure 4.2: Variation of $As_{42}S_{58}$ sample mass with exposure time in 2.2M KOH solution.

It can be seen that the variation in sample mass is linear, indicating a constant dissolution rate during the exposure. By plotting the logarithm of dissolution rate against the

`

logarithm of the concentration, the slope gives the value of n, the reaction order in the rate equation, while the intercept gives an idea of the relative reaction rates.

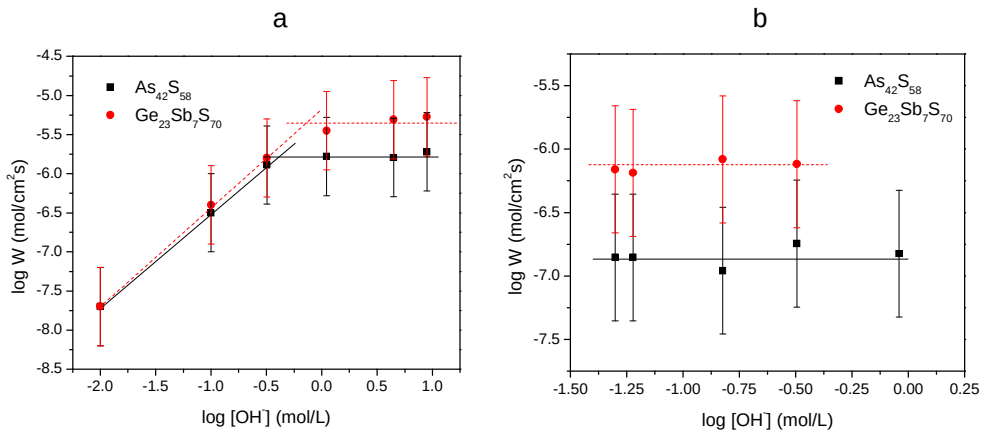

Figure 4.3: log-log plot of dissolution rate versus OH^- concentration in KOH (a) and NH_4OH aqueous solutions [137].

One can see from the graph, that when dissolved in increasing KOH concentrations (<0.3 M), the dissolution rate of both glasses also increases, and the slope was found to be approximately 1, indicating a 1:1 ratio of glass molecular units to OH^- ions in the reaction. This tells us that one OH^- ion is needed to cleave one bond at the surface of the glass. At the high concentrations, (>1 M) the dissolution rate is constant and slope approaches 0, indicating that there is no longer a dependence of the dissolution rate on OH^- concentration. The point at which the reaction mechanism changes appears to be near 0.5M, and is perhaps slightly lower (0.4 M) for $As_{42}S_{58}$ than for $Ge_{23}Sb_7S_{70}$ (0.6 M). In the case of dissolution of the bulk glasses in ammonia solutions, the dissolution rate was not observed to change with variation in concentration, and the rates were found to be lower than the maximum rate in KOH. The dissolution rate for $Ge_{23}Sb_7S_{70}$ in ammonia

is approximately unchanged at ~10^{-6} mol/cm^2s, while that of $As_{42}S_{58}$ is significantly higher, increasing from 10^6 in KOH to 10^7 in ammonia.

The observation of oxides formed on the surface of the glass when dissolved in hydroxide solutions (see Table 4.2) indicates that these solutions are unsuitable for film deposition. It was therefore necessary to find an organic liquid having a basic character to serve as a solvent. The logical choice in this case is primary or secondary amines. Critical properties of three such amines, chosen for this study, are reported form their MSDS sheets in the table below.

Table 4.3: Summary of amine solvent properties

Solvent	**Propylamine**	**Ethylenediamine**	**Ethanolamine**
	H_2N-CH_2-CH_2-CH_3	H_2N-CH_2-CH_2-NH_2	H_2N-CH_2-CH_2-OH
M.W. (g/mol)	59.11	60.103	61.08
Density (g/cm^3)	0.719	0.899	1.012
Boiling Point (°C)	48	116	170
Basicity (pK_b)	3.4	4.1	4.5
Viscosity (cP)	0.359	1.54	19.4

As shown in the table, the only change in the molecular structure is the nature of the terminal group which is CH_3 NH_2 or OH, however this influences many important properties which, as will be shown throughout the remainder of this work, alters their dissolution kinetics, solubility limits, and film processing ability. Figure 4.4, below, shows the reaction order for the four investigated glass in three primary amines, propylamine, ethylenediamine, and ethanolamine.

`

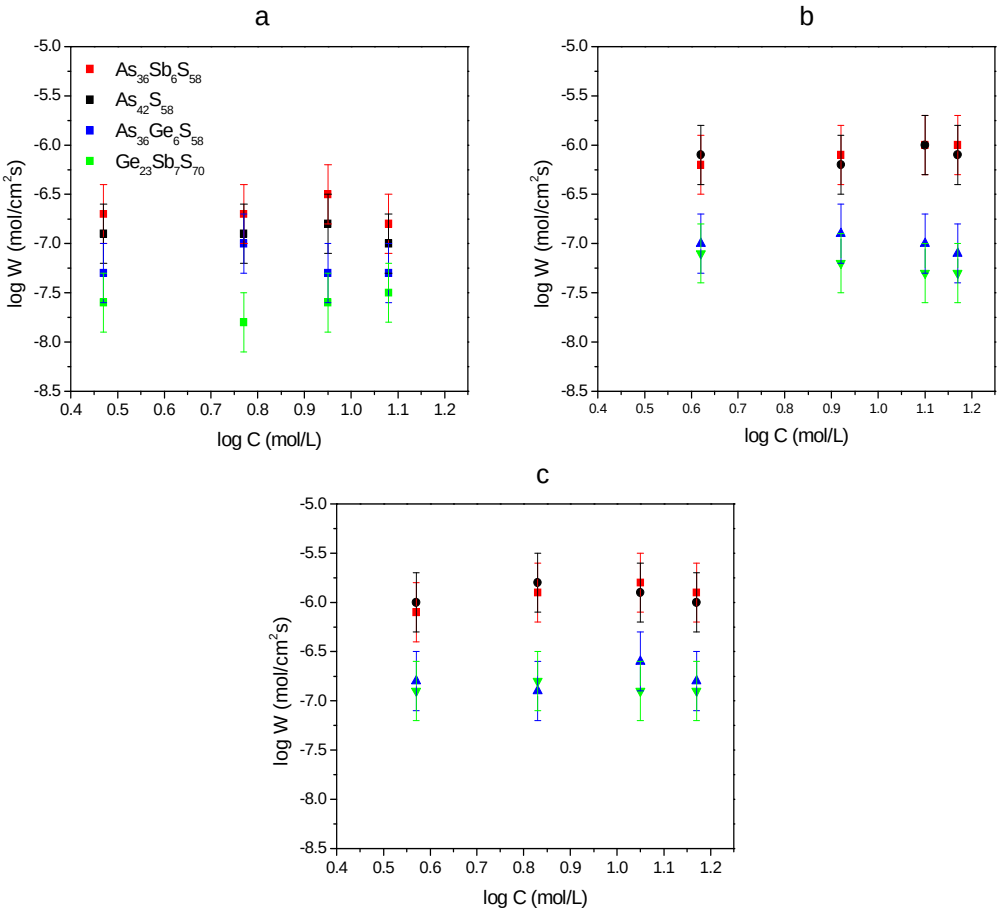

Figure 4.4: Reaction order for amine solvents: propylamine (a), ethylenediamine (b) and ethanolamine (c).

In all cases for the four chalcogenide glasses studied, an order of reaction of zero is found, as was observed for NH_4OH dissolution. However, a very different trend is observed for organic amines, as compared to KOH and ammonia dissolution in terms of relative dissolution rates. The most rapidly attacked glasses are the As-based glasses, and the replacement of As by Sb has very little effect (a slight increase of rate only in propylamine), while replacement of As by Ge decreases the dissolution rate. $Ge_{23}Sb_7S_{70}$ has a much reduced dissolution rate as compared to the As-based compositions. When comparing the same glass across the different solvent, ethanolamine is found to have the

highest dissolution rate followed by ethylenediamine and propylamine. The dissolution rates and trends observed in this study are similar to those reported by previous authors [138-141] for other chalcogenide glass systems .

It is important to note some additional observations made during amine dissolution. Firstly, roughening of the surface occurred during amine dissolution, leading to a deepening of scratches and eventual pitting, similar to the response shown in the case of OH^- dissolution. Secondly, most solutions were found to exhibit instability at high glass loadings (mass of glass per unit volume of solvent). This does not limit the potential for scale-up of the process, as the solubility limit does not vary with total volume. $Ge_{23}Sb_7S_{70}$ formed a red-brown precipitate unless only small quantities of glass (<50 mg/mL) were used. These precipitates were shown, using EDS, to contain Sb, while $As_{36}Ge_6S_{58}$ gave white precipitates containing Ge. $As_{36}Sb_6S_{58}$ solutions above 0.5 g/ml in propylamine separated into two immiscible layers with the upper yellow layer containing As and the lower dark orange layer containing Sb. Very high glass loading contents for $As_{42}S_{58}$ (up to 1 g/mL) were dissolved in ethanolamine (ETA) and ethylendiamine (EDA), giving very high viscosity solutions, a helpful trait if thicker films from these solutions are desired. No significant changes in glass surface composition were observed for non-aqueous etching, however, indicating that amines are promising solvents for solution processing, given low loadings for glasses containing Ge or Sb. Finally, absolutely no dissolution was observed for non-protic amines, such as triethylamine, indicating that the presence of an N-H bond is critical to the dissolution mechanism. It should also be noted that these dissolutions were performed in dry solvent (dried over

molecular sieves), and under N_2 atmosphere. It was determined that neglecting either of these conditions leads to the formation of oxide precipitates.

In comparison to aqueous solutions, the dissolution of As-based glasses in all three amines provided bright yellow or orange solution (depending on concentration), while surprisingly the dissolution of $Ge_{23}Sb_7S_{70}$ in all three solvents resulted in green solutions (though the glass is orange-yellow in color). This is particularly evident in ethylenediamine solution which is blue at very low loading concentrations and a bright emerald green at higher loading concentrations. Furthermore, the color of all amine solutions of this glass reverted to yellow and formed a precipitate if the solution was left open to the air for several hours. The same color was produced if only elemental S was dissolved in EDA, suggesting that it is the excess S in this glass which produces the coloration. The UV-Vis absorbance spectrum of a 0.1 g/mL solution of $Ge_{23}Sb_7S_{70}$ in ethanolamine, which was prepared under dry N_2 atmosphere and measured in a 10 mm path length quartz cuvette which was sealed with a Teflon stopper. The pure solvent in a matched cuvette was used as a reference for the background.

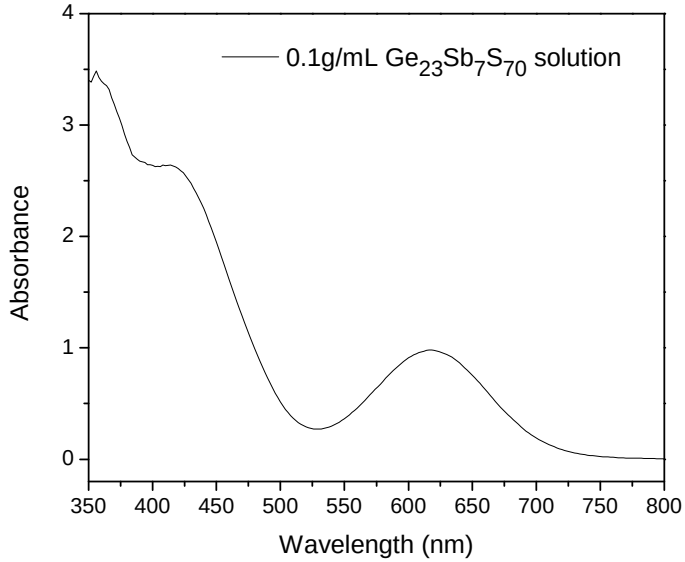

Figure 4.5: UV-Vis absorption spectrum of 0.1g/ml $Ge_{23}Sb_7S_{70}$ in Ethanolamine

Two main absorption features are found near 410 and 620 nm which are not present in the spectrum of the $Ge_{23}Sb_7S_{70}$ bulk glass, which are related to presence of excess S in this composition. The plot of absorbance at 620 and 410 nm versus glass loading for the three amine solvents is shown in figure 4.6.

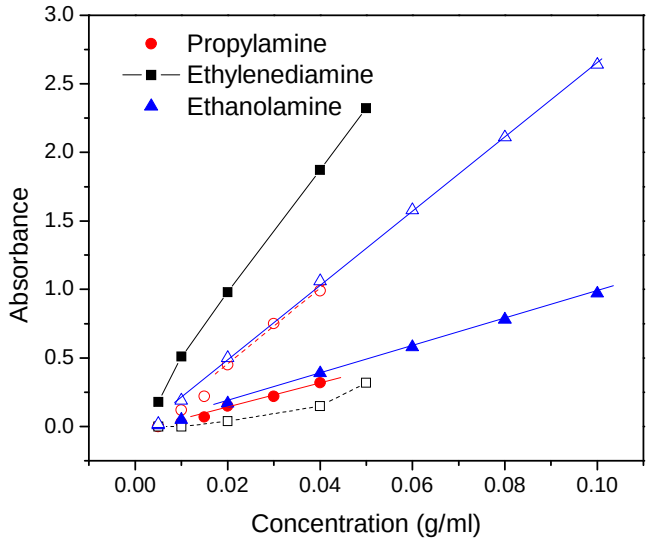

Figure 4.6: UV-Vis absorbance of $Ge_{23}Sb_7S_{70}$ solutions in EDA, ETA and PA at 620nm (closed symbols) and 410 nm (open symbols).

From the figure, it can be seen that the absorption coefficients of the two solvents with only one amine group (propylamine and ethanolamine) are very similar up to 0.04g/ml loading levels, above which precipitates form in propylamine solutions. However, the spectra of solutions prepared from ethylenediamine are significantly different, and the absorption of the 620 nm peak is significantly larger than that at 410 nm. This suggests that two bands are related to different products, and that one is more favored in ethylenediamine solutions. Previous investigations of elemental S dissolved in amine solutions have identified the species as the S_3^- (410 nm) and *cis*-planar S_4^- (620 nm) radicals using UV-Vis and Raman spectroscopy [142, 143] and electron spin resonance measurements [144]. Observations of S in the gas phase [145] and of solid S formed by rapid quenching [146] attribute the 410 and 620 nm absorptions to S_3 and *cis*-S_4

respectively, which has also been corroborated using quantum-chemical calculations [147].

The viscosity of the solutions was measured using a Brookfield Engineering (model DV-III Ultra) Viscometer, with a varying shear rate from 0.8 to 8 s^{-1}. This range was chosen to correspond with the spin-coating experiments which will be reported later in this work. Spin coating was performed using 5 cm polished square glass substrates at spin speeds of 1000 to 9000 rpm, with target film thicknesses of 500-1000nm. As shear rate (τ) is given by

$$\tau = \frac{V}{h} \qquad (4.2)$$

where h is the film thickness and V is the linear velocity at the film's edge, which is the product of spin rate (ω) and substrate radius (r). The highest glass loading and viscosity was achieved for ethanolamine solutions of $As_{42}S_{58}$, in which 1g of glass per ml of solvent was found to soluble, though this was only achievable by heating the solution to a temperature of 100°C in a sealed vial using a water bath. If this solution was allowed to cool to room temperature, a dark orange (but transparent) solid was formed which did flow appreciably over several days. Such a viscosity was too high to be measured. Similar concentrations (1g/ml) were also possible in the $As_{42}S_{48}$/EDA which did give clear solutions with measurable viscosities. The room temperature stress-strain curves for solutions of $As_{42}S_{58}$ in EDA and with varying glass content are shown in figure 4.7.

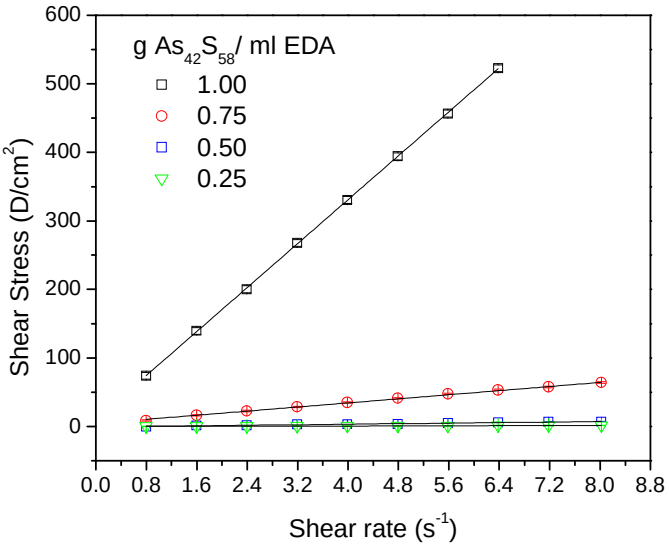

Figure 4.7: Stress-strain curves for EDA-$As_{42}S_{58}$ solutions at various glass loadings.

The viscosity of all the examined glass solutions was found to be linear across the measured range. This indicates that the viscous behavior is approximately Newtonian, where the shear stress is linearly dependant on the shear rate, and viscosity is given by the slope. This finding was observed for all glass solutions in EDA and ETA. It should be noted, however, that the viscosity of propylamine (PA) solutions was too low to be measured by this instrument (<5 cP), within the solubility range for this solvent (<0.05g/mL). Moreover, the relatively low solubility of $Ge_{23}Sb_7S_{70}$ (~0.1g/ml in EDA and ETA) also presents challenges for viscosity measurement. The viscosities of all $Ge_{23}Sb_7S_{70}$/EDA solutions were all too low to be measured, and no trends were observed for ETA solutions due to low glass content. Therefore, the viscosities for the EDA and ETA solutions of $As_{42}S_{58}$ only are shown as a function of glass loading in Figure 4.8.

`

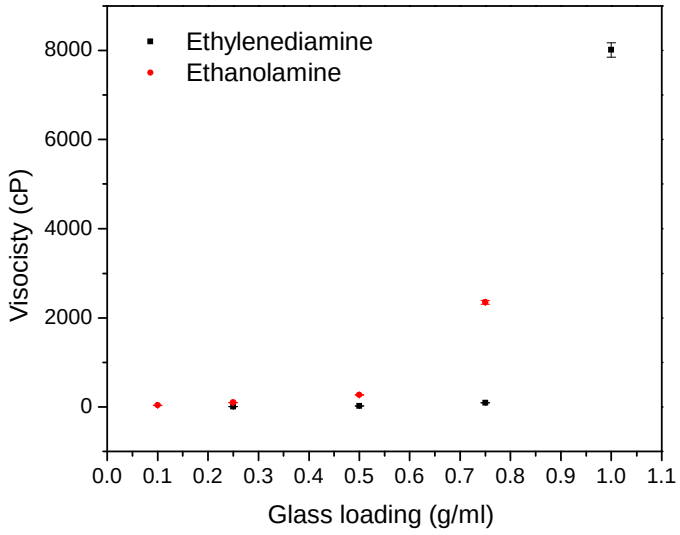

Figure 4.8: Viscosity (linear regression slope) of EDA and ETA solution of $As_{42}S_{58}$ as a function of glass loading.

It is important to note that a 1g/ml solution represents approximately 30% solids by volume. This is similar to common ceramic slurries, which tend to show highly non-Newtonian viscosities due to particle-particle interactions [148].

The micro-Raman spectrum of a solution of $Ge_{23}Sb_7S_{70}$ dissolved in ethanolamine (0.1 g/mL) is shown in Figure 4.9 below. It should be noted that, due to high volatility of ethylenediamine and propylamine, only ethanolamine solutions were found to be suitable for Raman spectroscopy measurements.

`

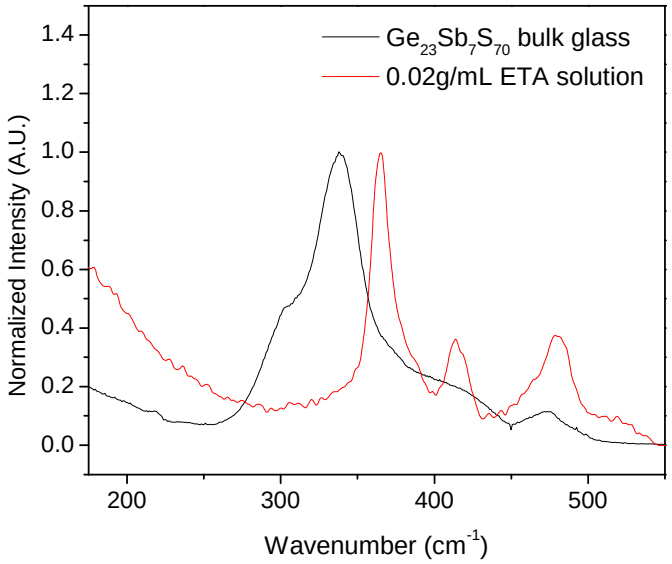

Figure 4.9: Raman spectrum of 0.1g/ml $G_{23}Sb_7S_{70}$ dissolved in ethanolamine

One can see from the figure that the Raman spectrum of the solution is different from that of the parent bulk glass, indicating that significant changes in structure have occurred during dissolution. The main band, expected to correspond to the stretching vibrations of GeS_4 tetrahedral units shifts from 330 cm^{-1} to approximately 360 cm^{-1} and gains a shoulder near 380 cm^{-1}. The shoulder of the band in the bulk glass, near 300 cm^{-1}, corresponding to the stretching of $SbS_{3/2}$ pyramids has disappeared completely in the spectrum of the dissolved glass, and new bands appear near 415 cm^{-1} as well as an asymmetric feature near 480cm^{-1}, which has a shoulder near 510 cm^{-1}. Assignment of this highest wavenumber feature is the most straightforward, because two bands at 480 and 510 cm^{-1} are present in the spectrum of the pure solvent (ETA). An additional small band (420 cm^{-1}) is also present in the spectrum of the solution which has been attributed to the S_3^- ion, already identified from the UV-Vis absorption spectrum.

`

In order to analyze the large shift of the main band, it is instructive to note that it was impossible to dissolve a significant quantity of crystalline powders, of either GeS_2 or Sb_2S_3 (meant to serve as a source for reference spectra), in any amine based solvent examined to date. However, both compounds were found to be readily soluble in solutions in which elemental S was already dissolved. This seems to suggest that the excess S in this glass composition may play a significant role in the dissolution process.

Several studies have examined the reaction between GeS_2 and Sb_2S_3 in amine-based solutions containing excess S [149-154]. It has previously been shown that the product which is typically formed during GeS_2 dissolution process is the "adamantane-like" $[Ge_4S_{10}]^{4-}$ cluster [150] which is composed of 4, corner-shared GeS_4 tetrahedra. This structure exhibits two main Raman features including a large peak near 360 cm^{-1} corresponding to Ge-S-Ge bond vibrations within thiogermanate $[Ge_4S_{10}]^{4-}$ clusters, and a smaller asymmetric feature near 415 cm^{-1} which may be attributed the motion of terminal Ge-S bonds at the corners of the Ge_4S_{10} structure. Both of these features are clearly present in the spectrum of the dissolved glass solution.

While the band near 300 cm^{-1}, related to SbS_3 pyramids, is completely missing from the Raman spectrum of the solution, EDS has consistently shown that the Sb content of the films derived from these solutions is the same as that of the parent bulk glass, within the experimental error (± 2at%) indicating that Sb is still present in the solution but not as SbS_3 units. Tetrahedral antimony sulfide species have previously been observed in amine solutions either as SbS_4^{3-} ions [152, 155] or clusters [153] such as $Sb_2S_6^{2-}$. These units, containing SbS_4 tetrahedra, possess Raman bands near 370 and 380

cm^{-1} which appear to form the shoulder of the main band in the spectrum of the solution. We may therefore tentatively conclude that during the dissolution of this glass, excess S forms polysulfide radicals which react with GeS_4 and SbS_3 units within the glass network to produce $Ge_4S_{10}^{2-}$ and SbS_4^{3-} tetrahedral molecules, depicted in Figure 4.10, below.

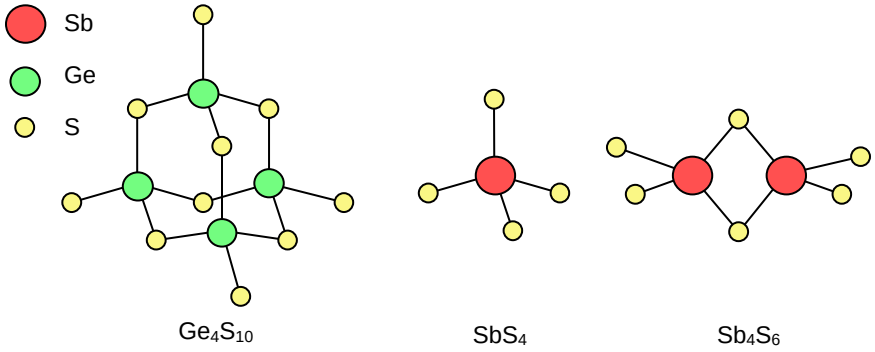

Figure 4.10: Proposed dissolution products for $Ge_{23}Sb_7S_{70}$

The presence of these molecular ions in the solution might be confirmed using mass spectroscopy, but such measurements have not been possible to date. Several studies have also shown the strong tendency of compounds containing Ge_4S_{10} to crystallize [149, 154] when prepared in aqueous solutions, by linking of the unshared sulfur atoms at the corners of the structure.

The Raman spectrum of the 0.1g/ml solution of $As_{42}S_{58}$ dissolved in ethanolamine is presented in figure 4.11 below.

`

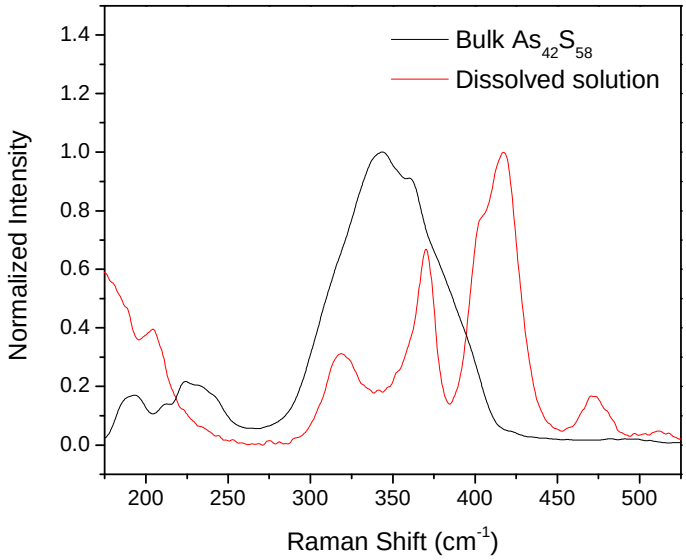

Figure 4.11: Raman spectrum of 0.1g/ml $As_{42}S_{58}$ dissolved in ethanolamine

In the spectrum of the solution, we find two features near 475 and 510 cm^{-1}, which can be attributed to the solvent. We also see that the main band is now located near 430 cm^{-1}, with a shoulder near 410 cm^{-1} Some smaller bands are found within the range covered by the main band of the bulk glass, including features near 320 and 370 cm^{-1}, and an additional small band near 210 cm^{-1} is also observed. The dissolution of a similar glass composition was studied previously [156]. In accordance with this prior work, the bands near 370 and 210 cm^{-1} may be attributed to the presence of As_4S_4 molecules similar to those observed in the spectrum of the bulk glass. Additionally, the feature near 320 cm^{-1} may be deconvolved into two bands at 320 and 340 cm^{-1}, associated with As-S bond vibration within AsS_3 pyramids [119]. Finally is possible to attribute the large new band at 430 cm^{-1} either to As-N bonds or to terminal (unshared) As-S bonds [156].

`

In agreement with a previous study [156], reaction of the amine with As_2S_3 occurs by attack of the lone pair the nitrogen atom in the amine, leading to cleavage of As-S bonds in order to form As-N bonds (aminolysis). One study of the dissolution of $As_{33}S_{67}$ in butylamine using dynamic light scattering, showed the formation of nano-colloids dispersed in the solvent with radii of up to 4 nm, however this seems to be at variance with the Raman data. At bulk density ($3.2g/cm^3$), a sphere of 4 nm radius should contain ~1000 atoms, or have a radius of ~22 atoms Since the ratio of atoms at the surface to the number of atoms in the volume of a sphere is given by.

$$\frac{n_s}{n_v} = \frac{r^3 - (r-1)^3}{(r-1)^3} \qquad (4.3)$$

where n_s is the number of surface atoms, n_v is the number of atoms below the surface and r is the radius of the sphere (in atoms) [157]. Accordingly, over 80% of the atoms are expected to be found beneath the surface than at the surface of a 4 nm As_2S_3 particle, however no bulk modes are visible in the Raman spectrum. The observation of Newtonian fluid dynamics in glass solutions also brings the idea of colloidal dispersions into question, as such fluids generally display more complex behavior, while the viscosity of true solutions tends to remain Newtonian at high concentrations [148].

This suggests that dissolution results in the formation of variety of fragments of the glass network with various small sizes, which become dissolved into the solvent. A selection of such possible network fragments are illustrated in Figure 4.12 below.

`

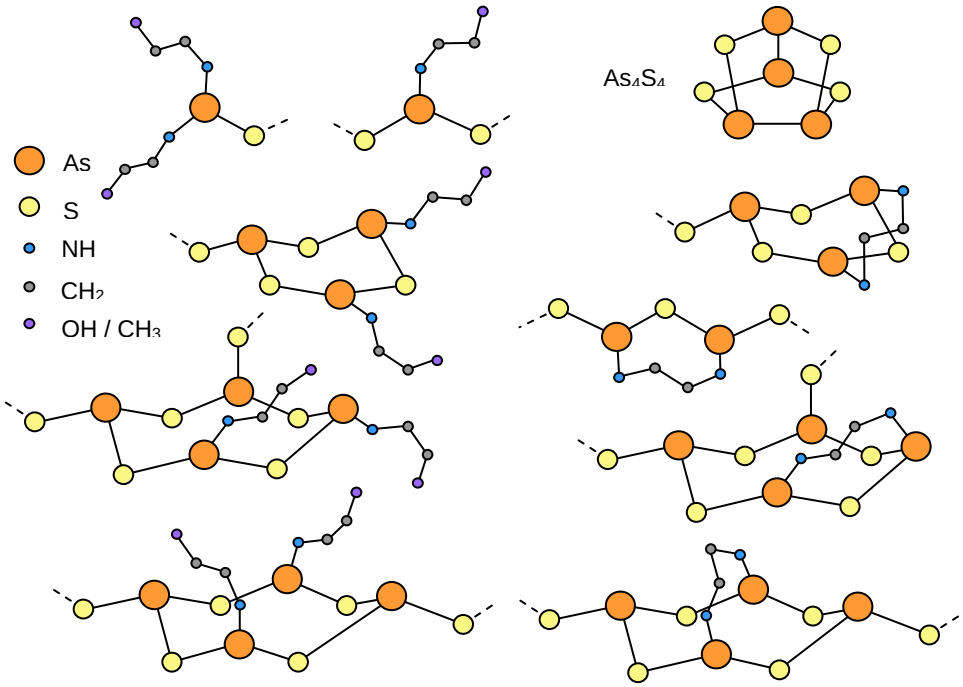

Figure 4.12: Proposed dissolution products for $As_{42}S_{58}$

This is consistent with a previous study for As_2S_3 bulk glass in EDA solution [158], where it was presumed that the terminal sulfur atoms of these fragments then bridge together through the formation of disulfide bonds to form an extended structure, resulting in the strong Raman band located near 430 cm^{-1}. The observed ability of this glass to form gels of very high viscosity was attributed to the formation of these As-S-S-As linkages between these network fragments. The observation of gelation at high glass concentrations in the current study is also in accordance with previous observations of ethylenediamine solutions of As_4S_4 [159] and As_2S_3 [156], which reported similar molecular structures to those shown in figure 4.12 forming –As:NH_2-CH_2-CH_2-NH_2:As- chains with nitrogen atoms of EDA acting as a ligand for As.

`

Based on this interpretation of the dissolution products, it is possible to understand the observations of the evolution of dissolution rates with composition, and the precipitation of solutions containing Sb or Ge. The discussion primarily centers on general acid-base chemistry. Amines are generally considered to be bases. The Brönstead-Lowry (B-L) concept defines an acid as a substance which is able to donate a proton while a base is a proton acceptor; whereas the Lewis concept defines acids as capable of accepting a lone pair in order to form a coordinate covalent bond and bases are the lone pair donors. In aqueous solutions these two systems are equivalent, but in non-aqueous solutions and particularly when the acid (in this case the glass) does not possess hydrogen atoms, the B-L concept becomes awkward. Because the relative strengths of acids are generally normalized to water (using the B-L system), their relative strengths are defined by the relative equilibrium concentrations of the acid and its dissociated proton:

$$K_a = \frac{[H+]\cdot[A-]}{[HA]} \qquad (4.2)$$

[HA] is the concentration an acid associated with its proton, $[H^+]$ is the concentration of free protons and the $[A^-]$ is the concentration of the conjugate base. The value K_a is known as the acid dissociation constant and is a direct evaluation of the ability of the acid to donate its proton. A similar term K_b is used in reference to the ability of a base to accept a proton. In practice, it is more convenient to refer to these values on a logarithmic scale because they tend to vary over many orders of magnitude. Therefore, pK_a and pK_b

`

are the negatives of the logarithm of K_a and K_b respectively. Importantly, the free energy of reaction (ΔG) for a particular acid to dissociate from its proton is given by:

$$\Delta G = RT\left(pK_a\right) \tag{4.4}$$

This means that acids or bases with large positive values of pK_a or pK_b respectively are considered weak, because the dissociation reaction is not spontaneous. As explained, this system is not the preferred way to envisage the reaction of amine and glass. It is the ability of the amine to donate its electron pair which actually defines its basicity, but the relative values of pK_b does not change based on the concept used and are a valid tool for comparison here. During the reaction of an acid (glass) and base (amine), the reactant base will be consumed and a new base will be produced. The free energy of this reaction is given by:

$$\Delta G = RT\left(pK_{b1} - pK_{b2}\right) \tag{4.5}$$

Thus, if the product is a weaker base than the reactant ($pK_{b2} > pK_{b1}$) the reaction will be spontaneous, providing driving force behind most acid-base reactions.

There is an additional distinction which is important in this discussion, called nucleophilicity, which is distinct from basicity. This is the focus of the Pearson hard-soft acid base (HSAB) concept [160], which defines the chemical hardness (η) as equal to one half of the derivative of the chemical potential of a system with respect to the total number of electrons. Stated more simply, it relates to the difference between the ionization potential (electron-loss energy) and electron affinity (electron-gain energy) [161] and is given by:

`

$$\eta = \frac{1}{2}\left(\frac{\partial \mu}{\partial N}\right) = \frac{1}{2}\left(E_I - E_A\right) \qquad (4.6)$$

where N is the total number of electrons in the system, μ is the chemical potential, E_I is the ionization potential and E_A is the electron affinity. Hardness is therefore a measure of the energy needed to alter the electron cloud through addition or removal of an electron. Species with extreme (very high or low) electronegativites or high charge densities would be considered hard, while those with intermediate electronegativities and high polarizabilities would be considered soft. Furthermore, hard-hard interactions will tend to be ionic in nature while soft-soft interactions are covalent, making soft bases generally better nucleophiles [162]. There is no direct correlation between basicity and nucleophilicity, however. For instance, the iodide (I^-) ion is among the strongest nucleophiles due to its large size and polarizabiliy, but is an extremely weak base (HI is a very strong acid). In comparison, the OH^- ion is a very strong base, but a poor nucleophile as it tends to be highly ionizing. It should be noted that attempts were made to dissolve the glasses in KI solutions, and no reaction was observed, indicating the nucleophilicity is only a secondary concern in glass dissolution.

Interestingly, the term ($E_I - E_A$) used in Equation 4.5 is commonly referred to as the *Hubbard U* [163] and is a measure of the band gap in Mott-type insulators. While the Hubbard term commonly considered to be an oversimplification of the true band gap due to charge transfer and electron-phonon coupling effects [164], it is useful as a qualitative tool for comparing the relative chemical hardness of the glasses through shifts of the band gap.

`

The reaction of the amine with the glass is expected to occur through nucleophilic attack of the N lone pair, which may occur either at metal (As/Sb/Ge) centers or even at S atoms in S-S chains [142]. Moreover, as the order of reaction for dissolution is 1 at low concentration, this indicates that the mechanism is of the SN_1 type where the rate limiting step is the generation of an ion pair [165]. While the strength of the nucleophile (amine) is in part dependent on the chemical hardness, the reaction must also have a driving force. As noted above, dissolution occurs both in OH^- solutions and in amines (as long as an N-H bond is present) which are a relatively poor nucleophiles, but not at all in neutral solutions even when a very good nucleophile (such as I^-) is present. In general, there are three basic forms of organic amine: primary ($R\text{-}NH_2$), secondary ($R_2{=}NH$) and tertiary ($R_3{\equiv}N$), with R being some form of carbon chain. All of these are considered bases as defined by their ability to donate their electron lone pair; however, during the reaction of amines containing N-H bonds it is also possible to cleave a bond in the glass. For example, M-S-M where M is a metallic element would yield M-SH and N-M products. In the case of tertiary amines, the only possible products are $R_3N^+\text{-}M$ and $M\text{-}S^-$. Because the hydrogen of a thiol (-SH) group is acidic (pK_a = ~10), it may go on to donate its proton to additional amine molecules in the solution, thus making the driving force for the reaction the generation of an acid and its subsequent neutralization. The thiolate anion ($R\text{-}S^-$) in comparison, is a base with similar strength to the amines in this study (pK_b ~4), which means that the forward reaction is not spontaneous. Note that the pK_b of propylamine, ethanolamine and ethylenediamine are 3.4, 4.5 and 4.1 respectively. As the generation of two charged species within a relatively non-polar environment is not favored without

some other strong driving force, this explains why no dissolution was observed when tertiary amines are used as the solvent.

In comparing the amines to each other, their structure becomes important. While propylamine is the strongest base, the molecule is terminated with a methyl ($-CH_3$) group which is essentially inert, leading to low polarity (dielectric constant (ε) = 5.3 F/m). Ethanolamine is terminated with an OH group which, due to the high electronegativity of oxygen, withdraws some electron density from the amine group and decreases its basicity; however, it has a high polarity (ε = 37.7 F/m) which increases stabilization of the solute and is able to participate in hydrogen bonding, giving this solvent the useful property of high viscosity. Ethylenediamine is symmetrical and has an amine group at each end of the molecule which slightly decreases basicity (per amine group) and places its polarity between those of propylamine and ethanolamine (ε = 13.5 F/m). It is also able to participate somewhat hydrogen bonding, but more importantly, having two amine groups increases the chances that the molecule will collide with the glass surface in the proper configuration for an amine group to react with network units (kinetic effect), and it is able to function as bridge between solute molecules (solvation effect). For these reasons, it is not surprising the fact that dissolution rate follows solvent polarity rather than basicity when comparing the same glass across multiple solvents.

First, in examining the glasses, it is important to note that chalcogens (and chalcogenide ions) are among the softest species known [160], having both high polarizabilities and intermediate electronegativities, while OH^- and ammonia in aqueous

solutions are chemically hard and are highly ionizing [160]. Compared to As, Ge is moderately hard, due to its higher oxidation state and charge density, which is evidenced by the blue shifted band gap of the Ge-containing glasses. In contrast, Sb is larger and more polarizable than As, as seen by its tendency to red-shift the band gap. Looking at the trend of dissolution rate in aqueous solution (chemically hard environment) we see that that $Ge_{23}Sb_7S_{70}$ glass, which gives more ionic products on dissolution, has a higher dissolution rate, while $As_{42}S_{58}$ has a lower rate. $Ge_{23}Sb_7S_{70}$, having a large excess of oxidizing S atoms may be expected to be more resistant to oxidation in acidic solvents. These results are consistent with our discussion of the HSAB principal, discussed in section 4.1.

This suggests that when comparing the glasses to each other (as when comparing the solvents) it is the stabilization of the reaction products by the solvent which controls the dissolution rate. In the amine solvents (softer chemical environment), we may therefore expect the opposite trend than in aqueous environments, which is in fact what is observed. The dissolution of the $As_{42}S_{58}$ and $As_{36}Sb_6S_{58}$ gives covalently-bonded species which are more easily stabilized by the solvent, while $As_{36}Ge_6S_{58}$ and $Ge_{23}Sb_6S_{58}$ give ionic species which tend to precipitate. The excess of S in $Ge_{23}Sb_6S_{58}$ induces oxidation of Sb products by the highly reactive polysulfide radicals, converting chemically soft pyramidal Sb^{3+} to harder tetrahedral Sb^{5+} containing units which has a higher charge density, changing the behavior of Sb in the solution. We may therefore suggest that glasses which are slightly deficient in S may be more stable in amine-based solutions by preventing this type of S oxidation. Finally, because the molecular structure of the

dissolution products for As-based glasses is more similar to the units in the bulk glass, we can suggest that solution derived films from these glasses may also have structures more similar to those of the parent bulk glasses.

4.2 Optimization of dissolution conditions

In order to deposit films with the greatest possible thickness, it is preferable to achieve the high loadings of glass in the solution to realize a high viscosity solution and minimize thinning through solvent evaporation. However, as noted above, many of these glasses give precipitates at high glass loadings. Therefore, the solution can be said to be optimal when it has the highest glass content while also being able to produce films of the same composition as the bulk glass. In order to create a method for determining the solubility limit for a particular glass-solvent combination, solutions of $As_{42}S_{58}$ and $Ge_{23}Sb_7S_{70}$ (being representative in Ge- and As-based glasses) in the primary amines already described were prepared containing various weights of finely powdered glass. The solutions were prepared using dry solvents under N_2 atmosphere using magnetic stirring, and the stirring time was varied. After stirring, the solutions were centrifuged to remove any remaining particulate matter (undissolved glass, precipitates, and/or impurities) then decanted. The compositions of the films prepared from these solutions were then determined using EDS. Films were prepared by spin-coating onto microscope slides at a spin speed of 1000 rpm, spinning for 5 seconds. A two-step heat treatment procedure was used, which included a 90°C heat treatment for 1 hour under dry N_2

`

atmosphere to stabilize the film, immediately followed by a 150°C heat treatment under vacuum (~0.1 Torr). By reducing the pressure, the boiling point of the solvent is reduced, allowing it to be removed more effectively; however, the presence large amounts of solvent in the film above its boiling point can lead to bubbles, cracking or pin-hole formation. The use of the two-step procedure allows sufficient slow evaporation of the solvent at low temperature to prevent this. The EDS composition of the films derived in this manner are shown as a function of glass loading in the Table 4.4 below.

Table 4.4: EDS composition of thin films (deposited at 1000 rpm) from PA, EDA and ETA solutions with varying glass loading (solutions which form precipitates are shown in **BOLD**).

		Film Composition				
		$As_{42}S_{58}$		**$Ge_{23}Sb_7S_{70}$**		
Solvent	**Glass loading (mg/ml)**	**As**	**S**	**Ge**	**Sb**	**S**
Propylamine	25	42	58	23	7	70
	50	42	58	25	5	70
	100	**40**	**60**	**29**	**0**	**71**
	200	**40**	**60**	**28**	**0**	**72**
	500	**40**	**60**	**28**	**0**	**72**
Ethylenediamine	25	42	58	23	7	70
	50	42	58	23	7	70
	100	42	58	23	7	70
	200	42	58	**28**	**1**	**71**
	500	42	58	**28**	**0**	**72**
Ethanolamine	25	42	58	23	7	70
	50	42	58	23	7	70
	100	42	58	23	7	70
	200	42	58	**27**	**4**	**69**
	500	42	58	**28**	**2**	**70**

In the table, solutions that produced a solution which contained undissolved solids or precipitate are shown in red. Solutions of $Ge_{23}Sb_7S_{70}$ are significantly more prone to precipitation, and those solutions which contain precipitates are found to produce films

with significantly reduced Sb content. Moreover, the composition of the films was found to approach $Ge_{28}S_{72}$ for high loading in all 3 solvents, which is the equivalent of removing Sb_2S_3 from the bulk glass. $As_{42}S_{58}$ was found to produce films approaching the stoichiometric composition of As_2S_3 in propylamine, but with no change in composition in the other two solvents. In order to determine the time needed to fully dissolve the glass powders, films were prepared using the maximum glass loadings which were found to give the same composition as the bulk glass. These results are summarized in Table 4.5.

Table 4.5: EDS composition of films obtained from PA, EDA and ETA using optimized glass loadings, as a function of stir time (solutions which form precipitates are shown in **BOLD**).

		Film Composition				
		$As_{42}S_{58}$		**$Ge_{23}Sb_7S_{70}$**		
Solvent	**Time (hrs)**	**As**	**S**	**Ge**	**Sb**	**S**
Propylamine	6	**40**	**60**	**28**	**0**	**72**
	12	42	58	**26**	**4**	**70**
	24	42	58	**25**	**5**	**70**
	48	42	48	23	7	70
Ethylenediamine	6	**41**	**59**	**25**	**3**	**72**
	12	42	58	23	7	70
	24	42	58	23	7	70
	48	42	58	23	7	70
Ethanolamine	6	42	58	23	7	70
	12	42	58	23	7	70
	24	42	58	23	7	70
	48	42	58	23	7	70

As can be seen, the dissolution of $As_{42}S_{58}$ is complete after a relatively short time, while the time needed to fully dissolve $Ge_{23}Sb_7S_{70}$ is significantly longer. Moreover the longest times are needed for propylamine and the shortest for ethanolamine. This is not surprising

based on our previous discussion of relative dissolution rates. It also may be noted that the composition of $Ge_{23}Sb_7S_{70}$ films formed from the shortest dissolution times and have a reduced Sb content, similar to that observed for solutions which exceed the solubility limit. This indicates that the species which are most stable in the solution are also dissolved first. The condensed list of optimized solutions is shown in table 4.6 below.

Table 4.6: Summary of optimized glass loadings and stir times for use in spin coating.

	$As_{42}S_{58}$		**$Ge_{23}Sb_7S_{70}$**	
Solvent	Loading (mg/mL)	Stir time (hr)	Loading (mg/mL)	Stir time (hr)
Propylamine	50	12	30	48
Ethylenediamine	100	12	100	12
Ethanolamine	100	6	100	6

While it is possible to prepare solutions of $As_{42}S_{58}$ with very high glass loadings (up to 1g/ml) the viscosity of these solutions is very high and are not suitable for spin coating. What is most important to note that by combining the optimized glass loadings and dissolution times it is possible to produced films, even for the $Ge_{23}Sb_7S_{70}$ composition which are identical in composition to the parent bulk glass, within experimental error (±2%). In our previous work it has not been possible to obtain films with this level of compositional fidelity using traditional thermal evaporation methods [19, 70, 131].

4.3 Optimization of spin coating conditions

As explained in the introduction, these coatings are intended for optical sensing applications where they will be used as waveguides. This makes optical loss one of the key concerns for their use. The main sources of optical loss are absorption and scattering. Absorption may be either intrinsic to the material or extrinsic if induced by impurities,

and scattering may be induced by inhomogeneities or surface roughness. Because we have found that surface roughness is the largest source of loss in planar waveguide-based devices [19], optimization of the deposition process has focused on the minimization of roughness. The optical design of the sensor system requires waveguides with 500-1000 nm thickness, therefore this thickness was chosen as the target for coating optimization. It is not possible to define a single optimal set of conditions, as these will vary based on the critical parameters of the specific optical design, and serves as an outline of the overall optimization method.

Films were prepared from the solutions listed in table 4.3 of the previous section, and the parameters to be optimized were: spin speed, spin time, wait times either before spinning (after application of solution) or after spinning (before heat treatment). In all cases, the amount of solvent applied to the substrate was sufficient to completely cover the substrate in a uniform layer of liquid before spinning began (~0.1ml/cm^2), and application was done drop-wise using a syringe fitted with a 0.2µm PTFE inline filter. All coating steps were performed inside a glove box which was continuously purged with dry N_2 (20 LPM introduced though a port on the coater) in order to protect the electronics of the spin coater from the corrosive solvent vapors, which additionally removes any buildup of solvent vapors in the atmosphere around the film.

Surface roughness was measured using a Zygo (NewView 6300) white-light interferometric microscope. Figure 4.13 below shows the surface roughness as a function of pre-spin wait time for propylamine-derived films spun at 1000 RPM for 10 seconds.

`

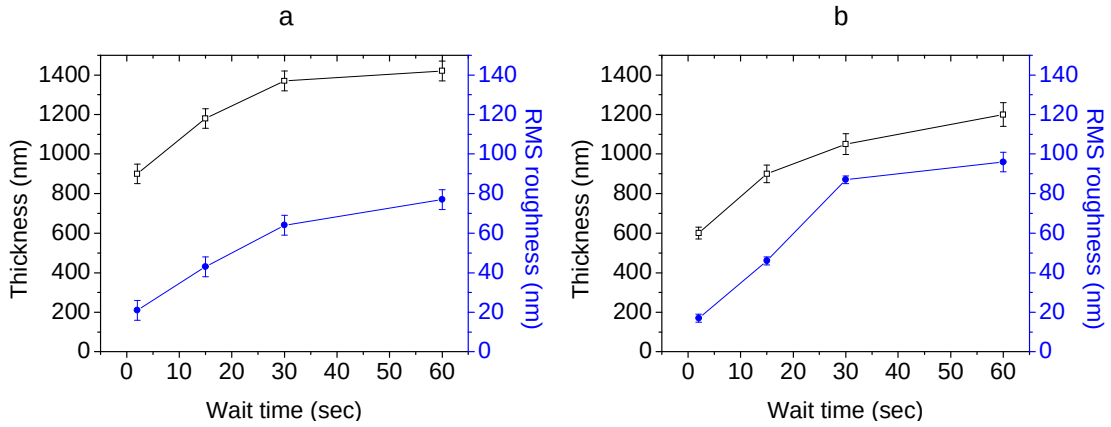

Figure 4.13: Surface roughness and film thickness as a function of pre-spin time for films deposited from 0.5g/ml $As_{42}S_{58}$ (a) and $Ge_{23}Sb_7S_{70}$ (b) deposited on microscope slides at 1000 RPM, and spun for 10 seconds.

From the figure, it can be seen that thickness and roughness increase with increasing wait time. Roughness of these films was found to be very high at 5-10% of the film thickness. Additionally, it can be seen that the $As_{42}S_{58}$ film is slightly thicker, which is attributed to a higher glass loading level. The surface profile of the $As_{42}S_{58}$ film formed with a 60 second wait time is shown below.

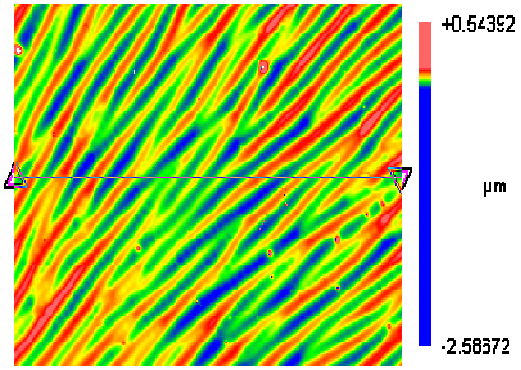

Figure 4.14: Surface profile of $As_{42}S_{58}$ film spun on a microscope slide at 1000 RPM for 10 seconds, with a 60 second wait time.

`

The figure shows a random undulation of the surface with a definite directionality. This image is only a small section of the total surface, and the center of spin for this film is located below and to the left of the image. The pattern is, in fact, radial and centered on the spin axis. This is a very common pattern observed for sol-gel derived films deposited by spin-coating, and is commonly attributed to the Marangoni effect [166], which is caused by an increase in surface tension as the solvent evaporates during spinning. An alternate explanation of this effect is the formation of a "skin layer" as the film begins to solidify at the surface [167], but remains liquid below this layer. In either case, it is the high evaporation rate of propylamine (B.P. = 48 °C) which causes the effect. Figure 4.15 below shows the transmission of the films as a function of pre-spin wait time.

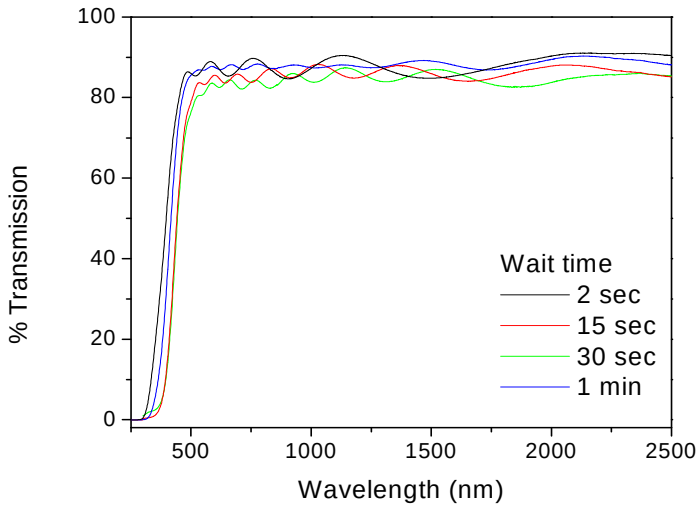

Figure 4.15: Transmission spectra of PA-derived $Ge_{23}Sb_7S_{70}$ as a function of pre-spin wait time

One can see that the films display a periodic variation in transmission in the transparent region, due to optical interference between reflections at the air-film and film-substrate

interfaces. Analysis of these interference fringes can give a measure of the refractive index and thickness, which are related to the fringe strength (ΔT) and spacing ($\Delta\lambda$) [108]. A complication behind these calculations is the influence of thickness inhomogeniety, which gives a different fringe pattern depending on which point on the surface of the film the optical beam passes through. The net effect is that many different patterns, centered around the average thickness, are superimposed in the spectrum, resulting in decreased fringe strength [168]. Thus, while the expected transmission minima for this composition may be expected to be at ~60% (Figure 2.8) due to its high refractive index (2.4), the effect is greatly reduced for these films. As we will show, transmission fringe strength is an alternate method of assessing film thickness uniformity.

As the roughness decreases with a shorter wait-time, all films discussed beyond this point were coated with a minimum pre-spin wait time (1 sec). Figure 4.16 below shows film thickness and roughness as a function of spin rate for propylamine films.

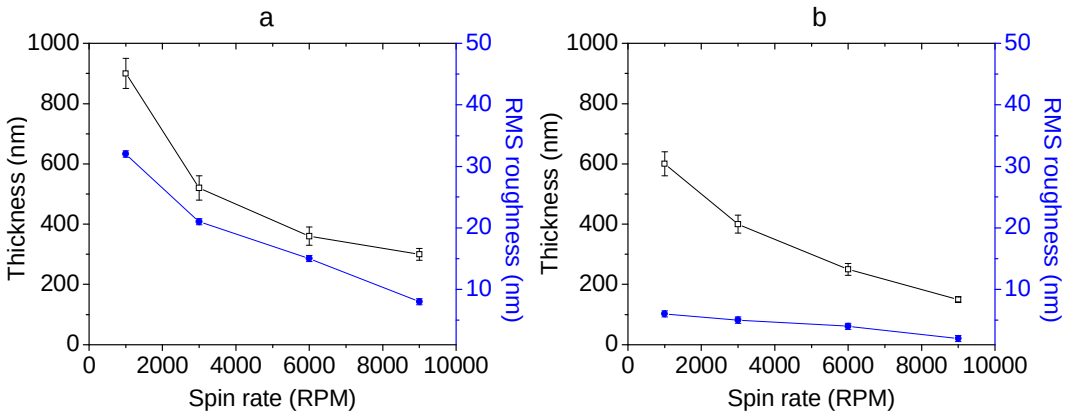

Figure 4.16: Surface roughness and film thickness as a function of spin rate for films deposited from 0.5g/ml $As_{42}S_{58}$ (a) and $Ge_{23}Sb_7S_{70}$ (b) deposited on microscope slides (1s wait time and 10s spin time).

As may be expected, film thickness decreases with increasing spin rate, and as before, the $As_{42}S_{58}$ films are slightly thicker than those of $Ge_{23}Sb_7S_{70}$. Roughness was found to be lower in $Ge_{23}Sb_7S_{70}$ films. In the same way that reaction order was determined using a logarithmic plot, a plot of the logarithm of film thickness versus the logarithm of spin rate was constructed in order to investigate whether thickness follows a power law.

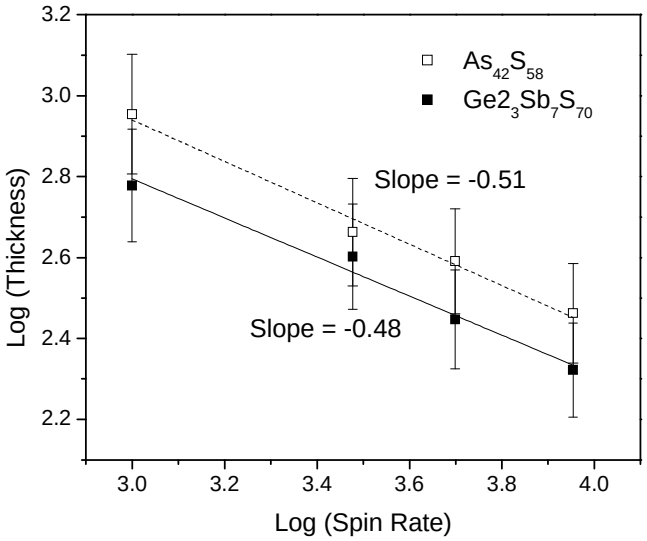

Figure 4.17: log-log plot of spin rate versus thickness for PA-derived thin films.

The linear fit appears to be good, and has a slope of approximately -0.5, indicating that thickness varies with the negative square root of the spin rate. Such a dependence suggests that the effect a high solvent evaporation rate dominates over viscous flow to control the final film thickness [169], which is consistent with our previous observations. Figure 4.18 shows the transmission spectra of propylamine derived films deposited at varying spin speeds.

`

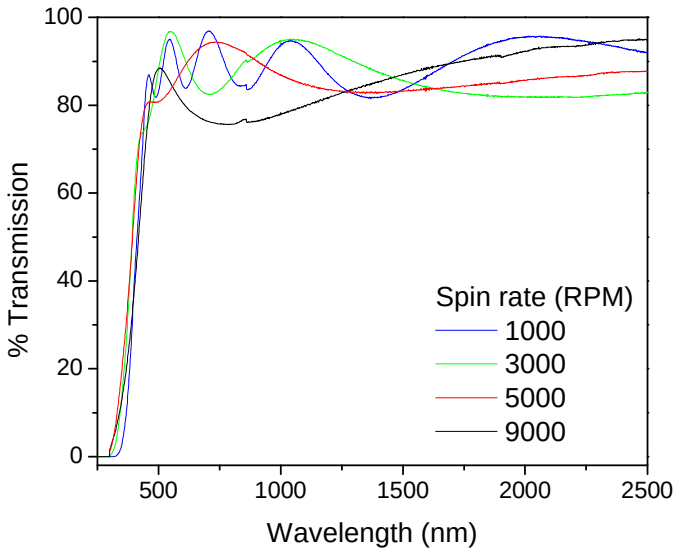

Figure 4.18: Variation of PA-derived film transmission with spin speed.

It can be seen that the size and spacing of the interference fringes increases with increasing spin speed, which can be related to a decrease of the thickness, and an increase of refractive index or homogeneity. Figure 4.19 displays the thickness and roughness of propylamine-derived $As_{42}S_{58}$ and $Ge_{23}Sb_7S_{70}$ film as a function of spin speed.

`

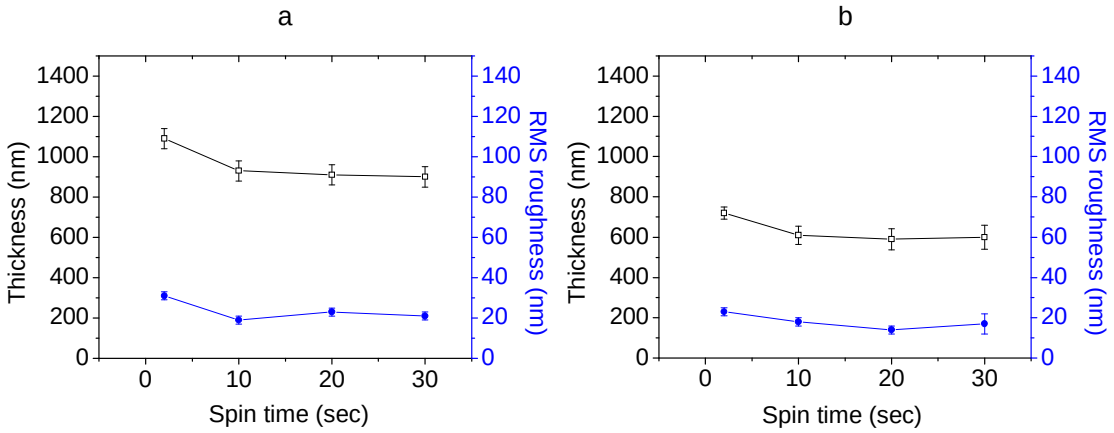

Figure 4.19: Surface roughness and film thickness as a function of spin time for films deposited from 0.5g/ml $As_{42}S_{58}$ (a) and $Ge_{23}Sb_7S_{70}$ (b) deposited on microscope slides (1s wait time,1000 RPM spin rate).

It can be seen that the thickness initially decreases until ~10 seconds. After this time film thickness appears to remain unchanged. Due the high evaporation rate, this likely shows that the solvent has evaporated sufficiently to solidify the film within the first 10 seconds of spinning. For this reason, longer spinning times are not needed.

Thickness and roughness dependence of the other two amine solutions has also been investigated. The addition of a pre-spin hold time was not found to significantly affect the film thickness or roughness, probably due to their lower evaporation rates (higher boiling points). The figure below presents the roughness and thickness of $As_{42}S_{58}$ (left column) and $Ge_{23}Sb_7S_{70}$ (right column) in ethylenediamine (upper row) and ethanolamine (lower row).

`

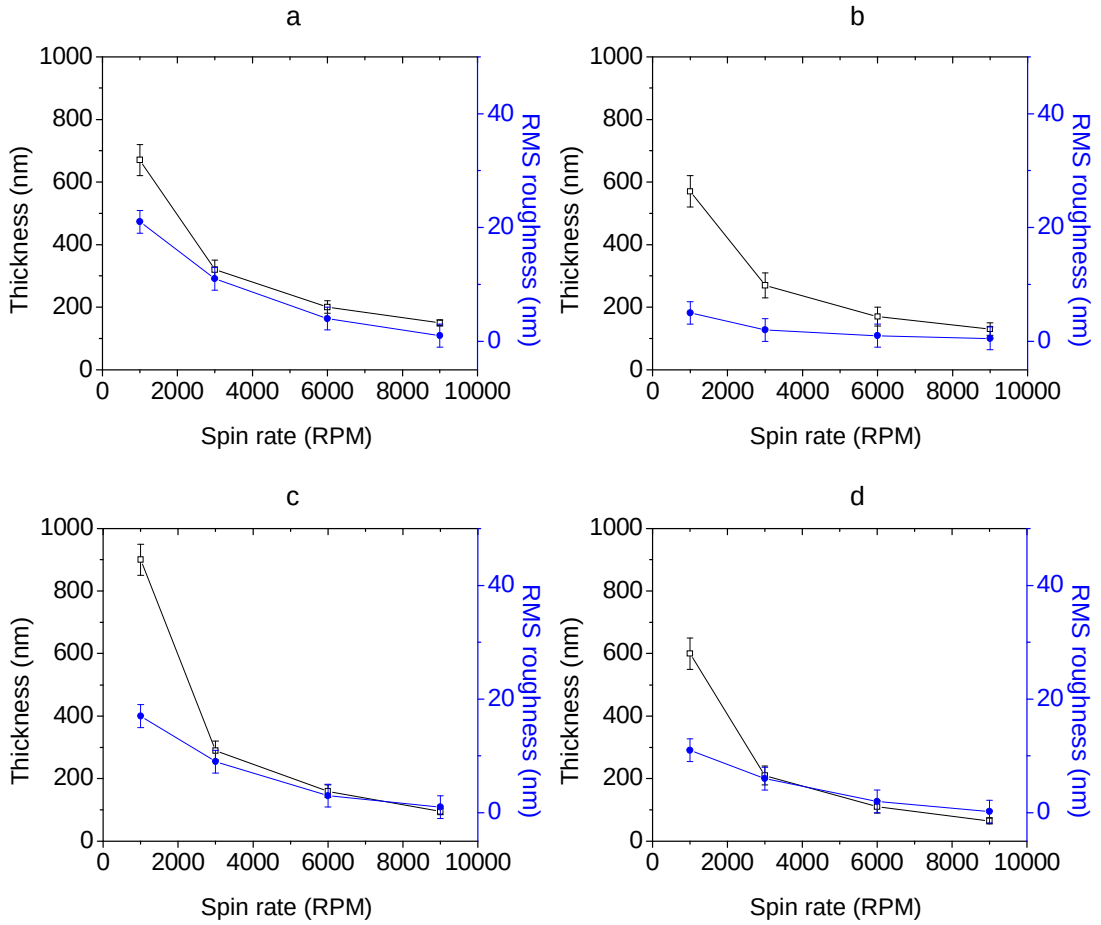

Figure 4.20: Surface roughness and film thickness as a function of spin rate for films deposited from 0.5g/ml $As_{42}S_{58}$ (a, c) and $Ge_{23}Sb_7S_{70}$ (b, d) in ethylenediamine (a, b) and ethanolamine (c, d) deposited on microscope slides (1s wait time and 10s spin time).

As with propylamine, the films become thinner at higher spin rates, with $As_{42}S_{58}$ films being slightly thicker, and $Ge_{23}Sb_7S_{70}$ films having lower roughness. Log-log plots give slopes of -3/4 and -1 for ethylenediamine and ethanolamine respectively, showing decreasing effects of evaporation which may be expected from their boiling points. Ethanolamine films are slightly thicker due to higher viscosity of the solvent. The

`

evolution of film thickness and roughness with spin time for ethylenediamine and ethanolamine solvents are shown in Figure 4.21

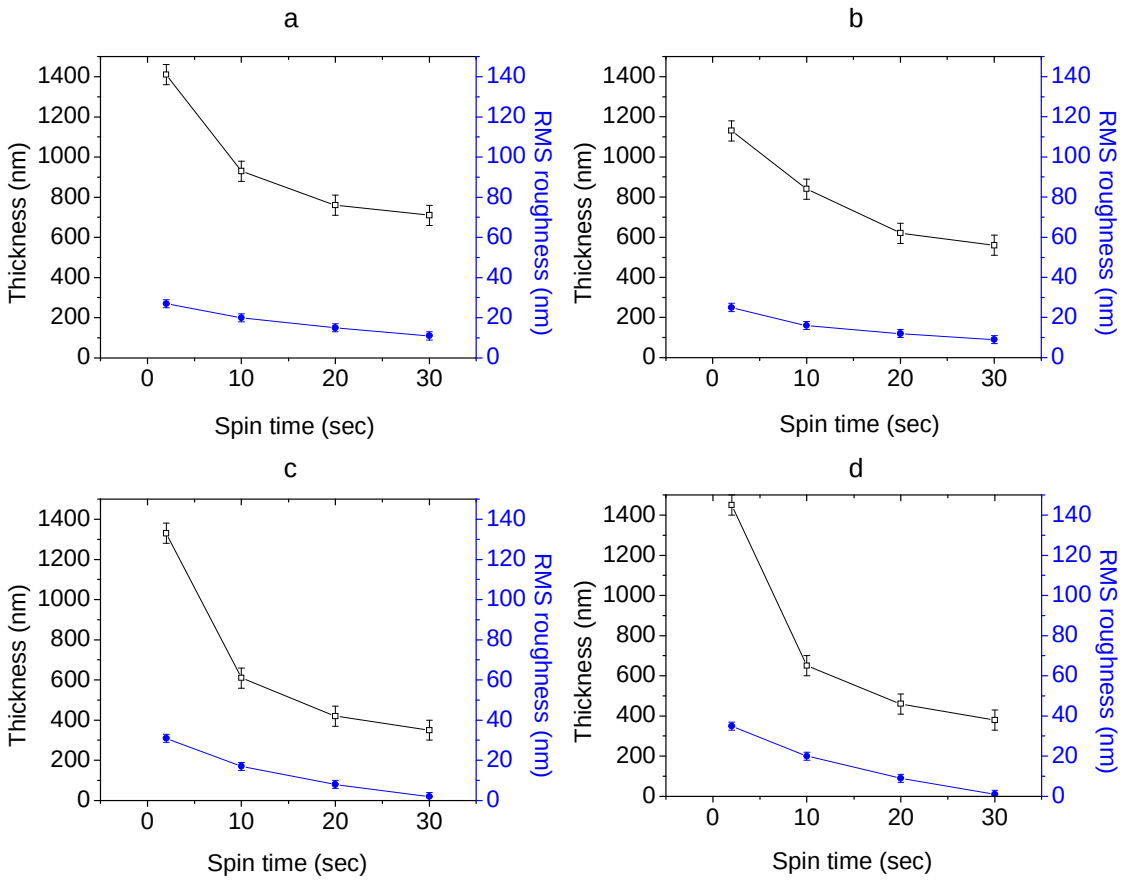

Figure 4.21: Surface roughness and film thickness as a function of spin time for films deposited from 0.5g/ml $As_{42}S_{58}$ (a, c) and $Ge_{23}Sb_7S_{70}$ (b, d) in ethylenediamine (a, b) and ethanolamine (c, d) deposited on microscope slides (1s wait time and 1000 RPM spin rate).

It can be seen that film thickness does not become constant after a few seconds, as with propylamine, but continues to decrease. Additionally, the ethanolamine films appear to thin out more over time than do the ethylenediamine films, which is probably due to the lack of any significant evaporation of ethanolamine during spinning.

`

Finally, the effect of an additional hold time added to the end of the spinning cycle and before the start of the heat treatment was examined. No significant changes in either thickness or roughness were found in propylamine or ethylenediamine derived films, however, a significant reduction of RMS roughness from 6.3 to 0.5 nm for a 400 nm ETA-derived thick film was observed. Figure 4.22 demonstrates the difference in surface profile for a film with and without a 30 second post-spin hold before heat treatment.

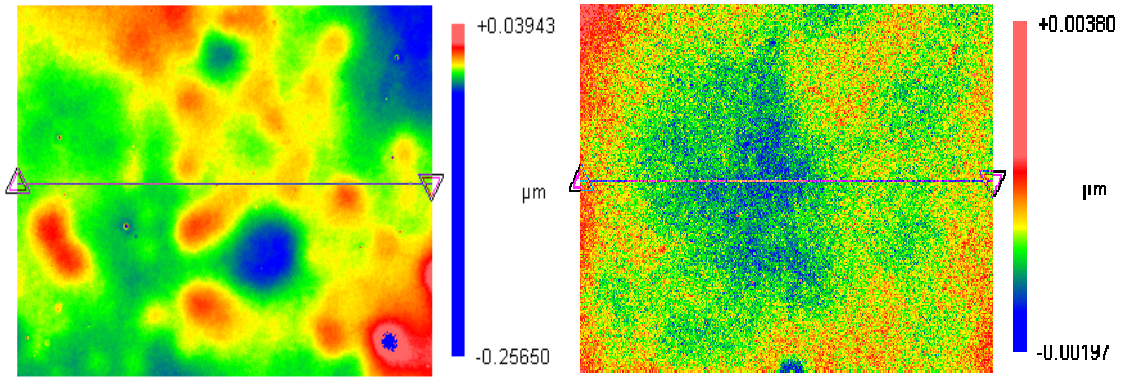

Figure 4.22: Surface profile of 400nm films ethanolamine-derived (ETA) $As_{42}S_{58}$ with (a) and without (b) a 30 second post-spin hold.

This effect is attributed to the low volatility of this solvent, which appears to remain liquid after the coating process. The smoothing effect can be monitored and is clearly apparent to the unaided eye. This added reduction in roughness makes this solvent highly attractive for optical applications. As is commonly observed during spin coating, a small bead of solution often remains at the edge of the substrate after spinning. Because this coating remains liquid, the excess at the edge flows back toward the center of the substrate during this hold time. This leads to a large area of non-uniform thickness around the outside edge, particularly for small irregularly shaped substrates such as

microscope slides. For device applications, this limitation can be avoided by selecting of an appropriate substrate (large diameter circles such as Si wafers).

For propylamine films, the high evaporation rate does not allow the control of film thickness using the spin time. Combined with the narrow solubility ranges observed for this solvent, this requires thickness control using spin speed alone. For the other two solvents, elimination of the edge bead requires a high spin speed (> 3000 RPM). This induces rapid thinning of the film. In order to produce films with thicknesses above 300 nm, short spin times or higher glass loadings are needed. Unfortunately, the low solubility of Ge-based glasses requires film thickness control using spin time alone.

Based on the findings thus far, we have shown that both $As_{42}S_{58}$ and $Ge_{23}Sb_7S_{70}$ thin films can be prepared, but $As_{42}S_{58}$ is preferred due to its higher solubility and the opportunity to use solutions of higher viscosity. All three investigated amines were also shown to be effective in spin coating, however ethanolamine is preferred due its lower evaporation rate and higher viscosity. This solvent also allows fabrication of low roughness, high uniformity films through addition of post-spin (pre-bake) hold.

4.4 Optimization of the heat treatment conditions

Heat treatment of the spin-coated films has two primary purposes. The first is the solidification of the film in order to fix its morphology. ChG's are known for their high IR transparency [170], which is our main reason in selecting these materials. The second purpose is therefore the removal of residual solvent, which typically has an undesirable fingerprint within the IR spectral region of interest for sensing applications. Organic

molecules tend to have absorptions in the mid-IR region, which are characteristic of the different bonds within the molecular structure. This is useful for detection and speciation of organic analytes, but may reduce the transparency of the ChG film in these key regions. In many ceramic systems, high temperature thermal treatments above 1000 °C are used to remove residual organic solvents and/or binders by thermal degradation. Unfortunately, as shown in chapter three, these glasses have a T_g in the range of 200-300 °C, making such treatments impossible. Instead, we will attempt to remove the solvent by heating the films above their solvent boiling points, allowing it to gradually diffuse through the film. The use of low pressures during vacuum heat treatments has the added effect of reducing the boiling point of the solvent, while leaving the T_g of the glass unaffected, and keeping the partial pressure of solvent vapors above the film low, through active pumping.

For these reasons, the heat treatments were broken into two separate steps. The first is a short, low temperature heat treatment intended to dry and solidify the film, making it stable enough to be handled and removed from the inert environment in which it was coated (dry N_2). This was done by placing the film on hot plate at 90 °C for a period of 5 minutes to one hour under N_2 atmosphere. After the completion of this “soft bake”, the films were removed from the glove box, and were placed into a vacuum oven. The oven was then purged with N_2 and evacuated to a pressure ~1 Torr. The films were heated to the hard-bake temperature (90-250 °C) at a rate of 2-3 °C/min, and held for a period of 1-48 hours before being cooled to 60°C at a rate of 1°C/min before being

removed to the air. All films were stored in a darkened vacuum desiccator (~10 Torr) in order to prevent any potential reaction with moisture, oxygen or room light.

Figure 4.23 below shows the evolution of the transmission spectra of a $Ge_{23}Sb_7S_{70}$ film with increasing hard-bake temperature. This combination of glass and solvent was chosen in this case because the glass has the highest T_g (305 °C) of those studied while the solvent has the lowest boiling point (47 °C). This combination should allow the most effective removal of excess solvent, as it can be heated far above the boiling point of the solvent, but still below the T_g of the glass.

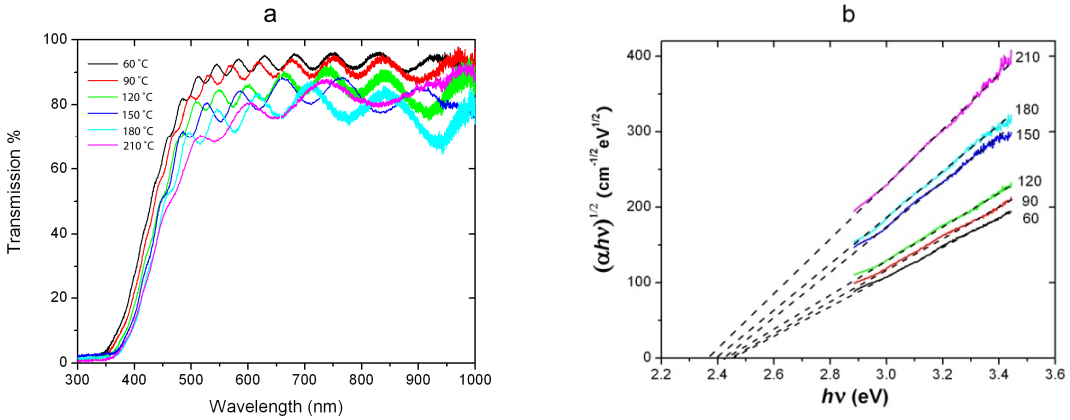

Figure 4.23: Transmission spectra and Tauc band gap plots for PA-derived $Ge_{23}Sb_7S_{70}$ films after treatment at varying hard bake temperatures

One can see that an increase of the hard-bake temperature causes an increase of the height and spacing of the interference fringes in the transmission spectra, reflecting an increase of refractive index and decrease of thickness, as well as a red shift of the absorption band gap. Figure 4.23b shows the Tauc absorption plots derived from the transmission spectra. From these figures, the film thickness, refractive index and band

gap were calculated [108], and are shown as a function of hard-bake temperature in the following figure.

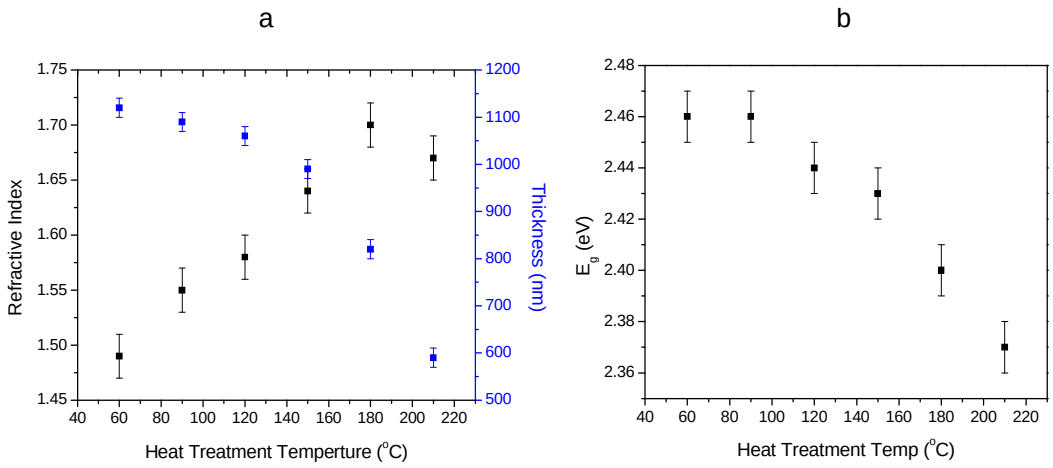

Figure 4.24: Variation of refractive index and thickness (a) and band gap (b) of $Ge_{23}Sb_7S_{70}$ with films hard-bake temperature, calculated from transmission spectra

It is the clear that band gap and film thickness decrease and refractive index increases as the hard-bake temperature increases. While the refractive index appears to decrease after 180 °C the band gap and thickness both decrease dramatically as the hard-bake temperature continues to rise. Initial thinning of the film and band gap shift are presumed to be caused by densification and removal of remaining excess solvent in the film, as it is linked to an increase in the refractive index and therefore density. Because the index begins to decrease above 180 °C, it is likely that an additional cause of this further thinning of the film occurs. This is probably the onset evaporation of materials from the film, which is associated with the refractive index reduction. The following figure displays the refractive index, thickness and band gap of $As_{42}S_{48}$ films as a function of heat treatment temperature.

`

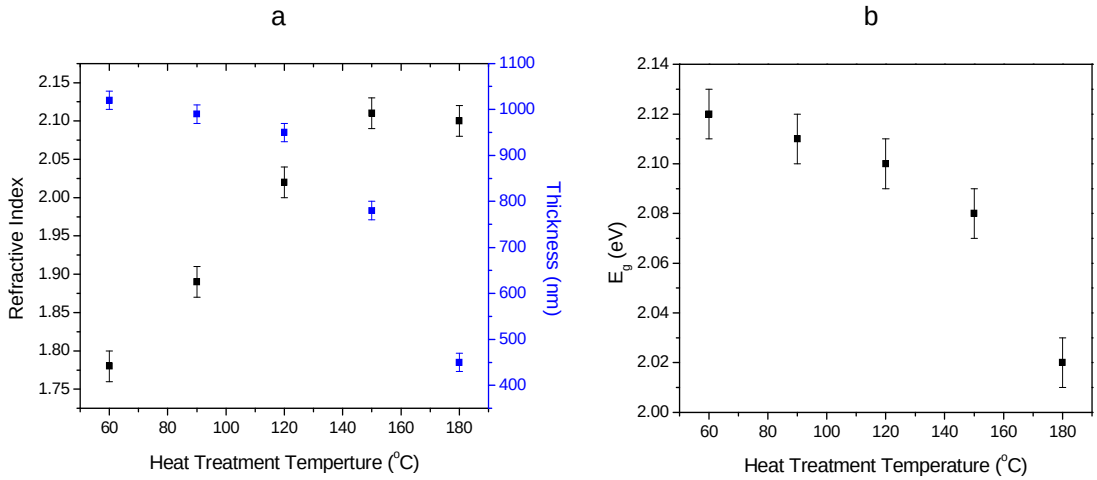

Figure 4.25: Variation of refractive index and thickness (a) and band gap (b) of $As_{42}S_{58}$ with films hard-bake temperature, calculated from transmission spectra

As with the Ge-based films, an increase of the refractive index with a decrease of thickness and band gap are observed. It is also important to note that data for 210°C heat treatment is not presented, which is because the film was found to have completely evaporated from the substrate. A yellow coloration was also observed on the window of the vacuum oven for high temperature treatments of either composition, which could indicate a loss of mass from the film, however, no significant change in the EDS composition was observed. By comparing the refractive index of the films to the bulk glass using the Lorenz-Lorentz relation (equation 2.2), the film density is expected to reach 72% and 88% of the bulk density for $Ge_{23}Sb_7S_{70}$ and $As_{42}S_{58}$ respectively. It should be noted that this assumes the void space is filled with air (n=1), however it is also possible that film porosity represents the presence of residual amine (n=1.3).

Attenuated total internal reflection (ATR) Fourier-transform infrared spectroscopy was used to monitor the amount of residual solvent in the films. The

`

following figure displays the spectra of ~1µm thick films of $As_{42}S_{58}$ after 1 hour hard bake at temperatures between 90 and 180 °C.

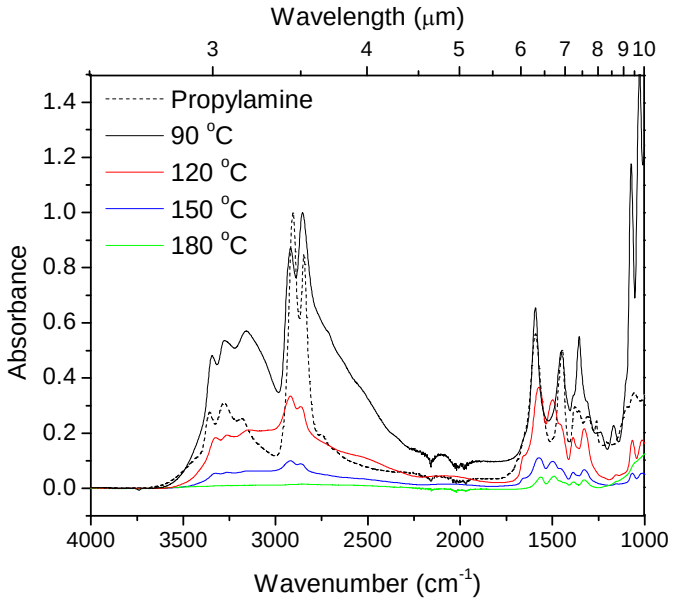

Figure 4.26: FTIR transmission spectra of ETA-derived $As_{42}S_{58}$ films with varying hard-bake temperature

Several important features are observed in the spectra which are also found in the spectrum of the solvent. In the high wavenumber region, the sharp doublet peak near 2900 cm^{-1} is attributed to the stretch of the two N-H bonds, while the broad feature form 3000-3500 cm^{-1} is attributed to the various C-H bond stretches. Features in the low wavenumber region, from 1500 to 1000 cm^{-1}, commonly referred to as the fingerprint region, are attributed to various stretching and bending modes within the carbon backbone. Finally, the peak at 1600 cm^{-1} is attributed to the C-N bond stretch. Because the ATR technique relies on absorption the evanescent field reflected inside a crystal which is in contact with the sample, normalization of absorbance to the film thickness is not appropriate. The shape of the spectra in the range of 2000-2200 cm^{-1} is attributed to

`

background absorption from the ATR crystal (diamond). Peak absorbance values for the features at 1600 and 2900 cm^{-1} as a function of hard-bake temperature are shown in Figure 4.27 below.

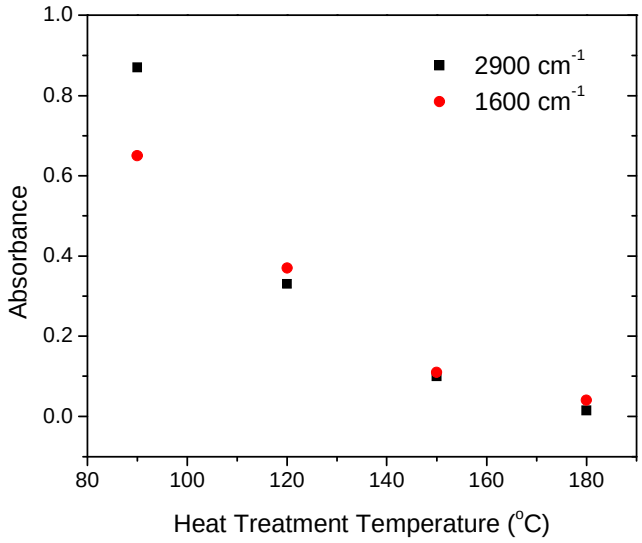

Figure 4.27: Variation of peak absorbance at 1600 and 2900 cm^{-1} from transmission spectra of ETA-derived $As_{42}S_{58}$ films with varying hard-bake temperature

The absorbance at 2900 cm^{-1} decreases from 0.87 to 0.015 while that at 1600 cm^{-1} decreases from 0.65 to 0.04 with increasing heat treatment temperatures. It is interesting to note that the peak at 2900 cm^{-1} shows larger rate of decrease than that at 1600 cm^{-1}. If it is assumed that the molar absorprtivity of the solvent remains constant with concentration during heat treatment, this indicates that the relative number of N-H bonds in the film is decreased more than the number of C-N bonds. One possible explanation of this observation is the formation and subsequent loss of volatile H_2S by conversion of N-H bonds to S-H bonds upon heating, leading to the retention of a small number the

`

organic molecules which become bonded into the structure of the film. This may account for the observation of a yellow discoloration of the oven after high temperature heat treatments. These results do indicate that is possible to remove most of the residual organic during heat treatment, up to 94-98%, depending on which peak is referenced.

4.5 Bulk-film structural comparison

It is well known that deposition of As-S based thin films by thermal evaporation of thin proceeds through the breakup of the network into molecular units including small As-S clusters, including As_4S_6 as well as As_4S_4 and short S_n chains [120, 122, 171]. These small molecules have relatively high vapor pressures and are easily liberated from the surface. It is also important to note that repolymerization of the glass network from the vapor results in films which have different structures from the bulk glass. The dissolution of the bulk glass is also expected to create small molecular structures, and film formation does not necessarily recreate the structure of the bulk glass. For this reason, we have compared the structure of the films to the bulk glass, which is shown for ~1 µm thick $Ge_{23}Sb_7S_{70}$ films derived from ethanolamine solutions.

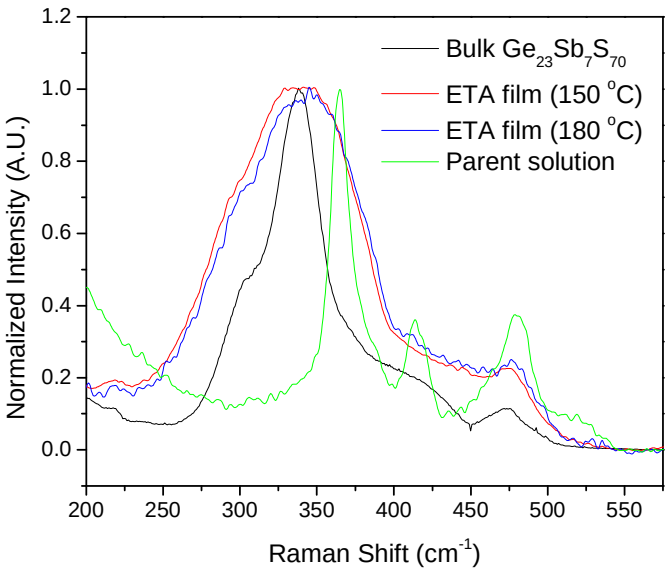

Figure 4.28: micro-Raman spectra of $Ge_{23}Sb_7S_{70}$ films after 150 and 180 °C hard bake, as compared to the bulk glass and parent solution.

It is clear that the structure of the film is similar to that of the bulk glass and quite different from that of the solution. The bands near 300 cm^{-1} and 475 cm^{-1} attributed to SbS_3 units and S-S bonds bulk glass are observed in the spectrum of the film. The main band of the films (centered near 350 cm^{-1}) is significantly broader than that of the bulk glass. This is attributed to the overlap of several bands corresponding to GeS_4 units linked by S-S bridges, corner-shared S atoms in Ge_4S_{10} clusters at 330 340 and 360 cm^{-1}, and the broad shoulder from 375 to 425 cm^{-1} is attributed to Ge-S-Ge bridges and $Ge_2S_2S_{4/2}$ bitetrahedra. The fundamental units comprising the structure of the films is found to be the same as those in the bulk glass (except Ge_4S_{10} which is observed only in the solution), however, the greater width of the main band indicates a wider distribution of bonding forms (bond angles) between units. This may be interpreted as a decrease in medium

`

range order. In comparing the spectra of the films heat treated at 150 and 180 °C, the only significant change is a slight narrowing of the main band which, based on the above interpretation, may be linked to an increase of medium range order.

Figure 4.29 displays the X-Ray diffraction patterns for $Ge_{23}Sb_7S_{70}$ films as a function of heat treatment temperature. The XRD spectra of the glasses were recorded using a Shimadzu XD-3A instrument with a Cu Kα X-ray source at 1.5418 Å, scanning 2θ from 5° to 80° with a step size of 0.02°. Bulk glasses were optically polished and mounted on an aluminum sample holder for measurement. Thin film patterns were obtained for films still on the substrate (not powder).

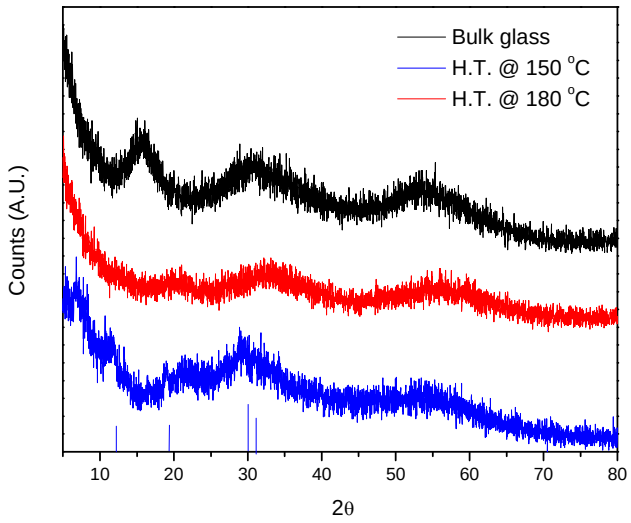

Figure 4.29: X-Ray diffraction pattern of $Ge_{23}Sb_7S_{70}$ films after 150 and 180 °C hard-bake, as compared to the bulk glass.

The diffraction pattern of the bulk glass shows three very broad features, often described as an amorphous halo. This is caused by the regularity of the types of molecular units in the glass, also known as short range order. The diffraction patterns of the films show a

similar shape for this halo, but small sharp features begin to be apparent in the film heat treated at 180 °C. This can be viewed as the initial onset of crystallization in the film, indicating subtle organization of the structure over the intermediate range, as observed in the Raman spectra. For this reason, as well as continued thinning of the film, heat treatments above 150 °C are not recommended.

The X-Ray diffraction patterns of the $As_{42}S_{58}$ films, compared to that of the parent bulk glass, are shown in Figure 4.30.

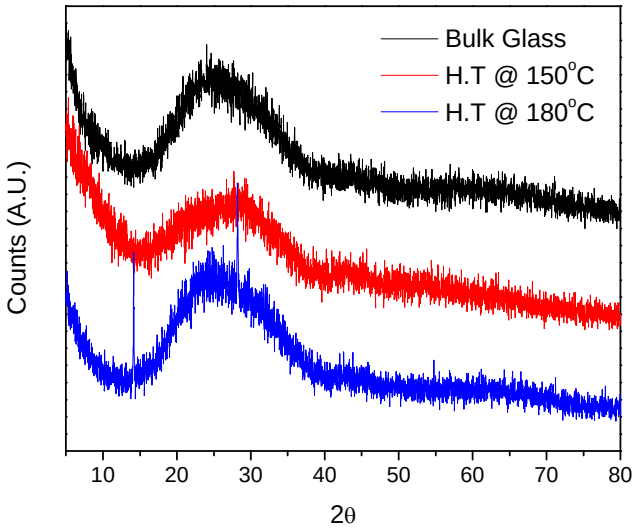

Figure 4.30: X-Ray diffraction pattern of $As_{42}S_{58}$ films after 150 and 180 °C hard-bake, as compared to the bulk glass.

As observed for the Ge-based films, the diffraction patterns of the As-based films are similar to that of the bulk glass, indicating a similar short range order. Upon heat treatment at 180 °C two sharp peaks appear which correspond to the two largest peaks found in the pattern of the mineral Realgar, which is comprised of As_4S_4 clusters [121]. We can therefore conclude that the formation of films from solutions of $As_{42}S_{58}$ results in

the repolymerization of dissolved units to form a network of $AsS_{3/2}$ units with a relatively large number of As-As and S-S bonding defects and lower medium range order compared to the bulk glass. Heat treatments above 150° C cause the crystallization of As_4S_4 clusters from the network, also inducing the formation of S_n chains. These small units, having a relatively high vapor pressure can then rapidly evaporate from the surface of the film at still higher temperatures (210 °C) leading to a complete evaporation of the film from the substrate when under vacuum. As with $Ge_{23}Sb_7S_{70}$, heat treatments of $As_{42}S_{58}$ films above 150 °C are not recommended due to the onset of crystallization at higher temperatures.

The following figure compares the Raman spectra of ethanolamine-derived $As_{42}S_{58}$ films after heat treatment at 150 and 180 °C for one hour with those of the parent bulk glass and solution.

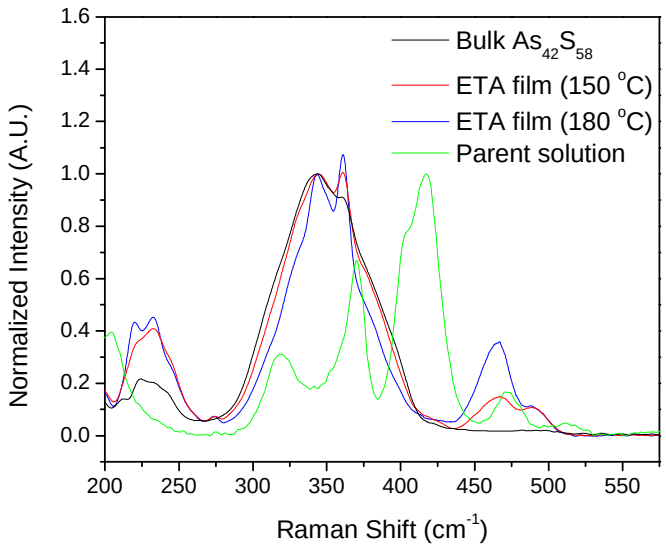

Figure 4.31: micro-Raman spectra of $Ge_{23}Sb_7S_{70}$ films after 150 and 180 °C hard bake, as compared to the bulk glass and parent solution.

As observed for the Ge-based film, the structure of this film is similar to that of the bulk glass, indicating that the network structure of the glass is mostly restored during heat treatment. The main band in the region of 300-400 cm^{-1} is attributed to vibrations of $AsS_{3/2}$ units. The spectra of both films show sharp features near 220 and 365 cm^{-1}, attributed to As_4S_4 molecules and a band near 235cm^{-1} attributed to As-As bonds in $S_{2/2}As\text{-}AsS_{2/2}$ network units. The intensity of these bands in significantly higher in the spectra of the films as compared to that observed for the bulk glass, indicate these features a relatively larger concentration of As-As bonds. As discussed in chapter 3, this should be balanced by an increase of S-S bonds because significant variation of the composition of the films from that of the bulk glass was not observed.

`

This is demonstrated the appearance to two bands near 470 and 490 cm^{-1} respectively in the Raman spectrum (Figure 4.31), which are attributed to the presence of S-S bonds in S_n chains and S_8 rings. In comparing the Raman spectra of the films treated at 150 and 180 °C, the intensity of the bands near 220, 365 and 470 cm^{-1} increase dramatically. This indicates an increase in the relative number of As_4S_4 clusters and S_n chains and S_8 rings with higher temperatures.

As the heat treatment temperature range is limited, it may be difficult to achieve low residual solvent levels, particularly for films derived from high boiling solvents like ethanolamine. Longer duration treatments may provide a solution to this problem. The figure below shows the FTIR absorbance spectrum of freshly deposited ethanolamine-derived $As_{42}S_{58}$ film (deposited on a silicon wafer) and that of the same film after 8 hours at 150 °C under vacuum.

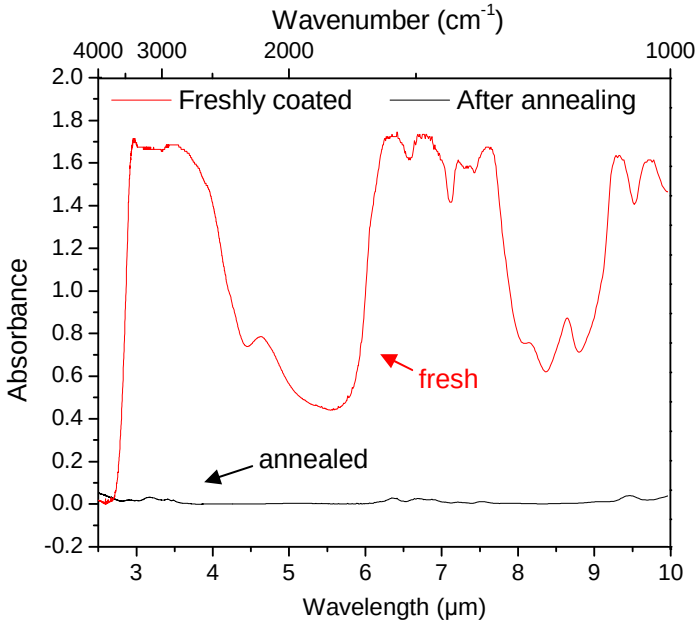

Figure 4.32: FTIR transmission spectra for as-deposited and heat treated (150°C for 8 hours) ETA-derived $As_{42}S_{48}$ film.

`

The spectrum of the as-deposited film shows several large absorption features, these appear to have a relatively constant absorption value due to saturation of the detector of spectrometer. It can be seen that the amine content may be dramatically reduced even without treatment at higher temperatures. The absorption spectrum of the heat treated film with an expanded y-axis from Figure 4.32 is shown in Figure 4.32 below.

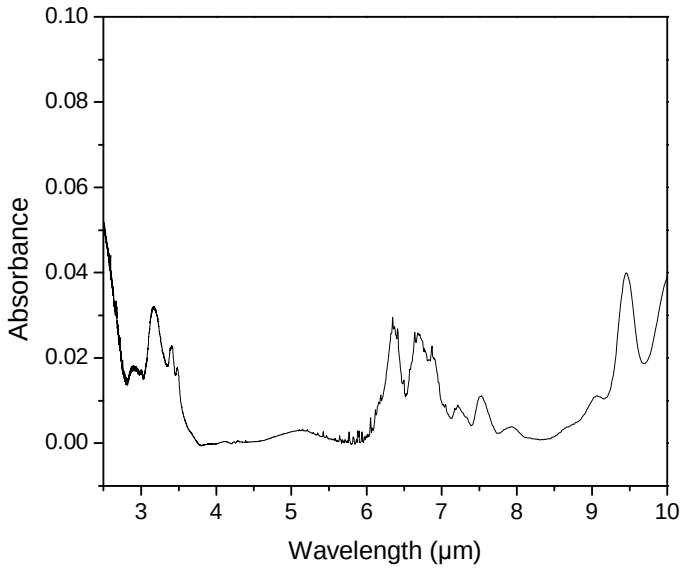

Figure 4.33: Enlargement of long-term hard-baked ETA-derived $As_{42}S_{58}$ film spectrum from figure 4.32

The features at 3.4 and 6.5 μm (2900 and 1600 cm^{-1}) can again be attributed to N-H and C-N bond vibrations. The reduction of the absorbance from ~1.9 to 0.03 indicates a reduction of the organic content of at least 98%, and probably more due to the observation of saturation in the absorbance spectrum of the as-deposited film. It is therefore possible to replace higher temperature heat treatments with treatments at lower temperatures and longer durations. It is important to note that no significant thinning or crystallization of the films was observed after this long duration heat treatment.

`

Based on a summary of the above results it is possible to define an optimized method for the deposition of chalcogenide thin films. Bulk glasses may be dissolved in pure primary or secondary amine solutions by stirring the powdered glass in the solvent for a period of up to 48 hours. The ratio of glass to solvent must be chosen based on the chemistry of the particular glass and solvent. The selection of glasses with high Ge or excess S content or solvents of low polarity are expected to result in decreased solubility. Once a precipitate-free solution is obtained, films may be deposited by spin coating.

Coating thicknesses for films derived from solvents of high vapor pressure are best controlled by varying spin speed, while films derived from low vapor pressure solvents are best if coated using a relatively high spin speed (3000 rpm) and short times (< 10 seconds) may be used to prevent excess thinning of the film. The use of solvents which do not appreciably evaporate (ethanolamine in this case) allow the relaxation of spinning-induced thickness variations and surface roughness giving better then 1nm surface roughness by incorporating a post-spin hold before heat treatment. Bulk glass should be dissolved in dry (water-free) solvents and all dissolution and coating steps should be performed under a dry inert atmosphere (N_2) to prevent the formation of oxides in the solution.

Heat treatment after coating is necessary to remove residual solvent from the film. Because of their sensitivity to moisture, films should be solidified by the use of a low temperature heat treatment (soft-bake) before removal from the inert atmosphere. A 5 minute exposure to 90°C on a hot plate was found to be sufficient for this purpose, but it

is important to note the moisture sensitivity of the film is only reduced by this step and exposure to air should be kept short (5-10 min), particularly if humidity is high. In order to fully remove the solvent and provide a stable film, a second high temperature (hard-bake) treatment should be performed. Crystallization and slow evaporation of the films was noted for hard-bake temperatures above 150 °C, indicating that this is the maximum useful temperature for this treatment. If full removal of the residual organics is desired, long treatment time (24-48 hours are preferred). For solvents which have boiling points above 150 °C, such as ethanolamine, the hard-bake must be performed under vacuum (< 1 Torr), but vacuum is preferred to inert atmosphere for all hard-bake treatments due to high solvent removal rates. If the solvent is not allowed diffuse slowly thought the film, cracking or bubbling of the film will result, thereby reducing the film's optical quality. For this reason, the 2-stage heat treatment protocol described above is preferred to single stage (hard-bake only) heat treatment schedules, and slow temperature ramp rates of 2°/min are desired. Film structure and properties were found to correspond well to those of the parent bulk glasses, but with broader variety of structural units comprising the network.

4.6 Summary of findings

In this chapter, examination of the mechanism for dissolution of chalcogenide glasses in basic solvents and optimization of the process parameters for spin-coating of films from dissolved bulk solutions has shown:

1) The glass dissolution mechanism has been interpreted based on the Pearson "hard-soft" acid base concept. Aminolysis through nucleophilic substitution identified as the dissolution mechanism, requiring that solvent have a labile hydrogen (N-H bond). Chemical softness (high polarizability) and polarity (high dielectric constant) solvents are more important that basicity in determining dissolution rate and solubility limits.

2) An optimized film deposition protocol was defined. Ethanolamine identified as preferred solvent due to improved solubility limits, increased solution viscosity, and reduced evaporation rates. As-based compositions were shown to provide high quality fins due to improved solubility. High spin rates (> 2000 rpm) with short spin times were shown to be preferred for ethanolamine and ethylenediamine solvents, thickness controlled in these solvents was achieved using spin time. The high vapor pressure of propylamine was found to necessitate careful handling to prevent excess evaporation, and thickness control using spin speed.

3) A heat treatment procedure which provides films with high density and amorphous bulk-like glass network structure was identified. A preliminary soft-bake at 60-90 °C for 5 minutes under inert atmosphere immediately after spinning may be used to solidify film, stabilize it against moisture and oxidation, and to fix the morphology. A long hard-bake at 150 °C in vacuum for at least 8 hours may

then be used to remove residual solvent in order to give the highest possible density and IR transparency. Hard-bake temperatures above 150 °C resulted in crystallization and gradual evaporation of chalcogenide material, particularly for As-based glass.

4) Solution-derived films possess a similar structure to that of the parent bulk glass after the hard-bake treatment, but containing a relatively larger number of As-As and S-S wrong bonds. It is important to note that traditional deposition methods such as thermal evaporation, follow a similar pattern, including the break-up of the network into small molecules which finally reform a glassy network upon annealing [172].

CHAPTER FIVE

Novel Chalcogenide Materials

5.1 Chalcogenide glass / polymer hybrid coatings

By taking advantage of the solution phase, novel combinations of materials become available. One material system which has been of great interest in recent years is glass-polymer hybrids [84-90, 94-97, 173, 174]. The primary advantage in combining these two materials into a composite or hybrid system is the combination of high hardness from the glass phase with ductility from the polymer phase for increased mechanical durability. One of the limiting factors in the application of these materials is low transparency due to phase separation [88]. The scattering of light by inhomogeneities is described by Mie theory [175], and is defined by the a characteristic dimension (x):

$$x = \frac{2\pi r}{\lambda} \tag{5.1}$$

Where r is the radius of the particle and λ is the wavelength of light. When x is small, the generalized form reduces to the case Rayleigh scattering. The Rayleigh scattering cross section for a spherical particle in a matrix is given by:

$$\sigma_s = \frac{2\pi^5}{3}\frac{d^6}{\lambda^4}\left(\frac{n_p{}^2 - n_m{}^2}{n_p{}^2 + 2n_m{}^2}\right)^2 \tag{5.2}$$

Where d is the diameter of the particle and n_m is the refractive index of the matrix and n_p is the refractive index of the particle. This shows that there are two ways to reduce scattering and increase transparency in a phase separated material. The first is by reducing the index mismatch between the particle and matrix ($n_p - n_m$), and the second is

by decreasing the ratio of particle size to wavelength. As we have shown, the refractive index of chalcogenide glasses is generally above 2.0; however, the index of most polymers is 1.4-1.5 which makes index matching impossible in this material system. Because scattering scales with d^6 and λ^{-4}, decreasing the size of a particle from λ, the target wavelength of use, to $\lambda/2$ or $\lambda/4$ will reduce the scattering by 98% and 99.98% respectively. As optical loss is important for sensor applications, we can use this to define to types of inhomogeneous materials: "composites", where the characteristic size of the microstructure, d, is large enough to induce significant scattering and the wavelength of operation ($d > \lambda/2$) and "hybrids", where the microstructure is small enough to make the sample transparent ($d < \lambda/4$). Thus, hybrid materials may be seen as essentially optically homogenous materials, whereas composites are optically inhomogeneous. Because the wavelength of interest for chalcogenide glasses is in the near- and mid-IR (λ =1-8 μm), where the optical absorption of the glass itself is also low, this gives a maximum size for phase separation or inclusions on the order of ~250 nm. While many attempts to create such materials have previously been made [84-90, 94-97, 173, 174], none to date have combined polymers with IR transparent materials in a way which is homogenous over these length scales.

The primary goal in this effort therefore, was to identify a polymer which can be dissolved into the glass solution and which can be either deposited homogenously or in a form in which phase separation may exist over length scales below 250 nm. As a starting point, polymethylmethacrylate (PMMA) was selected as the polymer, as it is commonly used in optical fibers and $As_{42}S_{58}$ was selected at the glass because of its better solubility.

It was however found that solid PMMA (M.W. = 100,000) would not dissolve into glass-containing solutions, due to the formation of a yellow precipitate at the polymer surface which inhibited dissolution. Instead, solutions of dissolved PMMA and dissolved $As_{42}S_{58}$ were mixed. Solutions which used a mixed solvent system such as PMMA/Acetone and $As_{42}S_{58}$/ethylenediamine (EDA) were found to induce precipitation of the glass upon mixing, even if the two solvents are miscible. Finally, it was found that two solutions could be mixed together to produce a stable co-solution if the same solvent was used to dissolve both the glass and polymer and these were mixed together. In the case of PMMA, the only appropriate solvent was EDA, due to the low solubility's of PMMA in ethanolamine (ETA) and glass in propylamine (PA). A four-step procedure was defined for producing stable EDA co-solutions:

1) Solution A: Dissolve 200mg/ml $As_{42}S_{58}$ in EDA heated to 80 °C

2) Solution B: Dissolve 5-20mg/ml PMMA in EDA heated to 80 °C

3) Add solution A to solution B while at 80°C and stir until clear

4) Add to equal volume room temperature EDA to give 50mg $As_{42}S_{58}$ + 5mg PMMA per ml solution and allow to cool.

These solutions were found to be stable for up to 1 week without precipitation or separation of either component form the solution, but over longer times, PMMA slowly precipitated from solution. Films were prepared from these solutions by spin coating, as described above, but all films were found to be opaque. The microstructure of the film was investigated using scanning electron microscopy, and an image of the film surface taken at 500x magnification.

`

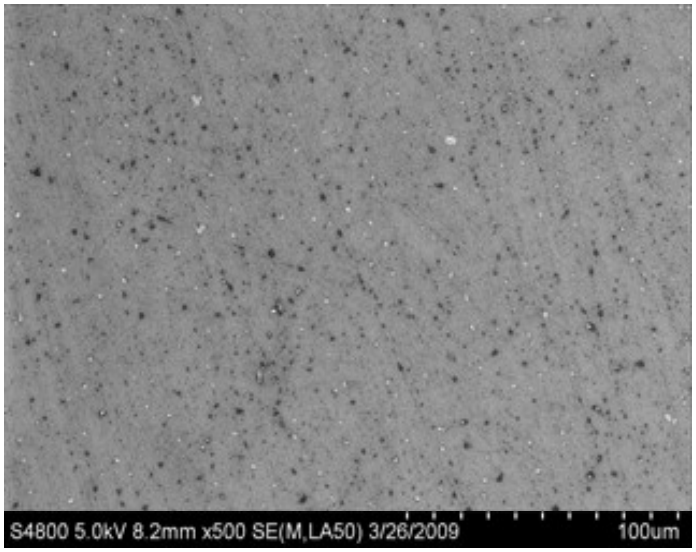

Figure 5.1: SEM micrograph EDA-derived 25% PMMA/$As_{42}S_{58}$ film at 500x magnification

As can be seen, darker drops or spots 2-10 µm in size, are present within a light matrix. These drops were found to be C-based (probably PMMA) while the matrix was found be almost C-free ($As_{42}S_{58}$), which likely indicates that the polymer separated from the solution during spinning and evaporation of the solvent. Similar phase separation was observed for all $As_{42}S_{58}$/PMMA films.

In order to find a more stable co-solution, polymers were investigated which contained N-H bonds, as it was found that these molecules were good solvents for the glass. Polyallylamine (PAA) was chosen as a starting point in this case because of the simple structure of the repeat unit $[-CH_2-CH(CH_2NH_2)-]_n$ which is similar to PA ($CH_3-CH_2-CH_2-NH_2$) and EDA ($H_2N-CH_2-CH_2-NH_2$). It was found that PAA (M.W. = 50,000) was soluble in ethanolamine and that $As_{42}S_{58}$/PAA co-solutions were stable for periods of at least 1 year (if protected for air/moisture). Solutions in this system were derived as explained above using solutions of 20mg/mL PAA in ETA and 200mg/ml $As_{42}S_{58}$; with

the exception that simple mixing of two solutions at room temperature was found to be sufficient to achieve a stable co-solution.

SEM micrographs for 2 films with 5 and 50% (V/V) polymer loading are shown in Figure 5.2 below.

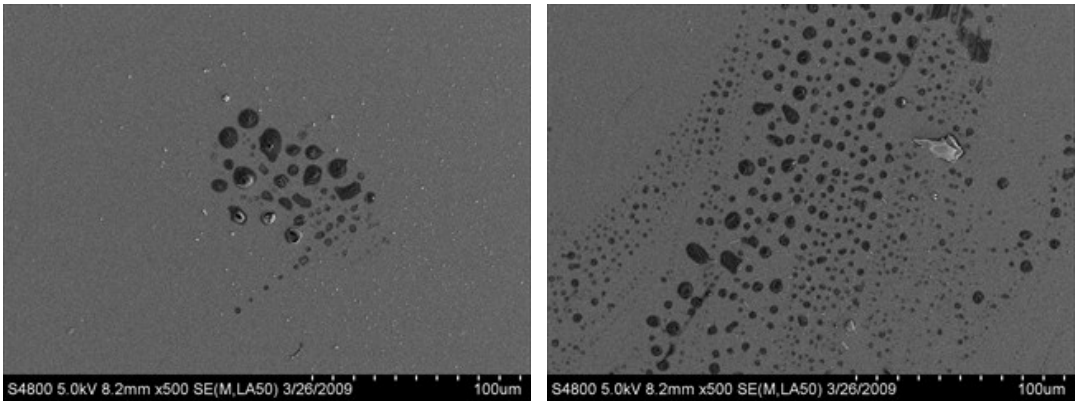

Figure 5.2: SEM micrograph ETA-derived 5% and 50% (V/V) $As_{42}S_{58}$/PAA films at 500x magnification.

As with the PMMA films described above, the PAA films show 1-20 µm dark drops within a matrix indicating a phase separation of the polymer from the glass. It should be noted however, that in the 95/5 film the drops only account for ~1% of the total area of the film, while in the 50/50 film the drops accounted for only 10-15% of the film, and the matrix was found to be completely homogeneous. This suggests that the matrix may contain a significant quantity of polymer. Additionally, the polymer regions were found to react to the electron beam, even at relatively low acceleration (5kV) necessitating short exposures. Despite the presence of some phase separation in the $As_{42}S_{58}$/PAA films, they nonetheless appeared to be transparent. Figure 5.3 below displays the transmissions spectra of 95/5 and 50/50 $As_{42}S_{58}$/PAA films.

`

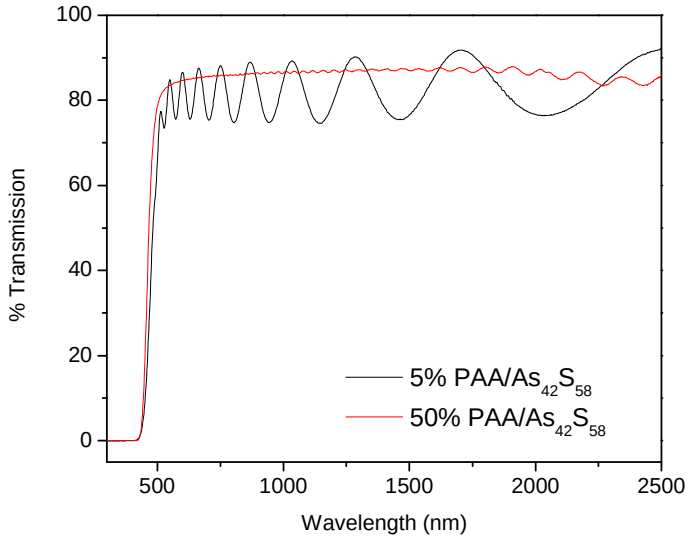

Figure 5.3: Transmission spectra of ETA-derived 5% and 50% (V/V) PAA/$As_{42}S_{58}$ films.

The spectrum of both films display a maximum transmission of 88-90%, however the fringe height and spacing of the 50% polymer film is significantly smaller. This is attributed to the larger thickness and non-uniformity in this film. The thickness the 5% and 50% films was found to be 2 and 20 µm respectively using interferometric microscopy, the thickness difference being attributed to the higher viscosity of the higher polymer containing solution. The value of the transmission maxima in the films, is predicted to be approximately equal to that of the uncoated substrate [108] (given insignificant scattering). The transmission of the substrate may be estimated using the refractive index of the substrate (1.54) using the Fresnel equation for normal incidence (equations 2.5 and 2.6) as 91%. Thus, there is only a 1-3% loss of transmission induced by the film showing that, despite the minor phase separation noted using SEM, the films are largely free of scattering.

`

A third polymer, polyacrylamide (PAM) was also found to produce stable co-solutions with $As_{42}S_{58}$ when dissolved in ethanolamine. SEM micrographs of films derived from PAM/$As_{42}S_{58}$ co-solutions in ETA, prepared as described above for PAA/$As_{42}S_{58}$ films, are shown in the figure below.

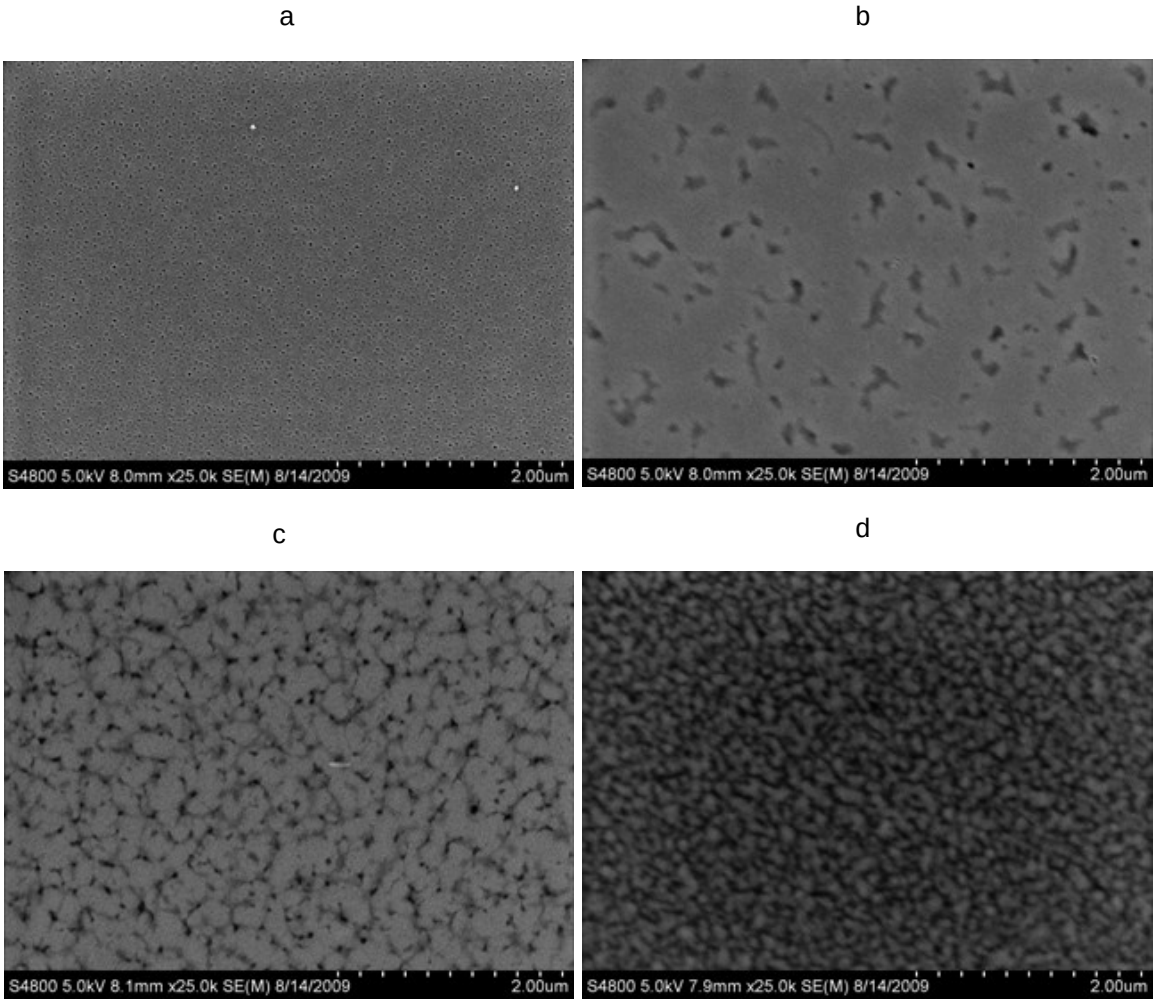

Figure 5.4: SEM micrographs of PAM/$As_{42}S_{58}$ hybrid films with 0% (a), 5% (b), 20% (c), and 50% (d) PAM by volume at 25,000x magnification

One can see from the figure, that the polymer-free film displays porosity on the scale of ~50nm, as described in the previous chapter. With the incorporation of polymer, the morphology of the films and microstructure becomes larger. It is important to note that these images were acquired at significantly higher magnification (25,000x) that those of the PMMA and PAA films (500x) shown above. The structure of PAM films appears completely homogenous at lower magnifications. At vol. 5% PAM loading, larger structures are observed (200-300 nm). These structures appear darker than the surrounding material, and appear to be porosity, as will the polymer-free films; however it may also be that the films are phase separated below the surface, which leads to this surface non-uniformity. As the polymer content increase from 5-50%, the size of the non-uniformities decreases slightly and their relative area increases. The size is the most important factor in this case, because inhomogeneity or phase separation over length scales below one quarter of the wavelength is not expected to induce strong scattering, and these features are well below the needed size for IR applications.

AFM 10µm and 1µm size surface topography images for hybrid films with 5% and 10% polymer content heat treated at 150 °C are shown in figure 5.5 below.

`

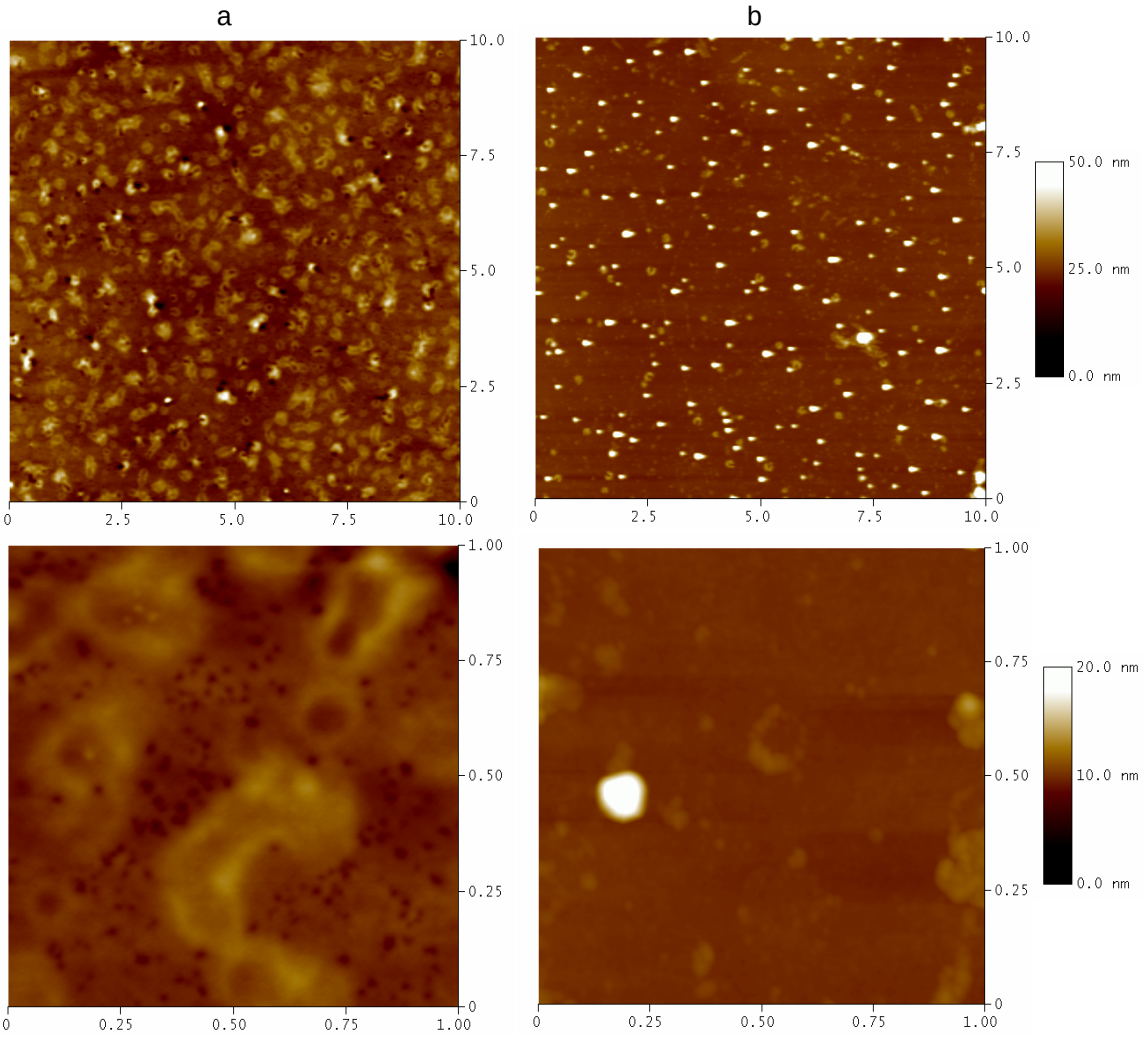

Figure 5.5: AFM surface topography images of 5% (a) and 10% (b) PAM/$As_{42}S_{58}$ hybrid films heat treated at 150 °C.

The AFM scans confirm the existence of phase separation suggested in SEM observations. As the polymer content increases from 5% to 10% a number of small (50nm-100nm) roughly spherical particles can be seen in the surface of the film. It is unknown whether these form only at the surface of the film or are present throughout the

`

thickness. 10µm x 10µm and 1µm x 1µm AFM surface topography images for hybrid films with 20% and 50% polymer loadings are shown in Figure 5.6.

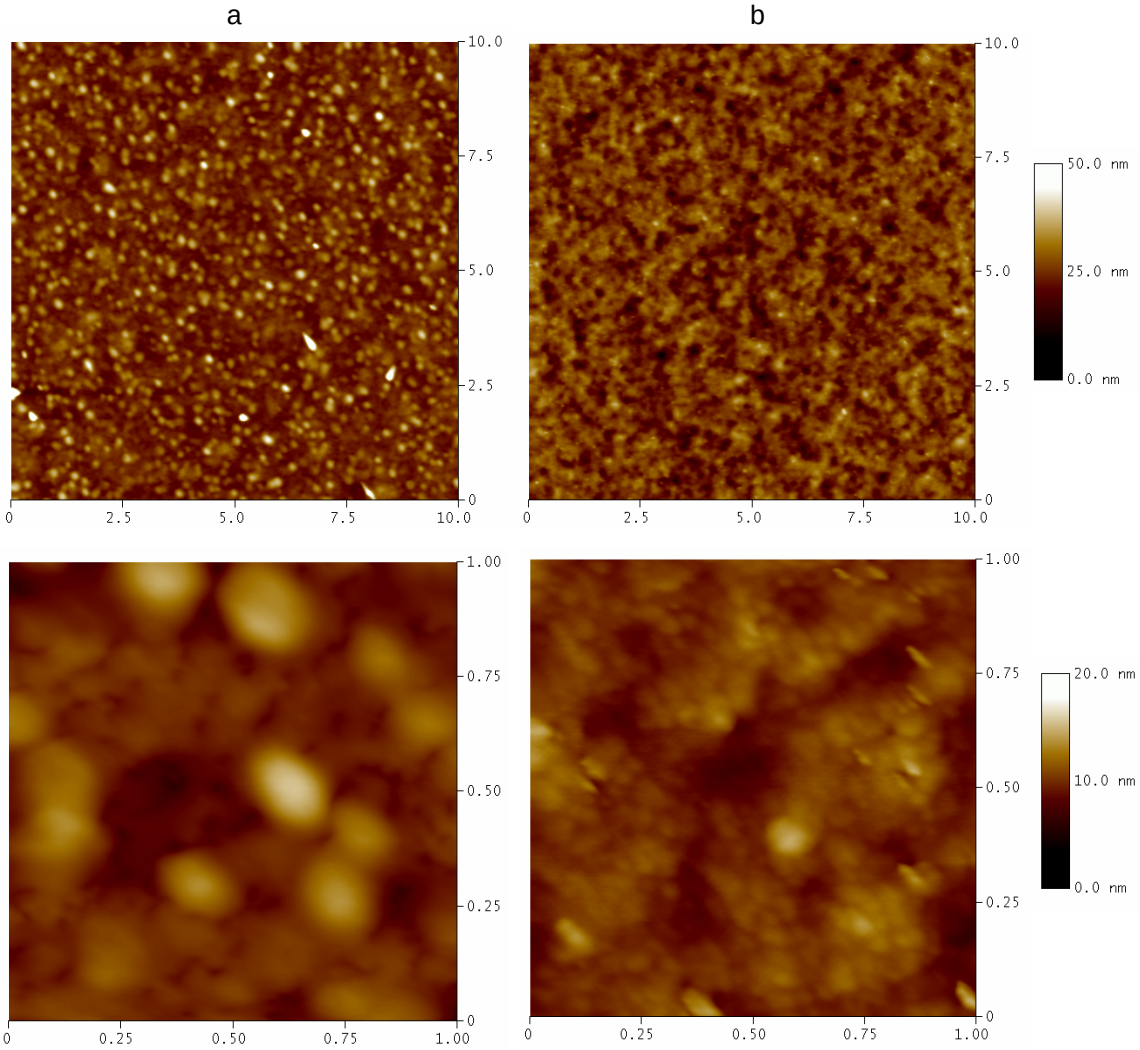

Figure 5.6: AFM surface topography images of 20% (a) and 50% (b) PAM/$As_{42}S_{58}$ hybrid films heat treated at 150 °C.

As the polymer content continuous to increase from 10 to 20%, the number of 20-50nm inclusions also continues to increase. Based on this trend and that approximately 10 and 20% of the image area is covered by these particle for 10% and 20% polymer films, this

suggests that the particles account for the majority of the polymer present in the films. At 50% polymer loading, these particles are no longer seen, and the film appears to be smooth and uniform. At high resolutions, the film appears to be comprised of small, 5-10 nm domains, possibly particles, but no appearance of separate phases is seen. For all of the studied films, the size of the structures observed using AFM are well below the critical dimension (~250 nm) for scattering at wavelengths longer than 1µm. This confirms that the films are homogeneous over optically important length scales, and may be expected to be transparent for use in devices in the near infrared and beyond (longer wavelengths).

One significant difference in this system is the large molecular weight of the polymer (1,000,000) compared with the previous systems. Because of the high molecular weight of this polymer, relatively low concentrations were necessary as concentration above 30mg/ml were found to form solid gels, and co-solutions. Stress-strain curves obtained using a Brookfield (model DV-III Ultra) Viscometer for PAM-ETA solutions of varying concentration are shown in figure 5.7 below.

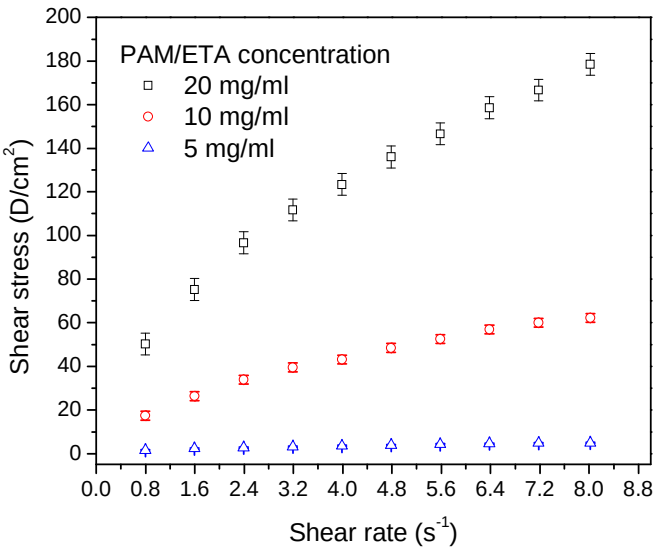

Figure 5.7: Shear stress-shear strain viscosity plots for PAM-ETA solutions.

It can be seen from the figure that the stress does not vary linearly with the shear rate, which indicates that the viscosity of the polymer solutions in non-Newtonian. As this can have a significant impact on the optimization of spin-coating parameters [176, 177], the data was fit using a generalized power law [178] of the form:

$$\tau = K\gamma^n \tag{5.3}$$

Where τ is the sear stress, γ is the shear rate, K is a pre-exponential factor, and n is the dimensionality constant. In order to determine the value of n, log-log plots were fit by linear regression. This is shown in Figure 5.8 below.

`

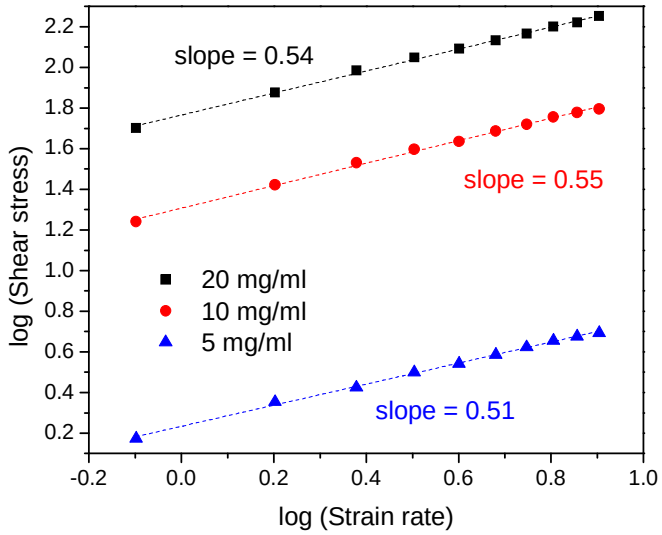

Figure 5.8: log-log plot of shear stress versus strain rate in PAM-ETA solutions.

The slope of the log-log plots for all three solutions is found to be ~0.5, showing that the shear stress increases with square root of the strain rate. Values of n less than one indicate that the fluid displays shear thinning, or a decrease of the viscosity with increasing strain rate. This phenomenon is commonly observed in polymer and sol-gel solutions where the solution contains relatively monodisperse spherical particles which are not entangled or cross-linked [169, 179]. It was found that the spin-coating of these solutions showed a higher tendency toward "fingering", or uneven spreading of the liquid front at the start of spinning [177]. By ensuring complete coverage of the solution on the substrate, the moving solvent front is eliminated and polymer-containing films can be deposited with uniformity similar to the polymer free films of the previous section. Finally, it should be also noted that the solutions showed clear viscoelastic behavior. As droplets are thrown out from outer edge of the substrate during spinning, filaments are formed. These

`

filaments tend to break and then fall back over surface of the spinning film, which leads to very large surface non-uniformities. Maintaining a minimum spin speed of 3000 rpm was found to prevent this behavior.

In order to prevent large variations in the viscosity of the solutions, requiring significant effort to optimize the coating conditions for films with different polymer loadings, the glass-polymer ratio was controlled by combining different volumes on stock solutions of glass and polymer with high concentrations, and diluting to the required volume with pure solvent. The table below shows a matrix of solution compositions used to achieve varying polymer/glass ratios with approximately constant viscosity used in this study. The densities of $As_{42}S_{58}$ and polyacrylamide are 3.20 and 1.17, and the stock solution concentrations were 200 and 20 mg/ml respectively.

Table 5.1: Matrix of glass-polymer solutions for spin coating at constant viscosity, and respective total solids content in volume %.

Polymer loading (Vol. %)	**Stock solution volume (ml)**			**Solids content** (Vol. %)
	Glass	Polymer	Solvent	
0	16	0	4	5.0
5	12	3	5	4.0
10	8	4	8	2.8
20	6	7	7	2.5
33	4	9	7	2.0
50	2	9	9	1.4

All of the above 20mL total volume solutions were found to have viscosities in the rage of 150-200 cP, which allowed spin-coating of films with RMS surface roughness below 5 nm using the optimized parameters for ETA-derived ChG films discussed in the previous

chapter. Figure 5.9 presents the UV-Vis transmission spectra of PAM/$As_{42}S_{58}$ hybrid films.

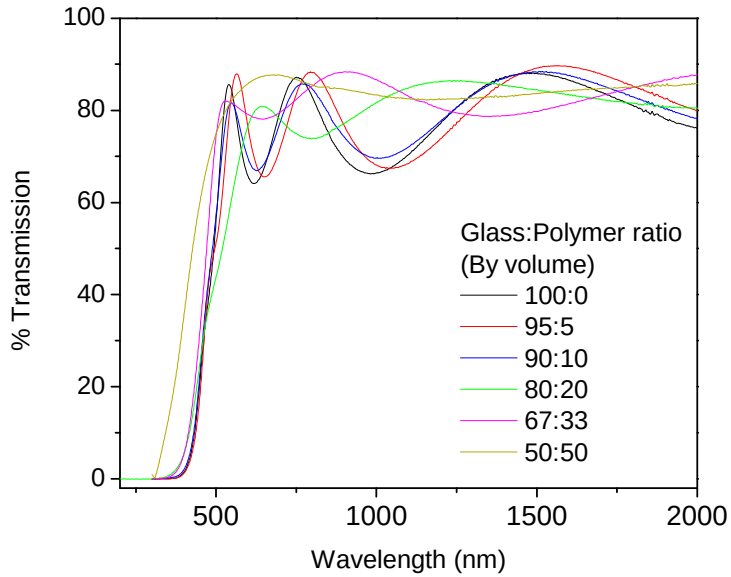

Figure 5.9: Transmission spectra of PAM/$As_{42}S_{58}$ films coated at 3000 rpm for 5 seconds with varying solvent ratio.

In the figure, it can be seen that the fringe strength decreases and fringe spacing increases with increasing polymer content. This may be attributed to decreases of the refractive index and thickness of the films with high polymer loadings. It may also be noted that transmission maxima of ~90% are again seen for the films, which indicates low scattering and confirms the high homogeneity over optically important length scales, as noted form SEM observations. Refractive index was measured using prism coupling at 633 nm, and the thickness and surface roughness were verified using interferometric microscopy, and are shown in Figure 5.10.

`

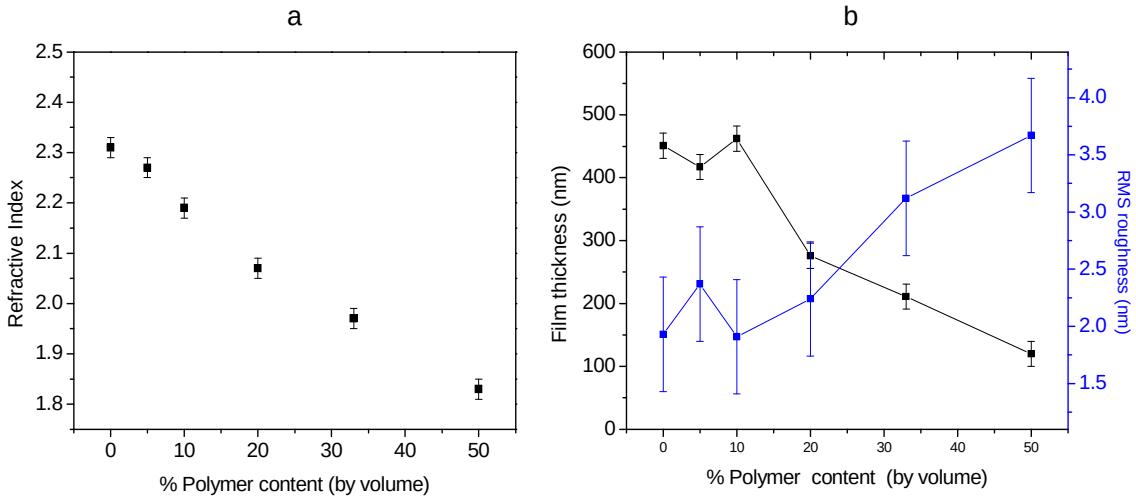

Figure 5.10: Refractive index (a) and thickness and RMS surface roughness (b) of PAM/$As_{42}S_{58}$ hybrid films.

As noted from the transmission spectra, the refractive index and thickness decreases with increasing polymer content. The refractive index follows the well-known "lever rule", varying between the index of the bulk glass (2.3) and the polymer (1.7) as a weighted average based on the volume fractions of each in the film. The surface roughness was also observed to increase slightly for films with high polymer loadings, but was acceptably low (<5 nm) in all of the PAM/$As_{42}S_{58}$ hybrid films. The decrease of thickness with high polymer concentrations is attributed to a decrease in the total volume of solids in the solution, summarized in table 5.1, which was necessitated by the need to maintain viscosity through dilution. It was noted that, unlike the polymer free solutions, the films were not completely re-dissolved by application of additional solution when attempting to deposit multi-layer films. This provides the opportunity to achieve greater thicknesses through sequential depositions. Figure 5.11 below shows the film thickness as a function of the number of layers deposited for ETA-PAM/$As_{42}S_{58}$ films with varying

polymer content. In all cases a 5 minute soft-bake at 90 °C on a hot plate was used after each deposition (between layers) in order to solidify the film.

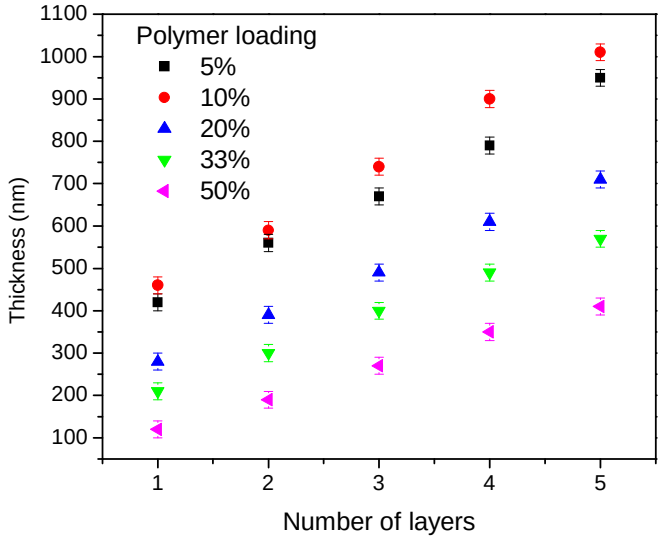

Figure 5.11: Thickness versus number of depositions for multilayer ETA-PAM/$AS_{42}S_{58}$ hybrid films.

It is clear from the figure that the thickness of these films increases with additional layers. While the thickness of the first layer varies, as described above, the rate of increase is relatively uniform for all 5 polymer loadings. This is attributed to a lower re-dissolution rate with greater polymer content. Thus, while the amount of additional material is lower for solutions with large polymer loadings (the amount of material removed from lower layers is also reduced) leading to less variation in the rate of thickness increase. The interplay between re-dissolution amounts and layer thickness, also leads to a slightly faster thickness increase for 10% PAM films as compared to 5% PAM films. This is a promising result for the potential application of these materials where thicknesses in the range of 500-1000 nm are required.

`

Because the addition of polymer to the film is expected to induce IR absorption, the IR transmission of hybrid films was investigated. The FTIR transmission spectrum of a 50% PAM/$As_{42}S_{58}$ film before and after hard bake is shown in figure 5.12 below.

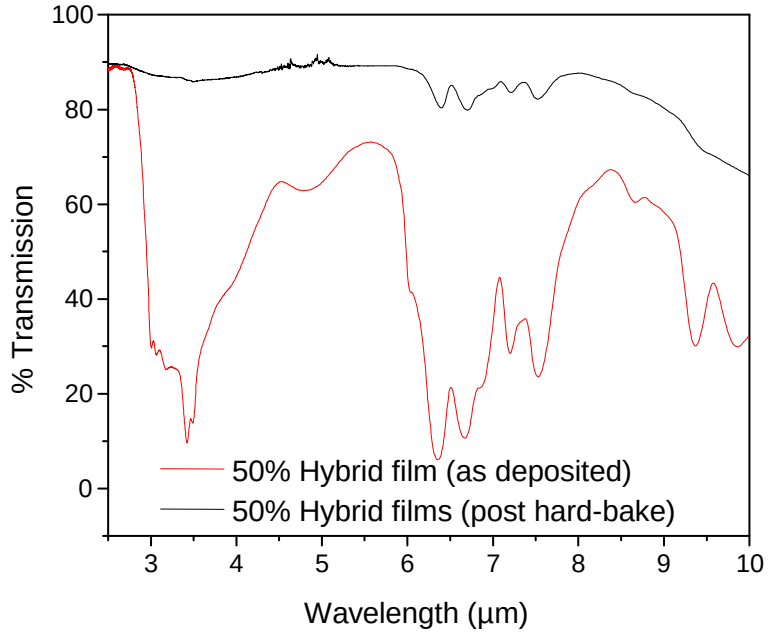

Figure 5.12: FTIR transmission spectrum of 50 vol. % PAM/$As_{42}S_{58}$ hybrid film before and after hard-bake.

From the figure, it is clear that absorption features, related to the organic are present in the spectrum of the film both before and after hard-bake, however, the absorption from the organic components near 3.5 and 6.5 and 9.5 µm are greatly reduced after treatment, probably due to the removal of residual solvent. As noted in Chapter 4, the N-H stretch near 3.5 µm is more strongly reduced as compared to the other bands. This corresponds to elimination of N-H bonds, possibly through the evolution of a small amount of H_2S gas during heat treatment. While the IR transparency is of hybrid films is reduced (as

expected) regions of higher transparency may be observed in near 5-6 and 8 µm. It may possible through the tailoring of the polymer system and glass/polymer loading levels, that these transparent regions may be selected to correspond to the particular wavelength of interest for certain applications. Additionally, it was observed for glass-only films, that an N-H bond is needed for the dissolution of the glass, but may it not be needed in the polymer to stabilize the hybrid film, as the lone pair of a tertiary N atom may still be donated to form a ligand bond. This suggests the polymer containing N atoms, but not as amide or amines may be possible as substitute polymer systems, allowing the removal of N-H and its associated absorption near 3 µm. Finally, it is also propose the dissolution of the polymer from the film after deposition and heat treatment. While PAM is soluble in water, the glass in insoluble when pH < 10. At this film is phase separated, the use of appropriate aqueous or solvent treatments may allow the stripping of the polymer phase. The created voids may either be left to produce a porous glass film, or a second polymer may then be back-filled into the void space to produce glass-polymer composites, but without a change in the microstructure, making these new glass-polymer hybrids also transparent. A full investigation of the potential glass-polymer systems which are available using these additional techniques is beyond the scope of this work, but serves to highlight potential for application of solvent-based process for novel ChG-based materials with high transparency.

5.2 Novel deposition and fabrication techniques

While spin-coating was used for all of the films demonstrated to this point, there is no particular reason to limit the investigation to this one technique. Many other deposition methods have been developed for solution processing, and any of these is potentially applicable. Dip-coating [180, 181] may be the most widely used technique for solution-processing outside of lithographic applications and, along with capillary coating [182], allows highly efficient use of the solution with minimal waste. Spray coating [183] and spray pyrolysis [184] are alternate methods which can be applied both to fine powders and to solutions, and have the advantage of being able to coat large areas and surfaces with complex geometries.

It is also possible to use certain techniques to directly pattern devices in a single step. The most common of these are screen-printing techniques [185] and ink-jet printing methods [186, 187]. However, these give devices with relatively large geometries, and may not provide devices with adequately precise geometries for low-loss optical applications [187]. Two additional methods, micro-stamping (micro-contact printing) [188] and capillary force lithography [189] may provide a route to direct fabrication and high resolution uniform device geometries. In micro-stamping, a piece of elastomeric material, typically PDMS, is patterned and coated with the solution. This is then carefully applied to the substrate, and the pattern is transferred. This is demonstrated in the following figure.

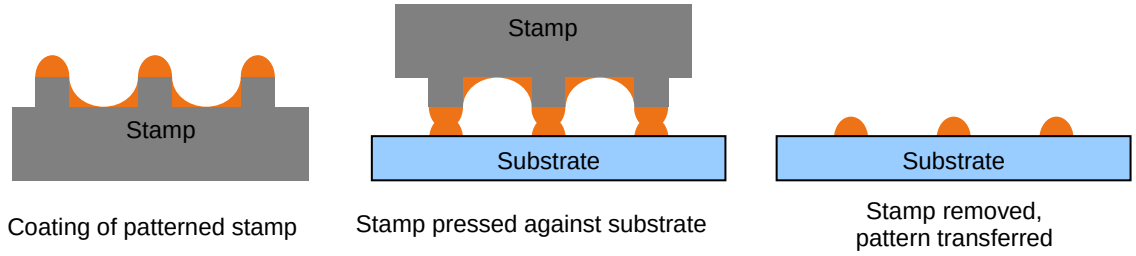

Figure 5.13: Schematic for PDMS micro-stamping process

Unfortunately, for this application good wetting of the solution both on the PDMS stamp and on the substrate are required and the ChG solutions studied were not found to adequately wet to PDMS material even after plasma etching. Therefore, the alternate capillary force lithography (CFL) technique was examined, as it requires wetting only to the substrate. This process is depicted in the following figure.

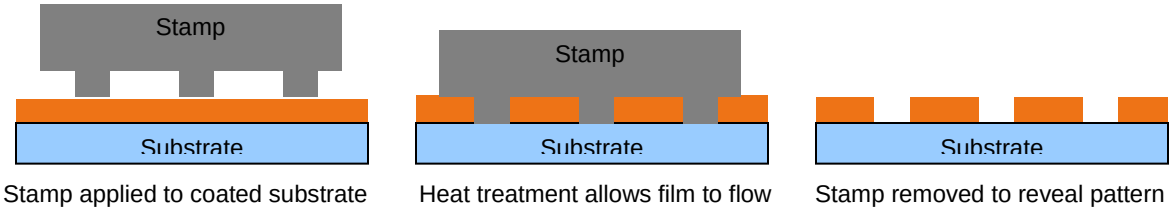

Figure 5.14: Process flow for capillary force lithography (CFL)

In this process, the stamp is placed in contact with a coated film and the film is then heat treated in order to allow the film to flow. As flow begins, capillary force causes flow of material into cavities in the pattern of the stamp. The film is then allowed to cool and re-solidify before the stamp is removed, leading the negative imprint of the stamp pattern on the film.

As a proof-of-concept test, a stamp was created by polymerizing a layer of PDMS over a compact disk (CD), to yield a grating pattern with a period of ~2 µm and a height of 200nm. Then, a 500 nm thick ETA-derived $As_{42}S_{58}$ film was deposited and the

`

standard soft and hard-bake treatments performed. Finally, a small section of the CD mask was placed on the film and both were heat treated together for 30 minutes at 210 °C, corresponding to the T_g of the bulk glass. After heat treatment, the film was allowed to cool to room temperature and the mask was peeled off. The resulting grating effect was clearly visible on the sample surface. An AFM scan of the CFL grating is shown in figure 5.15 below.

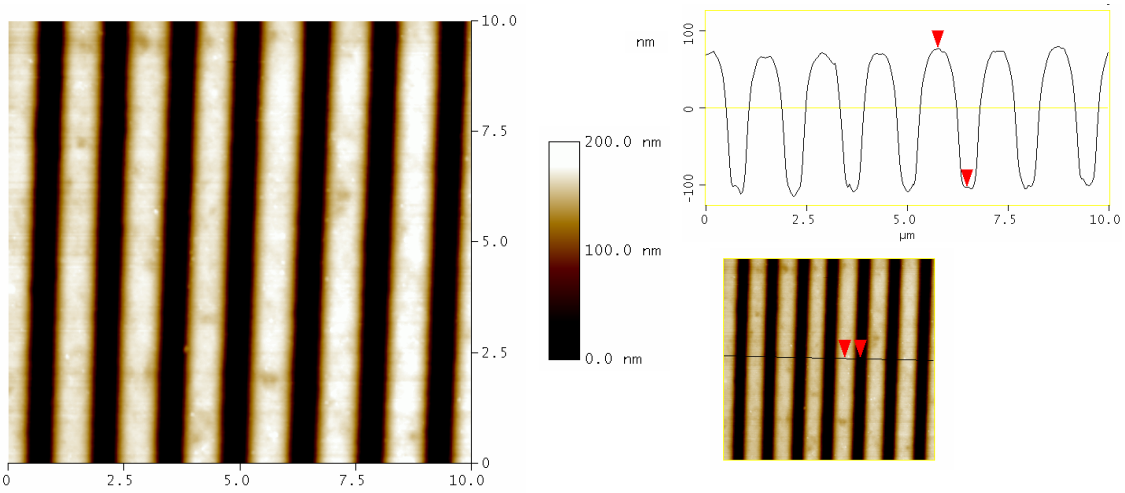

Figure 5.15: AFM surface topography images for CFL gratings in ETA-derived $As_{42}S_{58}$ film fabricated at 210 °C

From the figure, it is clear that the grating pattern was replicated in the surface of the film. It can also be seen that the top of the gratings appears to be relatively rough. A higher resolution scan of the grating surface is shown in the figure below.

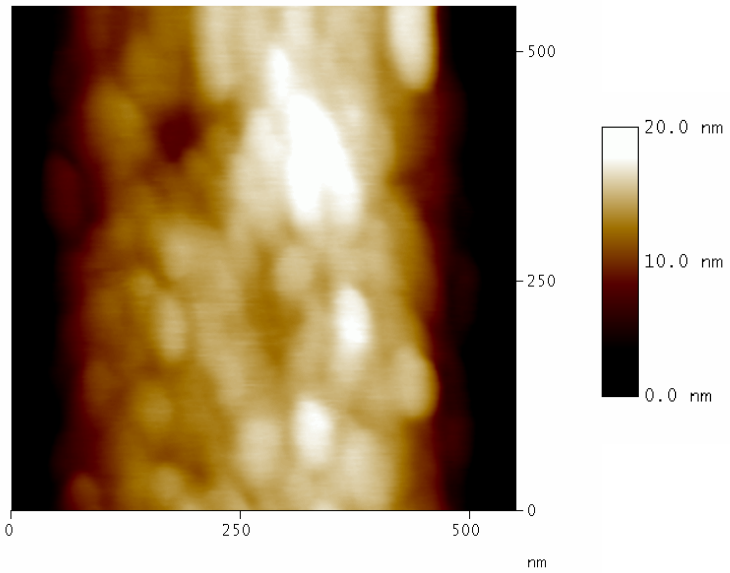

Figure 5.16: High resolution AFM topography scan of $As_{42}S_{58}$ grating surface produced at 210 °C

In this figure the increase of surface roughness is clearer. The RMS roughness of the top surface was found to be ~27 nm, significantly higher than in the pre-treatment film (~2 nm). As described in Chapter 4, this is attributed to partial crystallization of realgar (As_4S_4) from the film. For application of CFL in the fabrication waveguide devices, a roughness below 5 nm is needed to minimize optical loss through scattering. In order to overcome the problem of crystallization, two additional schemes were investigated.

By moving the CFL treatment to an earlier step in the procedure, it may be possible to take further advantage of the solution phase. Prior to the hard-bake treatment, significant amounts of solvent are still present within the film (as shown in chapter 4), allowing the material to flow under capillary force at lower temperatures. For this reason, the effect of performing the CFL step either during the soft bake or hard bake steps has also been investigate. Figure 5.17 below presents the AFM surface scans of CFL gratings

`

created either by placing the stamp onto the surface immediately before the soft-bake at 90 °C (a), or immediately before the start of the hard-bake at 150 °C (b).

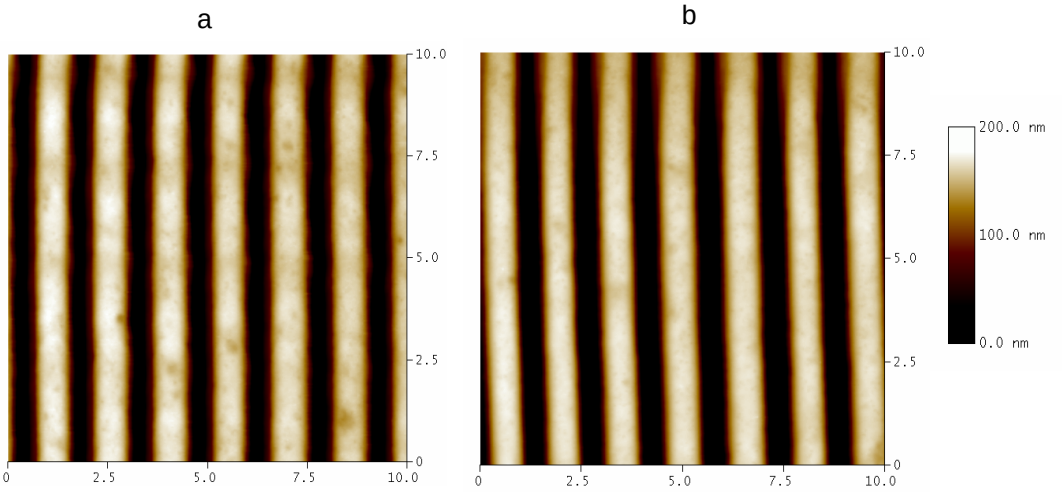

Figure 5.17: AFM scans of CFL gratings formed during soft-bake (a) and hard-bake (b) of ETA-derived $As_{42}S_{58}$ films.

One can see that both procedures produce grating structures similar to that obtained from the high temperature heat treatment shown in Figure 5.15. High resolution scans of the grating surfaces are shown in figure 5.18.

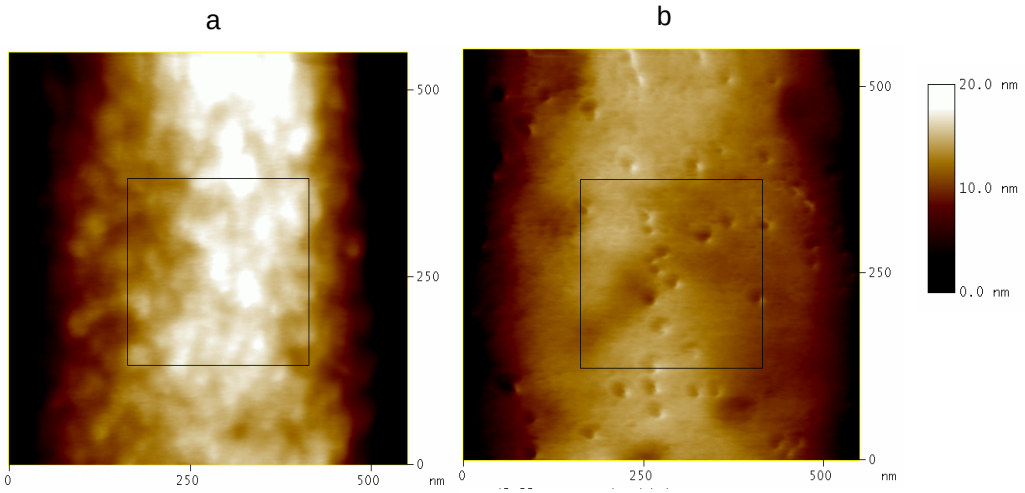

Figure 5.18: AFM scans of CFL gratings surfaces formed during soft-bake (a) and hard-bake (b) of ETA-derived $As_{42}S_{58}$ films.

`

It can be seen that both procedures offer improved surface roughness compared to the high temperature treatment, in fact the RMS roughness was found to decrease to 1.3 and 0.9 nm for soft-bake and hard-bake CFL respectively. Due to the fact that the ETA-derived film is still a liquid immediately after spinning, we believe soft-bake CFL this will allow the greatest flexibility in terms of the size of structures which can be fabricated using the CFL technique, while performing CFL during hard-bake appears to give more uniform and lower roughness structures. These methods may be applied for the fabrication of ridge waveguides and resonator structures, and may provide a simple and direct route to the fabrication of integrated planar optical devices for operation in the near- and mid-IR.

5.4 Waveguide over-cladding

We have previously shown that the optical loss in waveguide systems fabricated using lift-off photolithography is dominated by scattering induced by surface roughness [70]. Moreover, it is possible to reduce the loss of such systems either by decreasing the surface roughness using thermal reflow [190] or by including a graded index (GRIN) coating over the guide which reduces the index mismatch at the surface [191]. As shown in previous section in this chapter, solution-based processing both allows the tailoring of refractive index over a broad range, and provides surfaces with low roughness. We therefore propose that using spin-coating to create waveguide over-cladding layers may serve both roles, and allow significant improvement of optical loss values.

The waveguide over-cladding process in summarized in the following figure.

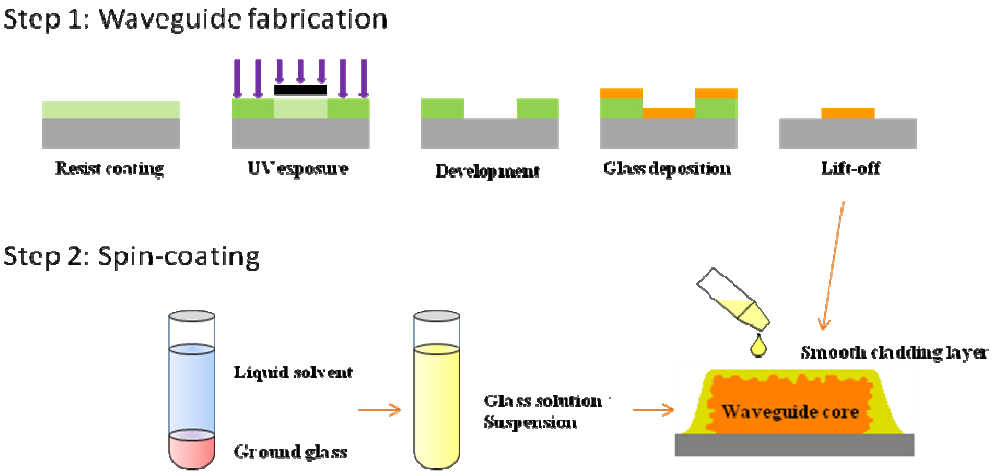

Figure 5.19: Process flow for solution over-cladding of lift-off fabricated waveguides

In this process, the waveguides are first prepared from thermally evaporated film, and then a solution of either the same or a different glass composition is coated onto them by spin coating. Dip-coating may alternately be used, and could possibly provide better coating uniformity, through matching the withdrawal direction with the propagation direction of the guides. The final coated waveguides are then annealed using the optimized soft-bake/hard-bake procedure outlined in the chapter 4.

Figure 5.20 presents SEM micrographs for cross-sectioned (cleaved) $Ge_{23}Sb_7S_{70}$ waveguides before and after over-cladding with an additional layer of $Ge_{23}Sb_7S_{70}$ using the process described above. The over-cladding was performed using 25mg/mL solution prepared in propylamine, due it its lower dissolution rate, which may be expected to minimize the potential for dissolution of the thermally evaporated material. Spin-coating was performed at 9000rpm, in order to minimize the over-cladding layer thickness.

`

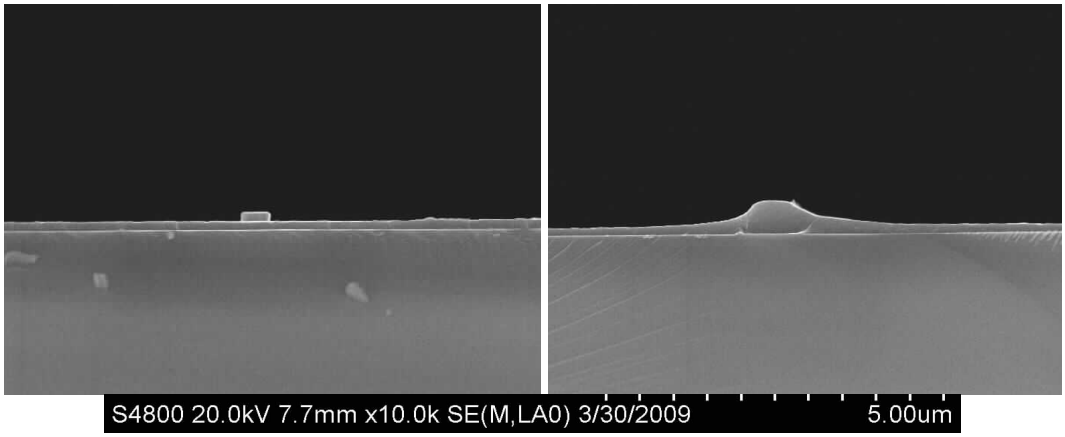

Figure 5.20: SEM cross-section of 200nm thick waveguide before (a) and after (b) over-cladding.

From the image one can observe that the as-fabricated waveguide (left) has a rectangular shape, and is approximately 500 (±10) nm in width and 200 (±10) nm in height, while the coated waveguide has a width of ~1000nm and a slightly greater height (400 (±10) nm). This change in geometry does not represent a major drawback to the use of this process, but would need to be accounted for in the design of the lift-off pattern if, for instance, single mode operation were required. It should also be noted that the core of the waveguides did not separate from the cladding as the sample was cleaved, indicating good adhesion between the two layers. Energy dispersive X-Ray spectroscopy (EDS) was used during imaging to verify the composition of the film, which was found to be identical to that of the parent bulk glass, within the error of the measurement (±2 at%). Unfortunately, due to the small size of the features, it was not possible perform any mapping of the composition across the cross-section, however, the lack of contrast between the core and clad suggested a good match in chemistry.

In order to examine the effects of spin-coating on the roughness of the waveguide, AFM images of the waveguide surface were collected before and after coating. In Figure

5.21 below is shown a surface profile for a 5 μm long waveguide section before and after coating.

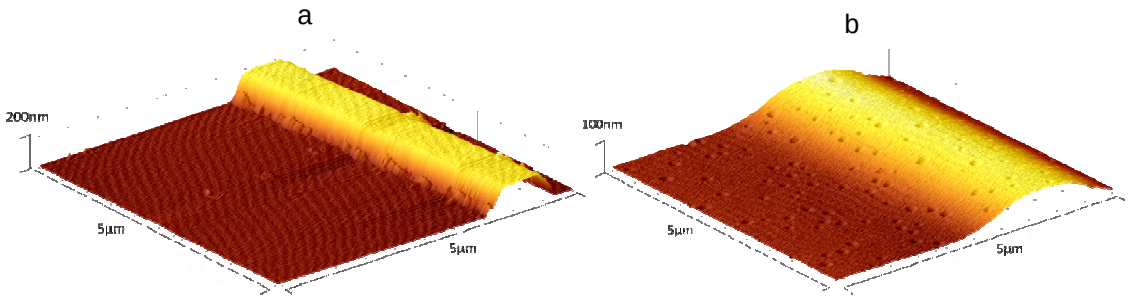

Figure 5.21: AFM profile of 200nm thick waveguide before (a) and after (b) over-cladding.

One can see a similar 500nm width and 200nm height for the uncoated guide, as observed in the SEM images. Additionally, a significant amount of roughness is visible on the sidewalls of the waveguide. After coating, the waveguide profile becomes more curved, and the width is significantly increased. There is also a decrease in the apparent height of the waveguide (100 nm), though based on the observation of the waveguide height in Figure 5.20, this is likely only due to the wide tapered wings created during spin coating. Shown in figure 5.22 is a typical plot of height vs. distance along the line-scan on the side of the waveguide before and after coating.

`

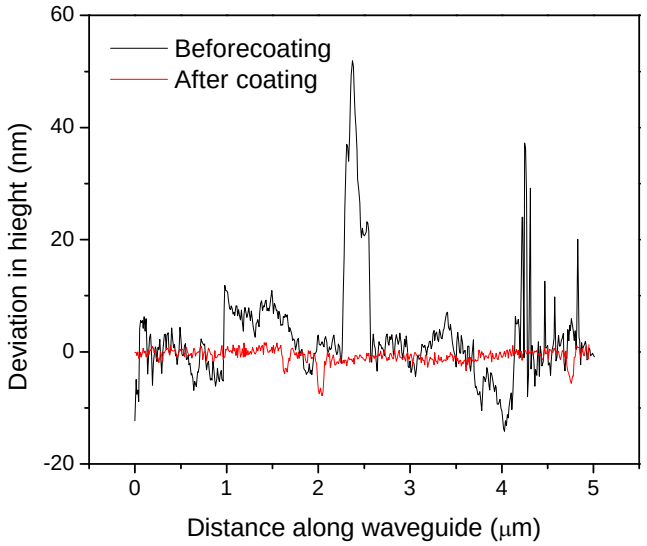

Figure 5.22: AFM line-scans of waveguide sidewalls before and after coating.

The line scans were taken at ½ of the total height of the waveguide above the background. Fewer significant peaks and valleys are found for the scan after coating as compared to before, and those that are present have much smaller amplitude. Average RMS roughness values were found to decrease from 19 (±2) nm for the as-fabricated waveguides, to 1.4 (±0.1) nm for the coated guides. The larger error in the value before coating is due to the higher variability between different waveguides (three waveguides were scanned for each sample).

In order to examine the influence of the coating parameters on waveguide loss, the optical loss of guides coated at varying spin-rates (varying cladding layer thickness), at heat treated at different temperatures, was measured. Optical loss measurements at a wavelength of 1550 nm were performed in collaboration with the Microphotonics Center

at MIT, using a cut-back based method, outlined in a previous publication [191]. Figure 5.23 presents the optical loss for waveguides before and after over-cladding.

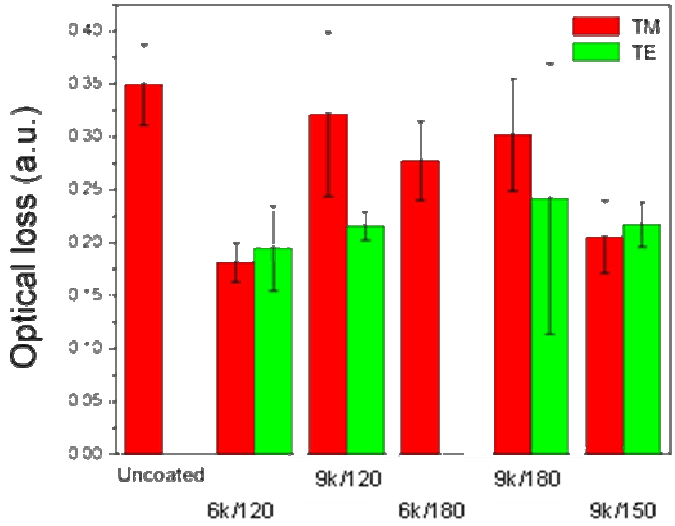

Figure 5.23: Optical loss at 1550 nm for coated waveguides as a function of spin-speed and hard-bake temperature (speed/temperature).

Overall, the trend shows that the thickness of the coating has a only a minor effect on the optical loss, with the loss decreasing slightly when the spin-speed increases from 6000 to 9000 rpm, with an estimated decrease of the coating thickness from 250 to 180 nm. The larger effects appear to be due to the temperature of heat treatment, with an increase of the loss with increasing temperature, particularly at 180 °C, which may be attributed to the onset of crystallization with the associated increase in roughness, as outlined in chapter 4. For all coating conditions shown, however the loss of the waveguide is reduced as compared to the uncoated sample, with a maximum loss reduction of approximately 50%. This result is very promising for the future development of low-loss waveguide-based sensor systems, as these experiments are still unoptimized. It is also likely the

coating of lower-index glasses or hybrid coatings over a high-index core, would allow still lower loss values due to the graded-index effect.

5.3 Summary of findings

In this chapter we have demonstrated that solution processing may be used as a route to fabrication of novel chalcogenide glass (ChG)-polymer hybrid materials. We have shown that:

1) Polymers containing N-H bonds act as good candidates for forming stable ChG-polymer co-solutions. Films formed from the glass $As_{42}S_{58}$ with polyallylamine (PAA) and polyacrylamide (PAM) in ethanolamine (ETA) solutions were found to exhibit a small degree of phase separation, and were found to possess high transparency in the visible and near-IR.

2) PAM /$As_{42}S_{58}$ films were found to be particularly promising for IR optical applications due to the small size of the phase separated regions (< 250 nm), and the refractive index of these films was found to vary over a wide range (1.7 - 2.3) in accordance with the well-known lever rule.

3) IR transparency of the hybrid system is reduced compared to glass-only films; however significant transmission was observed near 5-6 and 8 µm wavelengths. Further substitution of the polymer system, either within the solution or post-deposition by stripping and back-filling of the polymer phase may allow the

possible expansion of these hybrid material systems and expansion of the transparent regions.

4) ETA-derived ChG films were demonstrated to be well suited for the fabrication of planar optical structures using the capillary force lithography (CFL) technique. PDMS masks derived from compact disks were shown, as a proof-of-concept demonstration, to allow the fabrication of ~2 μm period gratings in $As_{42}S_{58}$ films. By combining the CFL step with the post-spin heat treatment procedure, surface roughness of the CFL-derived structures was found to be reduced. These results are promising for the future application of this technique for the fabrication of ChG thin film devices in a single step.

5) The over-cladding of lift-off fabricated waveguides was shown the both allow for reduction of surface roughness, and the decrease of optical loss. By tailoring the refractive index of the over-cladding layer, either though changing the glass composition or by using hybrid coatings, a graded index effect may also be created which is expected to further decrease the optical loss. This technique is promising for the improvement of sensitivity and detection limits in waveguide-based optical sensor systems.

CONCLUSIONS

In this work, we have demonstrated the use of solution-based processing techniques for the fabrication of chalcogenide glass and glass-polymer hybrid thin film and structures. Bulk glasses in the As-Ge-Sb-S system were prepared and characterized. These glasses were shown to have high IR transparency and linear and nonlinear refractive indices. The physical, thermal, and optical properties of the glass were related the molecular structure of the glass network, and was found to be influence primary by the density of lone electron pairs, and the average coordination of bond strength of the various network units. Assessment of bond statistics, derived from Raman spectra, and the associated bond energies and lone electron pair densities, was developed and used as a predictive tool to estimate linear and nonlinear optical properties, glass transition temperatures and microhardness in the investigated glass system.

Bulk glasses were shown to be resistant to acid solutions, unless highly oxidizing, but were susceptible to attack in high pH aqueous solution, and inorganic amines. The dissolution was found to proceed through a first order nucleophillic attack of the N atom in the amine group, resulting in aminolysis and the sulfide network, and the dissolved glass species were found to vary depending on the metallic species involved (As, Ge or Sb). Dissolution kinetics were found to be consistent with an interpretation based on the Pearson hard-soft acid base concept, and is controlled by stabilization of reaction products by the solvent.

Subsequent spin-coating of the amine solution was shown to allow the formation of this films and optimization of glass loading depending on specific glass-solvent

combination allowed the formation of thin films with composition identical the bulk glass but with a somewhat different molecular structure, as demonstrated using micro-Raman spectroscopy. Optimization of the deposition conditions allowed the formation of thin films with thickness of 500-1000 nm and RMS surface roughness below 1 nm, which is promising for IR optical sensing applications. It was demonstrated that residual organics may be largely eliminated through sub-T_g vacuum heat treatment.

By incorporating compatible polymers into the glass solution, polymer-glass hybrid films may be deposited which show optical transparency, due to their homogeneity over lengths scales (<200 μm) important for infrared applications. Due the wide range of glass-polymer ratios which may be deposited (100 glass – 100% polymer), the refractive index of the films may be varied over wide range (1.5 to 2.2), making these attractive of IR multilayer coatings. Additionally, a micro-stamping based technique known as capillary force lithography was shown as a promising route to the fabrication of ChG planar optical devices in a single step.

FUTURE WORK

Many opportunities for extending the research exist. In terms of glass science, the composition space examined in this study could be expanded to include sulfide, telluride and mixed-anion systems. Initial results indicate that As_2Se_3 is amenable to this form of processing, but with significantly lower dissolution rates. The cationic glass formers may also be changed. Of particular interest in this case are gallium and indium, which are commonly used both in chalcogenide glasses and in semiconductors. Initial examinations in this area suggest that these elements, which readily form tetrahedral anionic species ($[GaS_4]^-$ and $[InS_4]^-$ respectively) even within the glass network, require the use of highly polar solvent systems such as dimethylsulfoxide (DMSO) or propylene carbonate in addition to the amine to facilitate the stabilization of the dissolution products. The combination of diethylamine and DMSO has shown some promise. An alternate base, tris(dimethylamino)phosphine (HMPT) is particularly interesting as it is a very strong base, is chemically soft and highly polar, and has suitable boiling point (150°C).

The questions of residual solvent concentration in the films and the nature of the solution have both proven difficult to fully address. While the viscosity, and Raman analysis both suggest true solutions are formed, light scattering studies were not able to produce conclusive results, leaving this question still unanswered. One possible way to examine the solutions is through gel-permeation chromatography, where the mobility of the solute through a gel of known porosity can give information regarding its size and/or molecular weight. Electrochemical impedance spectroscopy, may also give information both about the nature of the glass solution and on the question of residual solvent within

the heat treated films. As the frequency-dependent motion of molecules and particles under an AC electrical field is dependant both on size and on polarization, particles would be expected be move more slowly in a solution than molecules, and films with air or nitrogen in their pore space would behave differently if that space was filled with solvent molecules.

Within the topic of hybrid films, most interesting perhaps is expansion of the investigated polymer systems. The choice of amine-based polymers was made only to improve glass-polymer compatibility over PMMA. It may be found other polymers would be acceptable in terms of their phase separation behavior, but with better properties. It is also probable that the inclusion of water-soluble polymers such as PAM in the films will reduce their long-term stability in humid conditions or aqueous environments. This should be investigated in more detail, and it may be found that alternate polymer chemistry may be necessary to provide adequate stability. N-isopropyl polyacrylamide (NIPAM) is known to change its solubility behavior as a function of temperature, becoming water soluble at high temperatures and insoluble at low temperatures, which may allow the preparation of the co-solution at elevated temperatures but with lower moisture sensitivity at room temperature.

Another important issue in relation to the hybrid films is their IR transparency. By replacing PAM with a polysulfone or a fluorinated polymer, the IR transparency may be improved. While the solubility of fluorinated polymers is low in the polar of solvents used to dissolve the glass, it may be possible to leach the polymer phase out of the hybrid films in a third solvent such as ethanol, which does not attack the ChG phase. The

resulting porous film may then be back-filled using a more suitable polymer for IR applications, while retaining the small dimensionality of the PAM phase and remaining transparent.

The novel processing methods discussed in this work, capillary force lithography (CFL), and waveguide over-cladding have both been shown to produce features with low surface roughness. While the optical loss of the over-clad waveguides was shown to be reduced as compared to lift-off waveguides, it was not possible to measure a propagation loss in the CFL grating, as they are designed for use perpendicular to the propagation direction. In order verify whether this technique can be used to produce low-loss waveguides, a suitable mold must first be prepared. Ideally, this would be fabricated by lift-off of a photo-resist rather than ChG or by etching of an oxidized wafer. A PDMS mold prepared from this master, and used in CFL would result in the duplication of the pattern of the master in the ChG film. As a result, any surface roughness on the master would be duplicated in the CFL device, but this would allow many duplicate molds to be prepared at low cost. Furthermore, by using the same pattern as that used to fabricate the lift-off waveguides, both types of waveguide could be directly compared. For the study of waveguide over-cladding, GRIN-type structures should also be examined to determine whether it is possible to further reduce the optical loss by tailoring the refractive index of the cladding layer.

REFERENCES

1. L. Petit, N. Carlie, T. Anderson, J. Choi, M. Richardson, and K. Richardson,"Progress on the Photoresponse of Chalcogenide Glasses and Films to Near-Infrared Femtosecond Laser Irradiation: A Review" *IEEE J. Sel.Topics Quant. Electron.* , **14**(5) 1325-1334 (2008)

2. S.O. Kasap and S. Yannacopoulos,"Kinetics of structural relaxations in the glassy semiconductor a-Se" *J. Mater. Res.*, **4**(4) 892-905 (1989)

3. H.J.M. Hanley, J.C. Rainwater, and M.L. Huber,"Prediction of shear viscosity and non-Newtonian behavior in the soft-sphere liquid " *Int. J. Thermophys.*, **9**(6) 1041-1050 (1988)

4. J.M. Saiter, J. Ledru, A. Hamou, and A. Zumailan,"Dependence of the glass transition temperature on the heating rate and structure of chalcogenide glasses" *Mater. Lett.*, **33** 91-96 (1997)

5. C.T. Moynihan,"Correlation between the Width of the Glass Transition Region and the Temperature Dependence of the Viscosity of High-Tg Glasses" *J. Am. Ceram. Soc.*, **76**(5) 1081-1087 (1993)

6. J. Nishii, S. Morimoto, I. Inagawa, R. Iizuka, T. Yamashita, and T. Yamagis,"Recent advances and trends in chalcogenide glass fiber technology: a review" *J. Non-Cryst. Solids*, **140**(199-208) (1992)

7. C.T. Moynihan, A.J. Easteal, J. Wilder, and J. Tucker,"Dependance of the Glass Transition Temperature on the Heating and Cooling rate" *J. Phys. Chem.* , **78**(28) 2673-2677 (1974)

8. A.E. Aliev, A.A. Zakhidov, and R.H. Baughman,"Chalcogenide Inverted Opal Photonic Crystal as Infrared Pigments" *Int. J. Nanosci.*, **5**(1) 157–172 (2006)

9. H.E. Kondakci, M. Yaman, O. Koylu, A. Dana, and M. Bayindir,"All-chalcogenide glass omnidirectional photonic band gap variable infrared filters" *Appl. Phys. Lett.*, **94**(11) (2009)

10. A. Zakery and S.R. Elliott, *Optical Nonlinearities in Chalcogenide Glasses and their Applications*, in *Springer Series in Optical Sciences*, W.T. Rhodes, Editor. 2007, Springer: Berlin.

11. T. Arai and M. Kikuchi,"Carbon monoxide laser power delivery with an As_2S_3 infrared glass fiber" *Appl. Opt.*, **23**(17) 3017-3019 (1984)

`

12. A.R.H. Sr., A.R.H. Jr., J. McCord, and T.J. Loretz,"Laser-power delivery using chalcogenide glass fibers *" Proc. SPIE*, **2977** 20-29 (1997)

13. J.S. Sanghera, L.B. Shaw, and I.D. Aggarwal,"Applications of chalcogenide glass optical fibers *" C. R. Chimie.*, **5**(12) 873-883 (2002)

14. R. Stegeman, G. Stegeman, P. Delfyett, L. Petit, N. Carlie, K. Richardson, and M. Couzi,"Raman gain measurements and photo-induced transmission effects of germanium- and arsenic-based chalcogenide glasses*"* *Optics Exp.*, **14**(24) 11702-11708 (2006)

15. O. Fedotova, A. Husakou, and J. Hermann,"Supercontinuum generation in planar rib waveguides enabled by anomalous dispersion*"* *Optics Exp.*, **14**(4) 1512-1516 (2006)

16. J. Hu, C.R. Menyuk, L.B. Shaw, J.S. Sanghera, and I.D. Aggarwal. *Generating mid-IR source using As_2S_3-based chalcogenide photonic crystal fibers*. in *Conf. Lasers Elecro Optics*: Opt. Soc. Am. (2009)

17. S. Hocde, C. Boussard-Pledel, G. Fonteneau, and J. Lucas,"Chalcogens based glasses for IR fiber chemical sensors*"* *Solid State Sci.*, **3**(3) 279-284 (2001)

18. A. Ganjoo, H. Jain, C. Yu, J. Irudayaraj, and C.G. Pantano,"Detection and fingerprinting of pathogens: Mid-IR biosensor using amorphous chalcogenide films*"* *J. Non-Cryst. Solids*, **354** 2757-2762 (2008)

19. J. Hu, V. Tarasov, A. Agarwal, L. Kimerling, N. Carlie, L. Petit, and K. Richardson,"Fabrication and testing of planar chalcogenide waveguide integrated microfluidic sensor*"* *Optics Exp.*, **15**(5) 2307-2314 (2007)

20. G. Delaizir, P. Lucas, X. Zhang, H. Ma, B. Bureau, and J. Lucas,"Infrared Glass–Ceramics With Fine Porous Surfaces for Optical Sensor Applications*"* *J. Am. Ceram. Soc.* , **90** 2073-2077 (2007)

21. R. Song, X. Mu, A.Ganjoo, Y.J. Ding, and H. Jain,"Design, characterization, and optimization of waveguides based on chalcogenide glasses for biosensors*"* *Proc. SPIE*, **5585** (2004)

22. A. Schweinsberg, S. Hocdé, N.N. Lepeshkin, R.W. Boyd, C. Chase, and J.E. Fajardo,"An environmental sensor based on an integrated optical whispering gallery mode disk resonator*"* *Sens. Act. B*, **123**(2) 727-732 (2007)

`

23. F. Pietrucci, S. Caravati, and M. Bernasconi,"TeO_2 glass properties from first principles" *Phys. Rev. B*, **78** (2008)

24. M. Dongol, T. Gerber, M. Hafiz, M. Abou-Zied, and A.F. Elhady,"On the structure of As_2Te_3 glass" *J. Phys: Cond. Mat.*, **18** 6213–6224 (2006)

25. C. Vigreux-Bercovici, L. Labadie, J.E. Broquin, P. Kern, and A. Pradel,"Selenide and telluride thick films for mid and thermal infrared applications" *J. Optoelectron. Adv. Mater.*, **7**(5) 2625-2634 (2005)

26. V. Pamukchieva, A. Szekeres, K. Todorova, M. Fabian, E. Svab, Z. Revay, and L. Szentmiklosi,"Evaluation of basic physical parameters of quaternary Ge–Sb-(S,Te) chalcogenide glasses" *J. Non-Cryst. Solids*, **355**(50-51) 2485-2490 (2009)

27. R. Zallen, *The Physics of Amorphous Solids*, Weinheim: Verlag (1983)

28. V.K. Tikhomirov,"Relaxation of a photoinduced anisotropy in chalcogenide glasses" *JETP Lett.*, **57**(12) 821-825 (1993)

29. A. Ganjoo and H. Jain,"Millisecond kinetics of photoinduced changes in the optical parameters of a-As_2S_3 films" *Phys. Rev. B*, **74** 024201 (2006)

30. K. Tanaka,"*Phys. Rev. B*, **57** 5163 (1998)

31. S.R. Ovshinsky and W. Czubatyj,"New developments in optical phase-change memory" *Proc. SPIE*, **4085** 15-22 (2001)

32. A.L. Greer,"Materials science: Changing face of the chameleon" *Nature*, **437** 1246-1247 (2005)

33. M. Veinguer, A. Feigel, B. Sfez, M. Klebanov, and V. Lyubin,"New Application Of Inorganic Chalcogenide Photoresists In Lift-Off Photolithography" *J. Optoelectron. Adv. Mater.*, **5**(5) 1361-1264 (2002)

34. I.Z. Indutnyy, M. Popescu, A. Lorinczi, F. Sava, V.I. Min'ko, and P.E. Shepeliavyi,"Interference lithography using chalcogenide inorganic photoresist" *J. Optoelectron. Adv. Mater.*, **12** 3188-3192 (2008)

35. A. Zoubir, C. Lopez, M. Richardson, and K. Richardson,"*Optics Lett.*, **29** 1840-1842 (2004)

36. O. Efimov, L. Glebov, K. Richardson, E.V. Stryland, T. Cardinal, S. Park, M. Couzi, and J. Bruneel,"Waveguide writing in chalcogenide glasses by a train of femtosecond laser pulses" *Opt. Mater.*, **17**(3) 379-386 (2001)

`

37. A. Ganjoo, H. Jain, J. Ryan, R. Song, R. Chanda, J. Irudyraj, Y. Ding, and C. Pantano,"Fabrication of chalcogenide glass waveguide for IR evanescent wave sensors" *Proc. SPIE*, **5593** 637-642 (2004)

38. N. Ponnampalam, R. DeCorby, H. Nguyen, P. Dwivedi, C. Haugen, J. McMullin, and S. Kasap,"Small core rib waveguides with embedded gratings in As_2Se_3 glass" *Optics Express*, **12**(25) 6270-6277 (2004)

39. J. Viens, C. Meneghini, A. Villeneuve, T. Galstian, E. Knystautas, M. Duguay, K. Richardson, and T. Cardinal,"Fabrication and characterization of integrated optical waveguides in sulfide chalcogenide glasses" *J. Lightwave Tech.*, **17**(7) 1184-1191 (1999)

40. H. Takahara, T. Takeuchi, M. Tabuchi, H. Kageyama, Y. Kobayashi, Y. Kurisu, S. Kondo, and R. Kanno,"All-Solid-State Lithium Secondary Battery Using Oxysulfide Glass" *J. Electrochem. Soc.*, **151**(10) A1539-A1544 (2004)

41. K. Minami, A. Hayashi, and M. Tatsumisago,"Electrical and electrochemical properties of the $70Li_2S{\cdot}(30-x)P_2S_5{\cdot}xP_2O_5$ glass-ceramic electrolytes" *Sol. State Ionics*, **179** 1282–1285 (2008)

42. K. Minami, F. Mizuno, A. Hayashi, and M. Tatsumisago,"Structure and properties of the $70Li_2S$ $(30-x)P_2S_5$ xP_2O_5 oxysulfide glasses and glass–ceramics" *J. Non-Cryst. Solids*, **354** 370–373 (2008)

43. J. Schrooten, B. Meyer, S.W. Martin, and F. Borsa,"Preparation and characterization of boron oxysulfide glasses" *J. Non-Cryst. Solids*, **319** 136–144 (2003)

44. Y. Ikeda, T. Kitade, S. Kohjiya, A. Hayashi, A. Matsuda, M. Tatsumisago, and T. Minami,"Ion conducting composites from $Li_2S–SiS_2–Li_4SiO_4$ oxysulfide glass and poly(oxyethylene)s" *Polymer*, **42**(16) 7225-7228 (2001)

45. A. Hayashi, M. Tatsumisago, T. Minami, and Y. Miura,"Structural Investigation of $95(0.6Li_2S\text{-}0.4SiS_2)$ $5Li_4SiO_4$ Oxysulfide Glass by Using X-ray Photoelectron Spectroscopy" *J. Am. Ceram. Soc.*, **81**(5) 1305-1309 (2005)

46. Y. Kim, J. Saienga, and S.W. Martin,"Glass formation in and structural investigation of $Li_2S + GeS_2 + GeO_2$ composition using raman and IR spectroscopy" *J. Non-Cryst. Solids*, **351**(49-51) 3716-3724 (2005)

47. G. Pfister, K.S. Liang, M. Morgan, P.C. Taylor, E.J. Friebele, and S.G. Bishop,"*Phys. Rev. Lett.*, **41** 1318 (1978)

`

48. K.L. Bhatia, D.P. Gosain, G. Parthasarathy, and E.S.R. Gopal,"Morphological structure of bismuth-doped n-type amorphous germanium sulphide semiconductors *" J. Mat. Sci. Lett.*, **5**(12) 1281-1284 (1986)

49. D. Adler,"Theory of amorphous semiconductors*" Solar Cells*, **2** 199-226 (1980)

50. Y. Vlasov, A. Legin, A. Rudnitskaya, C. Di Natale, and A. D'Amico,"Nonspecific sensor arrays ("electronic tongue") for chemical analysis of liquids*" Pure Appl. Chem.*, **77**(11) 1965-1983 (2005)

51. M.J. Schoning and J.P. Kloocka,"About 20 Years of Silicon-Based Thin-Film Sensors with Chalcogenide Glass Materials for Heavy Metal Analysis: Technological Aspects of Fabrication and Miniaturization*" Electroanal.*, **19**(19-20) 2029 – 2038 (2007)

52. T. Wagner, R. Molina, T. Yoshinobu, J.P. Kloock, M. Biselli, M. Canzoneri, T. Schnitzler, and M.J. Schoning,"Handheld multi-channel LAPS device as a transducer platform for possible biological and chemical multi-sensor applications*" Electrochim. Acta*, **53** 305-311 (2007)

53. Y.G. Vlasov, E.A. Bychkov, and A.V. Bratov,"Ion-selective Field-effect Transistor and Chalcogenide Glass Ion-selective Electrode Systems for Biological Investigations and Industrial Applications*" Analyst*, **119** 449-454 (1994)

54. J. Hu, L. Petit, X. Sun, A.M. Agarwal, N. Carlie, T. Anderson, J. Choi, J.J. Viens, M. Richardson, K.C. Richardson, and L.C. Kimerling,"Studies on structural, electrical, and optical properties of Cu doped As-Se-Te chalcogenide glasses*" J. Appl. Phys.*, **101**(6) 063520-9 (2007)

55. H. Abe and Y. Nakamura,"The effect of Cu doping on the DC conductivity and thermoelectric power of AS2Se3-based glasses*" Phys. Stat. Sol. A*, **107**(1) 315 - 319 (2006)

56. T. Carrig,"*J. Electron. Mater.*, **31** 759 (2002)

57. S.R. Lukic, D.M. Petrovic, I.I. Turyanitsa, and O.V. Khiminets,"*J. Mater. Sci*, **26** (1991)

58. K. Nakayama, K. Kojima, Y. Imai, T. Kasai, S. Fukushima, A. Kitagawa, M. Kumeda, Y. Kakimoto, and M. Suzuki,"Nonvolatile Memory Based on Phase Change in Se–Sb–Te Glass*" Jpn. J. Appl. Phys.*, **42** 404-408 (2003)

`

59. J.S. Sanghera, L.B. Shaw, and I.D. Aggarwal,"Applications of chalcogenide glass optical fibers" *C. R. Chimie.* , **5**(12) 873-878 (2002)

60. M. Asobe, T. Ohara, T. Kaino, and I. Yokohama,"Low power all-optical switching in a nonlinear optical loop mirror using chalcogenide glass fibre" *Electron. Lett.*, **32**(15) 1396-1397 (1996)

61. G.I. Stegeman,"Material figures of merit and implications to all-optical waveguide switching" *Proc. SPIE*, **1852** 75-89 (1993)

62. V.G. Ta'eed, M. Shokooh-Saremi, L. Fu, D.J. Moss, M.L. Rochette, I. C. M., B.J. Eggleton, Y. Ruan, and B. Luther-Davies,"Integrated all-optical pulse regenerator in chalcogenide waveguides" *Optics Letters*, **30**(21) 2900-2902 (2005)

63. W.J. Miniscalo,"Erbium-doped glasses for fiber amplifiers at 1500 nm" *J. Lightwave Tech.*, **9**(2) 243-250 (1991)

64. L. Brilland, F. Smektala, G. Renversez, T. Charletier, J. Troles, T.N. Nguyen, N. Traynor, and A. Monteville,"Fabrication of complex structures of Holey Fibers in Chalcogenide glass" *Optics Express*, **14**(3) 1280-1285 (2006)

65. A.R. Hilton, A.R. Hilton, J. McCord, and T.J. Loretz,"Laser-power delivery using chalcogenide glass fibers " *Proc. SPIE*, **2977** 20-29 (1997)

66. S. Hocde, C. Boussard-Pledel, G. Fonteneau, D.L. Coq, H. Ma, and J. Lucas,"Recent developments in chemical sensing using infrared glass fibers" *J. Non-Cryst. Solids*, **274** 17-22 (2000)

67. P. Lucas, D.L. Coq, C. Juncker, J. Collier, D. Boesewetter, C. Bousard-Pledel, B. Bureau, and M.R. Riley,"Evaluation of Toxic Agent Effects on Lung Cells by Fiber Evanescent Wave Spectroscopy" *Appl. Spect.* , **59**(1) 1-9 (2005)

68. J. Frantz, L. Shaw, J. Sanghera, and I. Aggarwal,"Waveguide amplifiers in sputtered films of Er^{3+}-doped gallium lanthanum sulfide glass" *Optics Express*, **14**(5) 1797-1803 (2004)

69. A. Ganjoo, H. Jain, C. Yu, R. Song, J.V. Ryan, J. Irudayaraj, Y.J. Ding, and C.G. Pantano,"Planar chalcogenide glass waveguides for IR evanescent wave sensors" *J. Non-Cryst. Solids*, **352** 584-588 (2006)

70. J. Hu, V. Tarasov, N. Carlie, N. Feng, L. Petit, A. Agarwal, K. Richardson, and L. Kimerling,"Si-CMOS-compatible lift-off fabrication of low-loss planar chalcogenide waveguides," *Optics Exp.*, **15**(5) (2007)

71. A. Mairaj, C. Riziotis, A. Chardon, P. Smith, D. Shepherd, and D. Hewak,"Development of channel waveguide lasers in Nd^{3+}-doped chalcogenide (Ga:La:S) glass through photoinduced material modification" *Appl. Phys. Lett.*, **81**(20) 3708-3710 (2002)

72. B.J. Riley, S.K. Sundaram, B.R. Johnson, and L.V. Saraf,"Fabrication of nano-gratings in arsenic sulphide films" *J. Non-Cryst. Solids,* **354** 813-816 (2008)

73. Y. Ruan, W. Li, R. Jarvis, N. Madsen, A. Rode, and B. Luther-Davies,"Fabrication and characterization of low loss rib chalcogenide waveguides made by dry etching" *Optics Express*, **12**(21) 5140-5145 (2004)

74. S. Ramachandran and S.G. Bishop,"*Appl. Phys. Lett.*, **74** (1999)

75. A. Kovalskiy, M. Vlcek, H. Jain, A. Fiserova, C.M. Waits, and M. Dubey,"Development of chalcogenide glass photoresists for gray scale lithography" *J. Non-Cryst. Solids*, **352** 589-594 (2006)

76. R.J. Curry, A.K. Mairaj, C.C. Huang, R.W. Eason, C. Grivas, D.W. Hewak, and J.V. Badding,"Chalcogenide Glass Thin Films and Planar Waveguides" *J. Am. Ceram. Soc.*, **88**(9) 2451-2455 (2005)

77. V. Lyubin, M. Klebanov, I. Bar, S. Rosenwaks, N.P. Eisenberg, and M. Manevich,"*J. Vac. Sci. Technol. B*, **15** 823-827 (1997)

78. N.P. Eisenberg, M. Manevich, S. Noacha, M. Klebanov, and V. Lyubin,"New types of microlens arrays for the IR based on inorganic chalcogenide photoresists " *Mat. Sci. Semicond. Proc.*, **3**(5-6) 443-448 (2001)

79. J. Orava, T. Wagner, M. Krbal, T. Kohoutek, M. Vlcek, and M. Frumar,"Selective wet-etching of undoped and silver photodoped amorphous thin films of chalcogenide glasses in inorganic alkaline solutions" *J. Non-Cryst. Solids*, **352**(1637-1640) (2006)

80. J. Orava, T. Wagner, M. Krbal, T. Kohoutek, M. Vlcek, and M. Frumar,"Selective wet-etching and characterization of chalcogenide thin films in inorganic alkaline solutions" *J. Non-Cryst. Solids*, **353**(2007) 1441-1445 (2007)

81. J. Xu and R.M. Almeida,"Preparation and Characterization of Germanium Sulfide Based Sol-Gel Planar Waveguides" *J. Sol-Gel Sci. Technol.* , **19**(1-3) 243-248 (2000)

82. J. Xu and R.M. Almeida,"Sol-gel derived germanium sulfide planar waveguides" *Mat. Sci. Semicond. Proc.*, **3** 339-344 (2000)

`

83. O. Martins, X. Jian, and R.M. Almeida,"Sol-gel processing of germanium sulfide based films" *J. Non-Cryst. Solids*, **256-257** (1998)

84. B. Elling and R. Danz,"Active polymer glass hybrid waveguides" *Mat. Sci. Eng. C*, **8-9** 401-405 (1999)

85. Y. Enami, P. Poyhonen, D.L. Mathine, A. Bashar, P. Madasamy, S. Honkanen, B. Kippelen, N. Peyghambarian, S.R. Marder, A.K.Y. Jen, and J. Wu,"Poling of soda-lime glass for hybrid glass/polymer electro-optic modulators" *Appl. Phys. Lett.*, **76**(9) 1086-1088 (2000)

86. M. Garcia, J.I. Eguiazabal, and J. Nazabal,"Processability and mechanical performance of hybrid composites based on poly(ether sulfone) modified with a glass fiber-reinforced liquid crystalline polymer" *J. Appl. Polym. Sci.*, **91**(2) 854-860 (2004)

87. M. Garcia, J.I. Eguiazabal, and J. Nazabal,"Two scale reinforcement in hybrid composites based on poly(ether sulfone), glass fiber and liquid crystalline polymer" *Compos. Sci. Technol.*, **63**(15) 2163-2170 (2003)

88. G. Gunduz, D. Erol, and N. Akkas,"Mechanical properties of unsaturated polyester-isocyanate hybrid polymer network and its E-glass fiber-reinforced composite" *J. Compos. Mat.*, **39**(17) 1577-1589 (2005)

89. E.K. Johnson, J.M. Kvavle, R.H. Selfridge, S.M. Schultz, R. Forber, W. Wang, and D.Y. Zang,"Electric field sensing with a hybrid polymer/glass fiber" *Appl. Opt.*, **46**(28) 6953-6958 (2007)

90. K.G. Sharp,"A New Route to Polymer-Filled Glass - Hybrid Interpenetrating Networks with Appreciable Toughness" *Hybrid Org.-Inorg. Compos.*, **585** 163-180 (1995)

91. R. Shechter, E. Millul, Y. Amitai, A.A. Friesem, and V. Weiss,"Hybrid polymer-on-glass integrated optical diffractive structures for wavelength discrimination" *Opt. Mater.*, **17**(1-2) 165-167 (2001)

92. M.M. Thwe and K. Liao,"Durability of bamboo-glass fiber reinforced polymer matrix hybrid composites" *Compos. Sci. Technol.*, **63**(3-4) 375-387 (2003)

93. S.C. Tjong and S.A. Xu,"Mechanical properties of glass fiber and liquid crystalline polymer reinforced polypropylene hybrid composites toughened with elastomers" *J. Appl. Polym. Sci.*, **94**(4) 1539-1546 (2004)

94. J. Wallace,"Electro-optics - Hybrid polymer/glass fiber senses electric fields" *Laser Focus World*, **43**(11) 51-52 (2007)

95. S. Yokoyama and S. Mashiko,"Tuning of laser frequency in random media of dye-doped polymer and glass-particle hybrid" *Jap. J. Appl. Phys.*, **42**(8A) L970-L973 (2003)

96. X.B. Yu, C. Wei, D. Xu, C.H. Lu, J.H. Yu, and S.R. Lu,"Wear and mechanical properties of reactive thermotropic liquid crystalline polymer/unsaturated polyester/glass fiber hybrid composites" *J. Appl. Polym. Sci.*, **103**(6) 3899-3906 (2007)

97. K.M. Zhou, X.F. Chen, Y.C. Lai, K. Sugiden, L. Zhang, and I. Bennion,"In-fiber polymer-glass hybrid waveguide Bragg grating" *Optics Lett.*, **33**(15) 1650-1652 (2008)

98. S.W. Hughes,"Archimedes revisited: a faster, better, cheaper method of accurately measuring the volume of small objects" *Phys. Ed.* , **40**(5) 468-474 (2005)

99. E. Hecht, *Optics*, San Francisco: Pearson (2002)

100. G. Bokov and Y.I. Naberukhin,"Application of the Onsager model to the theory of the dielectric constant of nonpolar liquids" *J. Chem. Phys.*, **75**(5) 2357-2365 (1981)

101. R.L. Smith and G.E. Sandland,"An Accurate Method of Determining the Hardness of Metals, with Particular Reference to Those of a High Degree of Hardness" *Proc. Inst. Mech. Eng.*, **1** 623-641 (1922)

102. N. Carlie, J. Massera, L. Petit, and K. Richardson. *Application of Micro-thermal Analysis for Metal, Oxide, and Non-oxide Thin Film Materials*. in *NIST: Front. Char. Metrol. Nanoelectron.* Albany NY (2009)

103. G.J. Adriaenssens and A. Stesmans,"Gap States in Chalcogenide Glasses" *J. Optoelectron. Adv. Mater.* , **4**(4) 837-842 (2002)

104. J. Tauc, *Amorphous and Liquid Semiconductors*, New York: Plenum (1974)

105. S.R. Elliot, *Physics of Amorphous Materials*, Essex: Longman (1990)

106. F. Wooten, *Optical Properties of Solids*, New York: Academic Press (1972)

107. S.T. Kirsch,"Determining refractive index and thickness of thin films from prism coupler measurements" *Appl. Opt.*, **20** 2085-2089 (1981)

108. R. Swanepoel,"Determination of the thickness and optical constants of amorphous silicon" *J. Phys. E: Sci. Instrum*, **16** 1214-1222 (1983)

109. A.L. Patterson,"The Sherrer formula for X-Ray particle size determination" *Phys. Rev.* , **56**(10) 978-982 (2002)

110. A. Zakery and S.R. Elliot,"Optical Properties and Applications of Chalcogenide Glasses: A Review" *J. Non-Cryst Solids*, **330**(1) 1-12 (2003)

111. L. Petit, N. Carlie, F. Adamietz, M. Couzi, V. Rodriguez, and K.C. Richardson,"Correlation between physical, optical and structural properties of sulfide glasses in the system Ge–Sb–S" *Mat. Chem. Phys.*, **97** 64-70 (2006)

112. B. Zhong, I. Watanabe, and T. Shimizu,"Effect of Sb Incorporation in Ge–S Glasses" *Jpn. J. Appl. Phys.*, **22** 780-784 (1983)

113. L. Petit, N. Carlie, A. Humeau, G. Boudebs, H. Jain, A.C. Miller, and K. Richardson,"Correlation between the nonlinear refractive index and structure of germanium-based chalcogenide glasses" *Mat. Res. Bull.*, **42**(12) 2107-2116 (2007)

114. G. Yang, H. Jain, A. Ganjoo, D. Zhao, Y. Xu, H. Zeng, and G. Chen,"A photo-stable chalcogenide glass" *Optics Exp.*, **16**(14) 10565-10571 (2008)

115. E. Marquez, A.M. Bernal-Oliva, J.M. Gonzalez-Leal, R. Prieto-Alcon, and T. Wagner,"Optical properties and structure of amorphous $(As_{0.33}S_{0.67})_{100-x}Te_x$ and $Ge_xSb_{40-x}S_{60}$ chalcogenide semiconducting alloy films deposited by vacuum thermal evaporation" *J. Phys. D.* , **39**(9) 1793-1799 (2006)

116. B. Tatian,"Fitting refractive-index data with the Sellmeier dispersion formula" *Appl. Opt.*, **23**(24) 4477-4485 (1984)

117. D.S. Ma, P.S. Danielson, and C.T. Moynihan,"Multiphonon absorption in XAs_2S_3-(1-X)GeS_2 Glasses" *J. Non-Cryst. Solids*, **81** 61-70 (1986)

118. D.S. Ma, P.S. Danielson, and C.T. Moynihan,"Bulk and Impurity Absorption in 0.5 As_2Se_3-0.5 $GeSe_2$ glass" *J. Non-Cryst. Solids*, **37** 181-190 (1980)

119. E.I. Kamitsos, J.A. Kapoutsis, I.P. Culeac, and M.S. Iovu,"Structure and Bonding in As-Sb-S Chalcogenide Glasses by Infrared Reflectance Spectroscopy" *J. Phys. Chem. B*, **101** 11061-11067 (1997)

`

120. M. Frumar, Z. Polak, and Z. Cernosek,"Raman spectra and photostructural changes in the short-range order of amorphous As-S chalcogenides" *J. Non-Cryst Solids*, **256&257** 105-110 (1999)

121. R. Forniers,"The infrared and Raman spectra of realgar and orpiment" *Amer. Mineralogist*, **54** 1062-1074 (1969)

122. A. Bertoluzza, C. Fagnano, P. Monti, and G. Semerano.,"Raman and infrared spectra of As_2S_x chalcogenide glasses with x < 3" *J. Non-Cryst. Solids*, **29** 49-60 (1978)

123. M. Kincl and L. Tichy,"*Mat. Chem. Phys.* , **103** 78-88 (2007)

124. C. Julien, S. Barnier, M. Massot, N. Chbani, X. Cai, A.M. Loireau-Lozac'h, and M. Guittard,"Raman and infrared spectroscopic studies of Ge-Ga-Ag sulphide glasses" *Mat. Sci. Eng. B* **22**(2-3) 191-200 (1994)

125. Q. Mei, J. Saienga, J. Schrooten, B. Meyer, and S.W. Martin,"Preparation and characterization of glasses in the $Ag_2S+B_2S_3+GeS_2$ system" *J. Non-Cryst Solids*, **324** 264-276 (2003)

126. B. Frumarova, P. Nemec, M. Frumar, J. Oswald, and M. Vleck,"Synthesis and optical properties of the Ge-Sb-S:$PrCl_3$ glass system" *J. Non-Cryst. Solids*, **256&257** 266-270 (1999)

127. P. Bonazzi and L. Bindi,"A crystallographic review of arsenic sulfides: effects of chemical variations and changes induced by exposure to light" *Z. Kristallogr.*, **223** 132–147 (2008)

128. B.G. Aitken and C.W. Ponader,"Physical properties and Raman spectroscopy of GeAs sulphide glasses" *J. Non-Cryst. Solids*, **256&257** 143-148 (1999)

129. K. Tanaka,"*Phys. Rev. B*, **39** 1270-1279 (1989)

130. Y. Luo, *Comprehensive Handbook of Chemical Bond Energies*, Boca Raton, FL: CRC Press (2007)

131. T. Anderson, L. Petit, N. Carlie, J. Choi, J. Hu, A. Agarwal, L. Kimerling, K. Richardson, and M. Richardson,"Femtosecond laser photo-response of $Ge_{23}Sb_7S_{70}$ films" *Optics Exp.*, **16**(24) 20081-20098 (2009)

`

132. L. Petit, N. Carlie, T. Anderson, M. Couzi, J. Choi, M. Richardson, and K.C. Richardson,"Effect of IR femtosecond laser irradiation on the structure of new sulfo-selenide glasses" *Opt. Mater.*, **29** 1075-1083 (2007)

133. M.D. O'Donnel, A.B. Seddon, D. Furniss, C. Rivero, M. Ramme, R. Stegeman, G. Stegeman, K. Richardson, R. Stolen, M. Couzi, and T. Cardinal,"Tellurite and fluoro-tellurite glasses for fiberoptic Raman amplifiers: Glass characterization, optical properties, Raman gain, preliminary fiberization and fiber characterization" *J. Am. Ceram. Soc.*, **90**(5) 1448–1457 (2007)

134. R. Kaigawa, A. Ohyama, T. Wada, and R. Klenk,"Electrical properties of homogeneous Cu(In,Ga)S_2 films with varied gallium content " *Thin Solid Films*, **515**(5) 6260-6264 (2007)

135. M. Yamashita, H. Yamanaka, and H. Wakabayashi,"Thin-film preparation of the Li_2S-GeS_2-Ga_2S_3 glass system by sputtering" *Solid State Ionics*, **89**(3-4) 299-304 (1996)

136. J. Schubert,"Chalcogenide-based thin film sensors prepared by pulsed laser deposition technique " *Appl. Phys. A*, **69**(1) S803-S805 (1999)

137. J. Boudies, *Dissolution kinetics of two types of glasses: As_2S_3 and $Ge_{23}Sb_7S_{70}$* in *NSF Internal REU Program*, National Science Foundation, Grant EEC-0244109 and DMR-031208 (2007)

138. S.B. Mamedov and M.D. Michailov,"Dissolution kinetics of glassy and crystalline As_2S_3 in aqueous sodium sulfide and hydroxide" *J. Non-Cryst. Solids*, **221** 181-186 (1997)

139. M.D. Michailov, S.B. Mamedov, and S.V. Tsventarnyi,"Dissolution Kinetics of Glassy Arsenic Sulfide in Alkali and Amine Solutions" *J. Non-Cryst. Solids*, **176**(2-3) 258-262 (1994)

140. M.D. Mikhailov, S.B. Mamedov, and S.V. Tsventarnyi,"Kinetics of Dissolution of Glassy Arsenic Sulfide in Alkali and Amine Solutions" *J. Appl. Chem. USSR*, **60**(4) 693-696 (1987)

141. S.A. Zenkin, S.B. Mamedov, and M.D. Mikhailov,"Kinetics of Dissolution of Arsenic Sulfide Films in Solutions of Ammonia, Methylamine, and Dimethylamine" *J. Appl. Chem. USSR*, **61**(7) 1336-1340 (1988)

142. F.P. Daly and C.W. brown,"Raman Spectra of Sulfur Dissolved in Primary amines" *J. Phys. Chem.*, **77**(15) 1859-1861 (1973)

`

143. R. MacColl and S. Windwer,"Spectroscopy of Sulfur in Ethylenediamine" *J. Phys. Chem.*, **74**(6) 1261-1265 (1970)

144. W.G. Hodgson, S.A. Buckler, and G. Peters,"*J. Am. Chem. Soc.*, **85** 543–546 (1963)

145. R. Steudel, J. Albertsen, and K. Zink,"*Ber. Bunsenges. Phys. Chem.*, **92** 502 (1989)

146. P. Hassanzadeh and L. Andrews,"Vibronic absorption spectra of sulfur (S_3 and S_4) in solid argon" *J. Phys. Chem.*, **96** 6579-6585 (1992)

147. R. Steudel, Y. Steudel, and M.W. Wong,"Speciation and Thermodynamics of Sulfur Vapor" *Top. Curr. Chem.*, **230** 117–134 (2003)

148. P.C. Hiemenz and R. Rajagopalan, *Principles of colloid and surface chemistry*. 3rd ed, New York: Marcel Dekker (1997)

149. M.J. MacLachan, N. Coombs, and G.A. Ozin,"*Nature*, **402** 867-871 (1999)

150. M.J. MacLachlan, S. Petrov, R.L. Bedard, I. Manners, and G.A. Ozin,"*Angew. Chem. Int. Ed.*, **37** 2075-2079 (1998)

151. M.F. Vigasnia, R.Y. Orlov, A.V. Shabatina, and T.P. Dadze,"*J.Mol. Liq.*, **91** 103-107 (2001)

152. G.R. Helz, M.S. Valerio, and N.E. Capps,"*Environ. Sci.Tech.*, **36** 943-948 (2002)

153. J.A. Tossell,"*Geochim. Cosmochim. Acta*, **67** 3347-3354 (2003)

154. S. Bag, P.N. Trikalitis, P.J. Chupas, G.S. Armatas, and M.G. Kanatzidis,"*Science*, **317** 490-493 (2007)

155. N. Carlie, J. Massera, L. Petit, C. Vigreux, A. Pradel, and K. Richardson,"On the use of the micro-thermal analyzer as a new tool for the measurement of thermal properties of chalcogenide thin films, while still attached to the substrate." *Microsc. Microanal.* ,

156. T.A. Guiton and C.G. Pantano,"*Chem. Matls.*, **1** 558-563 (1989)

157. C.-F. Lin, E.-Z. Liang, S.-M. Shih, and W.-F. Su,"Significance of Surface Properties of CdS Nanoparticles" *Jpn. J. Appl. Phys.*, **42** L610–L612 (2003)

158. T. Kohoutek, T. Wagner, J. Orava, M. Frumar, V. Perina, A. Mackova, V. Hnatowitz, M. Vlcek, and S. Kasap,"Amorphous films of Ag–As–S system

prepared by spin-coating technique, preparation techniques and films physico-chemical properties *" Vacuum*, **76**(2-3) 191-194 (2004)

159. J. Wang, M. Lin, T. Zhang, Y. Yan, P.C. Ho, Q.-H. Xu, and K.P. Loh,"Arsenic(II) Sulfide Quantum Dots Prepared by a Wet Process from its Bulk*" J. Am. Chem. Soc.*, **130** 11596–11597 (2008)

160. R.G. Parr and R.G. Pearson,"Absolute Hardness: Companion Parameter to Absolute Electronegativity*" J. Am. Chem. Soc.*, **105** 7512-7516 (1983)

161. R.G. Pearson,"Hard and soft acids and bases, HSAB, part II: Underlying theories*" J. Chem. Educ.*, **45** 643–648 (1968)

162. R.G. Pearson,"Hard and soft acids and bases, HSAB, part I: Fundamental principles*" J. Chem. Educ.*, **45** 581–586 (1968)

163. J. Hubbard,"Electron Correlations in Narrow Energy Bands*" Proc. R. Soc. Lond. A*, **276** 238-257 (1963)

164. J. Keller, C.E. Leal, and F. Forsthofer,"Electron-phonon interaction in Hubbard systems *" Physica B*, **206-207** 739-741 (1995)

165. J. McMurry, *Organic Chemistry*. 5th ed, Pacific Grove: Brooks/Cole (1999)

166. M.G. Velarde and R.K. Zeytounian, *Interfacial phenomena and the Marangoni effect*, Udine, Italy: CISM (2002)

167. N. Sahu, B. Parija, and S. Panigrahi,"Fundamental understanding and modeling of spin coating process : A review*" Indian J. Phys*, **83**(4) 493-502 (2009)

168. E. Márquez, J.M. González-Leal, R. Jiménez-Garay, and M. Vlcek,"*Thin Solid Films*, **396** 184-191 (2001)

169. Y.-Y. Huang and K.-S. Chou,"Studies on the spin coating process of silica films*" Ceram. Int.* , **29** 485–493 (2003)

170. A.B. Seddon,"Chalcogenide glasses: a review of their preparation, properties and applications*" J. Non-Cryst. Solids*, **184** 44-50 (1995)

171. P.J.S. Ewen, M.J. Sik, and A.E. Owen,"A note on the Raman spectra and structure of As_xS_{100-x} (x > 40) glasses*" Sol. State. Comm.*, **33** 1067-1070 (1980)

172. M. Frumar, J. Jedelsky, B. Frumarova, T. Wagner, and M. Hrdlicka,"Optically and thermally induced changes of structure, linear and non-linear optical

properties of chalcogenides thin films*" J. Non-Cryst. Solids*, **326&327** 399-404 (2003)

173. Y.F. Ding, J.S. He, J. Zhang, C.Y. Liu, P. Chen, and A.Q. Zhang,"Rheological hybrid effect in nylon 6/liquid crystalline polymer blends caused by added glass beads*" J. Non-Newt. Fluid Mech.*, **135**(2-3) 166-176 (2006)

174. D.A. Savin, J. Pyun, G.D. Patterson, T. Kowalewski, and K. Matyjaszewski,"Synthesis and characterization of silica-graft-polystyrene hybrid nanoparticles: Effect of constraint on the glass-transition temperature of spherical polymer brushes*" J. Polym. Sci. B*, **40**(23) 2667-2676 (2002)

175. G. Mie,"Beiträge zur Optik trüber Medien, speziell kolloidaler Metallösungen*" Ann. Phys.* ,(330) 377-445 (1908)

176. S.A. Jenekhe and S.B. Schuldt,"Coating flow of non-Newtonian fluids on a flat rotating disk*" Ind. Eng. Chem. Fundamen.*, **23**(4) 432–436 (1984)

177. J.P.F. Charpin, M. Lombe, and T.G. Myers,"Spin coating of non-Newtonian fluids with a moving front*" Phys. Rev. E.*, **76** 016312 (2007)

178. G.W.S. Blair,"*J. Phys. Chem.*, **43**(7) 853-864 (1939)

179. R.H. Colby, D.C. Boris, W.E. Krause, and S. Dou,"Shear thinning of unentangled flexible polymer liquids*" Rheol Acta*, **46** 569–575 (2007)

180. M.N. Rahaman, *Ceramic Processing*, Boca Raton: CRC Press (2007)

181. H. Dislich,"*J. Non-Cryst. Solids*, **80** 115-121 (1980)

182. B.T. Chen,"*Polym. Eng. Sci.*, **23** 399-493 (1983)

183. C.J.R. Gonzalez-Oliver and I. Kato,"Sn(Sb)-oxide sol-gel coatings on glass *" J. Non-Cryst. Solids*, **82**(1-3) 400-410 (1986)

184. M. Kaelin, D. Rudmann, and A.N. Tiwari,"Low cost processing of CIGS thin film solar cells *" Solar Energy*, **77**(6) 749-756 (2004)

185. H.G. Floch, F. Belleville, and J.-J. Priotton,"*Am. Ceram. Soc. Bull.*, **74** 60-63 (1995)

186. A. Atkinson, J. Doorbar, A. Hudd, D.L. Segal, and P.J. White,"Continuous ink-jet printing using sol-gel “Ceramic” inks *" J. Sol-Gel Sci. Technol.*, **8**(1-3) 1093-1097 (1997)

187. X. Yu, Z. Wang, and Y. Han,"Microlenses fabricated by discontinuous dewetting and soft lithography" *Microelec. Eng.*, **89**(9) 18781881 (2008)

188. H. Nagata, S.W. Ko, E. Hong, C.A. Randall, S. Trolier-McKinstry, P. Pinceloup, D. Skamser, M. Randall, and A. Tajuddin,"Microcontact Printed BaTiO3 and LaNiO3 Thin Films for Capacitors" *J. Am. Ceram. Soc.*, **89**(9) 2816 - 2821 (2006)

189. K.Y. Suh, Y.S. Kim, and H.H. Lee,"Capillary Force Lithography" *Adv. Mat.*, **13**(18) 1386 - 1389 (2001)

190. J. Hu, N. Feng, N. Carlie, L. Petit, A. Agarwal, K. Richardson, and L. Kimerling,"Optical loss reduction in high-index-contrast chalcogenide glass waveguides via thermal reflow" *Opt. Exp.*, **18**(2) 1469-1478 (2010)

191. J. Hu, N. Feng, N. Carlie, L. Petit, J. Wang, A. Agarwal, K. Richardson, and L. Kimerling,"Low-loss high-index-contrast planar waveguides with graded-index cladding layers" *Opt. Exp.*, **15**(22) 14566-14572 (2007)